PACIFIC EARTHQUAKE ENGINEERING RESEARCH CENTER

Seismic Response Analysis of Highway Overcrossings Including Soil-Structure Interaction

Jian Zhang
and
Nicos Makris
Department of Civil and Environmental Engineering
University of California, Berkeley

PEER 2001/02
MARCH 2001

Seismic Response Analysis of Highway Overcrossings Including Soil-Structure Interaction

Jian Zhang and Nicos Makris
Department of Civil and Environmental Engineering
University of California, Berkeley

A report on research conducted under
grant CMS-9696241 from the National Science Foundation

PEER Report 2001/02
Pacific Earthquake Engineering Research Center
College of Engineering
University of California, Berkeley

March 2001

ABSTRACT

In this report the development and validation of a simple yet dependable method to estimate the seismic response of freeway overcrossings is presented. The proposed method adopts the substructure approach to address the issue of soil-foundation-superstructure interaction. The various steps of the method are validated with scarce historic records and are compared with the results obtained by other investigators.

Recognizing that soil-structure interaction affects appreciably the earthquake response of highway overcrossings, Chapter 2 concentrates on the calculation of the kinematic response functions and dynamic stiffnesses of the approach embankments. It is shown that the shear-wedge model yields dependable estimates for the amplification functions of typical embankments. The shear-wedge model is extended to a two-dimensional model in order to calculate the transverse static stiffness of an approach embankment loaded at one end. The formulation reveals a sound closed-form expression for the critical length, L_c, that is the ratio of the transverse static stiffness of an approach embankment and the transverse static stiffness of a unit-width wedge. It is shown through examples that the transverse dynamic stiffness ("spring" and "dashpot") of the approach embankment can be estimated with confidence by multiplying the dynamic stiffnesses of the unit-width wedge with the critical length, L_c. The study also shows that the values obtained for the transverse kinematic response function and dynamic stiffness can also be used with confidence to represent the longitudinal kinematic response function and dynamic stiffness, respectively.

The dynamic stiffness of piles and pile groups is revisited in Chapter 3 where an existing methodology is employed to determine the group effect. Chapter 4 concentrates on the computation of bridge response quantities. The analysis is conducted in the time domain using either an elementary stick model or a more sophisticated finite element formulation to discretize the bridge superstructure. All dynamic stiffnesses of approach embankments and pile groups are approximated with frequency-independent springs and dashpots that have been established in chapters 2 and 3. A real eigenvalue analysis confirms the one-to-one correspondence between modal characteristics obtained with the three-dimensional finite element solutions and the result of the simpler stick-model idealizations. A complex eigenvalue analysis reveals modal damping values in the first six modes of interest and shows that realistic damping ratios assume values much higher than those used by Caltrans. The efficiency of the proposed method is validated by comparing the computed time response quantities with records from the Meloland Road and the Painter Street overcrossings located in southern and northern California, respectively. The proposed procedure allows for inexpensive parametric analysis that examines the importance of considering soil-structure interaction at the end abutments and center bent. Results and recommendations presented by past investigations are revisited and integrated in comprehensive tables that improve our understanding of the

dynamic characteristics and behavior of freeway overcrossings. The study concludes with a step-by-step methodology that allows for a simple, yet dependable dynamic analysis of freeway overcrossings that involves a stick model and frequency-independent springs and dashpots.

ACKNOWLEDGMENTS

Partial financial support for this study was provided by the National Science Foundation under Grant CMS-9696241. The valuable input and comments of Dr. Tim Delis are appreciated.

This work made use of Pacific Earthquake Engineering Research Center shared facilities supported by the Earthquake Engineering Research Center Program of the National Science Foundation under award number EEC-9701568.

CONTENTS

ABSTRACT iii

ACKNOWLEDGMENTS v

TABLE OF CONTENTS vii

LIST OF FIGURES ix

LIST OF TABLES xv

CHAPTER 1: INTRODUCTION 1
- 1.1 Background 1
- 1.2 Soil-Structure Interaction 4

CHAPTER 2: KINEMATIC RESPONSE FUNCTIONS AND DYNAMIC STIFFNESSES OF BRIDGE EMBANKMENTS 9
- 2.1 Considerations for Response Analysis 9
- 2.2 Kinematic Response Functions 10
  - 2.2.1 The Shear Beam Approximation 11
  - 2.2.2 Finite Element Analysis 20
  - 2.2.3 Kinematic Response Functions 22
  - 2.2.4 Validation of Method — Crest Response 25
  - 2.2.5 Summary of Procedure to Compute the Kinematic Response Functions of Embankments 35
- 2.3 Dynamic Stiffnesses 38
  - 2.3.1 Resilience of Abutments 38
  - 2.3.2 The Shear Beam Approximation 40
  - 2.3.3 Finite Element Analysis 43
  - 2.3.4 Estimation of Critical Length L_c 50
  - 2.3.5 Summary of Procedure to Compute the Spring and Dashpot Values of Bridge Embankments 53

CHAPTER 3: DYNAMIC STIFFNESSES OF PILE FOUNDATIONS 57
- 3.1 Input Motion at Pile Caps 57
- 3.2 Dynamic Stiffnesses of Single Pile 58
  - 3.2.1 Lateral Dynamic Stiffness of a Single Pile 58
  - 3.2.2 Vertical and Rocking Dynamic Stiffnesses of a Single Pile 61
- 3.3 Dynamic Stiffnesses of Pile Group 63
  - 3.3.1 Lateral Dynamic Stiffness of Pile Group 63
  - 3.3.2 Vertical and Rocking Dynamic Stiffnesses of Pile Group 66
  - 3.3.3 Spring and Dashpot Values of the Pile Foundations of the Meloland Road Overcrossing and the Painter Street Overcrossing 67

3.4 Equivalent Flexural-Shear Beam 77
3.5 Summary of Procedure to Compute the Spring and Dashpot Values of Pile Foundations 79

CHAPTER 4: PREDICTION OF THE SEISMIC RESPONSE OF HIGHWAY OVERCROSSINGS 81
4.1 Response of the Meloland Road Overcrossing 81
4.1.1 Eigenvalue Analysis 84
4.1.2 Time History Analysis 92
4.2 Response of the Painter Street Overcrossing 100
4.2.1 Eigenvalue Analysis 100
4.2.2 Time History Analysis 108
4.3 Outline of Proposed Procedure 117

CHAPTER 5: CONCLUSIONS 119

REFERENCES 123

LIST OF FIGURES

Figure 1.1 General procedure for seismic soil-foundation-superstructure interaction 5

Figure 1.2 Schematic of a highway overcrossing and its idealized model 7

Figure 2.1 Cross section of infinitely long embankment (top); Isoparametric view of approach embankment (center); geometrical and material characteristics of embankments of three instrumented bridges in California (bottom) 12

Figure 2.2 Characteristic function (top) and first and second transverse modes (center and bottom) of shear-wedge model with variable cross sections 14

Figure 2.3 First natural frequency of prismatic embankment 15

Figure 2.4 Normalized soil shear modulus and damping coefficient ($\eta = 2\xi$) as a function of shear strain 17

Figure 2.5 Crest total acceleration, relative velocity, and relative displacement time histories computed with shear-beam approximation for Meloland Road Overcrossing embankment ($G=2.0MPa$, $\eta=0.52$) 19

Figure 2.6 Strain time histories at base, center, and near top of Meloland Road Overcrossing soil embankment computed with Rayleigh damping approximation ($G = 2.0MPa,$ $\eta= 0.52$, $\alpha = 2.3057$, and $\beta=2.9312x10^{-2}$) 21

Figure 2.7 Strain time histories at base, center, and near top of Painter Street Overcrossing soil embankment computed with Rayleigh damping approximation ($G= 8.0MPa$, $\eta = 0.50$, $\alpha = 3.6461$, and $\beta= 1.7140x10^{-2}$) 23

Figure 2.8 Kinematic response functions of Meloland Road Overcrossing embankment (left) and Painter Street Overcrossing embankment (right) 24

Figure 2.9 Elevation and plan views of Meloland Road Overcrossing along with locations of accelerometers 26

Figure 2.10 Recorded acceleration time histories at free field (left), north embankment (center),and south embankment (right) of Meloland Road Overcrossing during 1979 Imperial Valley earthquake 27

Figure 2.11 Transverse crest response of Meloland Road Overcrossing embankment computed with shear-beam approximation (left), two-dimensional finite element method (center), and three-dimensional finite element method (right) 29

Figure 2.12 Longitudinal crest response of Meloland Road Overcrossing embankment computed with shear-beam approximation (left), three-dimensional prismatic geometry (center), and three-dimensional tapered geometry (right) 30

Figure 2.13 Elevation and plan views of Painter Street Overcrossing along with locations of accelerometers 32

Figure 2.14 Recorded acceleration time histories at free field (left), west embankment (center), and east embankment (right) of Painter Street Overcrossing during 1992 Petrolia earthquake 33

Figure 2.15 Idealized soil profiles that emerged from refraction surveys (Heuze and Swift 1991) 34

Figure 2.16 Transverse crest response of Painter Street Overcrossing embankment computed with shear-beam approximation (left), two-dimensional finite element method (center), and three-dimensional finite element method (right) 36

Figure 2.17 Longitudinal crest response of Painter Street Overcrossing embankment computed with shear beam approximation (left), three-dimensional prismatic geometry (center) and three-dimensional tapered geometry (right) 37

Figure 2.18 Unit-width finite wedge (top) and infinitely tall wedge (bottom) 41

Figure 2.19 Transverse dynamic stiffnesses of shear-wedge model and solution of two-dimensional finite element formulation. Left: finite wedge on rigid support; Right: infinitely tall wedge. Material and geometrical properties are those of Meloland Road Overcrossing ($G = 2MPa$, $\eta = 0.52$, $z_0 = 2.59m$, $H = 7.92m$, and $B_c = 10.36m$) 44

Figure 2.20 Transverse dynamic stiffnesses of shear-wedge model and solution of two-dimensional finite element formulation. Left: finite wedge on rigid support; Right: infinitely tall wedge. Material and geometrical properties are those of Painter Street Overcrossing ($G = 8MPa$, $\eta = 0.50$, $z_0 = 3.81m$, $H = 9.6m$, and $B_c = 15.24m$) 45

Figure 2.21 Transverse and longitudinal loading imposed to obtain dynamic stiffness of approach embankment with material properties, G and η, supported on halfspace with material properties, G_h and η_h 47

Figure 2.22 Dynamic stiffnesses of approach embankment of Meloland Road Overcrossing ($G = 2.0MPa$, $\eta = 0.52$). Spring and dashpot values shown in Figure 1.1 are extracted by multiplying values shown above with width of embankment, B_c. Stiffness and damping values along longitudinal (y) direction are equal to those of transverse direction 48

Figure 2.23 Dynamic stiffnesses of approach embankment of Painter Street Bridge ($G = 8.0MPa$, $\eta = 0.50$). Spring and dashpot values shown in Figure 1.1 are extracted by multiplying values shown above with width of embankment, B_c. Stiffness and damping values along longitudinal (y) direction are equal to those of transverse direction 49

Figure 2.24 Free-body diagram of a section of a long embankment under transverse loading at one end 51

Figure 2.25 Critical-length parameter, $\alpha = K_x / (\hat{k}_x \sqrt{SB_cH})$ for various geometries 54

Figure 3.1 Comparison of storage (real part) and loss (imaginary part) stiffness factors along horizontal direction obtained with approximate analytical method (dashed lines) against rigorous solution of Kaynia and Kausel (solid line) for single pile (top) and 3 by 3 square group with rigid pile cap and pile spacing, $S/d = 5$ (bottom). $E_p/E_s = 1000$, $\rho_p/\rho_s = 1.42$, $L/d = 15$, $\beta_s = \eta/2 = 0.05$, $\nu = 0.4$, homogeneous halfspace 59

Figure 3.2 Comparison of storage (real part) and loss (imaginary part) stiffness factors along the vertical direction obtained with approximate analytical method (dashed lines) against rigorous solution of Kaynia and Kausel (solid line) for single pile (top) and 3 by 3 square group with rigid pile cap and pile spacing, $S/d = 5$ (bottom). $E_p/E_s = 1000$, $\rho_p/\rho_s = 1.42$, $L/d = 15$, $\beta_s = \eta/2 = 0.05$, $\nu = 0.4$, homogeneous halfspace 64

Figure 3.3 Cross-section view of Meloland Road Overcrossing and plan view of pile group at center bent 68

Figure 3.4 Plan view of pile groups at south and north abutments of Meloland Road Overcrossing 69

Figure 3.5 Cross-section view of Painter Street Overcrossing and plan view of pile group at center bent 70

Figure 3.6 Plan view of pile groups at west and east abutments of Painter Street Overcrossing 71

Figure 3.7 Dynamic stiffnesses of single pile and pile group at center bent of Meloland Road Overcrossing 72

Figure 3.8 Dynamic stiffnesses of single pile and pile group at center bent of Painter Street Overcrossing 73

Figure 3.9 Dynamic stiffnesses of single pile and pile group at abutments of Meloland Road Overcrossing 74

Figure 3.10 Dynamic stiffnesses of single pile and pile group at west abutment of Painter Street Overcrossing 75

Figure 3.11 Dynamic stiffnesses of single pile and pile group at east abutment of Painter Street Overcrossing 76

Figure 4.1 Numerical models of Meloland Road Overcrossing (Top: stick model; Bottom: 3D finite element model) 82

Figure 4.2 First six natural frequencies and modes computed by stick model (left) and 3D FEM model (right) of Meloland Road Overcrossing 85

Figure 4.3 Fourier amplitude of recorded accelerations of channels 7, 8, 9, and 13 of Meloland Road Overcrossing 91

Figure 4.4 Records of channel 7 and predictions of Meloland Road Overcrossing response considering different support motions 93

Figure 4.5 Records of channel 8 and predictions of Meloland Road Overcrossing response considering different support motions 94

Figure 4.6 Records of channel 9 and predictions of Meloland Road Overcrossing response considering different support motions 95

Figure 4.7 Records of channel 13 and predictions of Meloland Road Overcrossing response considering different support motions 96

Figure 4.8 Bridge models with different support idealizations 97

Figure 4.9 Records of channel 7 and predictions of Meloland Road Overcrossing response considering different support idealizations 98

Figure 4.10 Records of channel 9 and predictions of Meloland Road Overcrossing response considering different support idealizations 99

Figure 4.11 Numerical models of Painter Street Bridge (Top: stick model; Bottom: 3D finite element model) 101

Figure 4.12 First six natural frequencies and modes computed by stick model (left) and 3D FEM model (right). Values in parentheses are those reported by McCallen and Romstad (1994) 102

Figure 4.13 Fourier amplitude of recorded accelerations of channels 4, 7, 9, and 11 of Painter Street Bridge 107

Figure 4.14 Records of channel 4 and predictions of Painter Street Overcrossing response considering different support motions 109

Figure 4.15 Records of channel 7 and predictions of Painter Street Overcrossing response considering different support motions 110

Figure 4.16 Records of channel 9 and predictions of Painter Street Overcrossing response considering different support motions 111

Figure 4.17 Records of channel 11 and predictions of Painter Street Overcrossing response considering different support motions 112

Figure 4.18 Records of channel 4 and predictions of Painter Street Overcrossing response considering different support idealizations 113

Figure 4.19 Records of channel 7 and predictions of Painter Street Overcrossing response considering different support idealizations 114

Figure 4.20 Records of channel 9 and predictions of Painter Street Overcrossing response considering different support idealizations 115

Figure 4.21 Records of channel 11 and predictions of Painter Street Overcrossing response considering different support idealizations 116

LIST OF TABLES

Table 2.1 Comparisons of estimated abutment/embankment stiffnesses 39

Table 3.1 Spring and dashpot values of the pile groups of interest 77

Table 4.1 Spring and dashpot values that approximate the presence of the approach embankments and pile foundation of the Meloland Road Overcrossing. Values from this study are associated with the intensity of the 1979 Imperial Valley earthquake 83

Table 4.2 Modal frequencies, ω_j (rad/s), and damping ratios, ξ_j (%), of the Meloland Road Overcrossing 89

Table 4.3 Spring and dashpot values that approximate the presence of the approach embankments and pile foundations of the Painter Street Overcrossing. Values from this study are associated with the intensity of the 1992 Petrolia earthquake 104

Table 4.4 Modal frequencies, ω_j (rad/s), and damping ratios, ξ_j (%), of the Painter Street Overcrossing 106

1 Introduction

1.1 BACKGROUND

Over the last thirty years several highway overcrossings have experienced severe damage under strong ground shaking. Most of this damage was the result of excessive seismic displacements and deflections that have been substantially underestimated during design. Such design deficiencies appear to be the result of dated design concepts, which typically considered a small fraction of the actual forces and displacements that develop on bridges during strong earthquake shaking. A direct consequence of the underestimated seismic displacements, which were the combined result of poor representation of the kinematic characteristics of the ground, low lateral forces, and overestimated stiffnesses, was that the seating length at the deck supports was unrealistically short and the lateral separations between adjacent structures were typically inadequate, resulting in loss of support or pounding (Maragakis and Jennings 1987). These geometrical inconsistencies resulted in spectacular failures that have been witnessed during the recent 1989 Loma Prieta and the 1994 Northridge earthquakes in California and the 1995 Kobe earthquake in Japan. In addition to failures that are the result of geometric inconsistencies (limited seating length, pounding-abutment slumping), several bridges failed due to inadequate strength and ductility in their columns, cap-beams, and foundations (Priestley et al. 1996).

In view of these failures, many research programs were launched after the 1971 San Fernando earthquake to study the seismic resistance of highway bridges. Improvements have been achieved in both design and analysis of bridge structures with the help of strong-motion records. Extensive retrofit programs have been implemented in California, which include jacketing of columns and the use of composite materials (FHWA 1995).

An alternative strategy for the seismic protection of bridges that the California Department of Transportation (Caltrans) is currently investigating is the implementation of devices such as isolation bearings and supplemental dampers. Several bridges worldwide are equipped with seismic protection devices (Skinner et al. 1993). The increasing need for safer bridges in association with the rapid success of seismic protection devices in buildings has accelerated the implementation of large-capacity damping devices in bridges (Delis et al. 1996). Typically bridges and, in particular, freeway overcrossings are more sensitive than buildings to soil-structure interaction, yet the potentially important effects of soil-structure interaction are often downplayed or occasionally neglected even in relatively sophisticated studies that consider the implementation of modern technologies. These concerns and conclusions from system identification studies that indicate that once damping is beyond 20% of critical its effect is marginal even if it is augmented to 40% (Wilson and Tan 1990a,b), generated the need for a comprehensive study that will elucidate the effectiveness of supplemental damping in freeway overcrossings.

The motivation for this study did not originate from a lack of published material on the seismic response of freeway overcrossings but rather from an abundance of publications, the vast numbers of which present findings that are scattered, occasionally conflicting, and derived from various methodologies that in many occasions have little in common. As a result, despite several existing recommendations (Werner 1994; Goel and Chopra 1997, among others) there is no established procedure that results in a dependable estimate of the seismic response of freeway overcrossings, partly because the findings of the below-mentioned studies have not been combined in a rational manner that will result in a systematic analysis procedure.

Most of the work published on this class of bridge structures was motivated from the availability of strong-motion response data from two representative bridges which have been instrumented by the Strong Motion Instrumentation Program (SMIP) of the California Division of Mines and Geology. The two representative bridges are the Meloland Road Overcrossing that was subjected to the 1979 Imperial Valley earthquake and the Painter Street Bridge that was subjected to the 1992 Petrolia earthquake.

In this report we also use the data from these two aforementioned overcrossings to develop and validate a step-by-step simple, yet sound, procedure to estimate the seismic response of freeway overcrossings. Our goal is not to derive another isolated study, but rather to build on the work of others. Many past publications are used in this study to validate deformation levels, material parameters, and response quantities. Agreements between our results and those of other investigators further establish the dependability of the proposed procedure, while discrepancies in response quantities have been the motivation for the additional studies presented herein.

The seismic response of freeway overcrossings received distinct attention in the late 1980s. Maragakis and Jennings (1987) introduced the “stick model” enhanced with bilinear “springs” and “dashpots” at its support to study the motion of skew overpasses. While their model accounted for several practical difficulties such as the presence of elastometric pads and the gap between the deck and the back wall, the estimation of model parameters was presented in a hasty manner. Werner et al. (1987) developed a system identification methodology to extract information from an array of strong-motion measurements that were recorded in the vicinity of the Meloland Road Overcrossing during the 1979 Imperial Valley earthquake. Their conclusions emphasized the ability of linear models to fit the measured response and the pronounced effects that the approach embankments and foundations have on the response of the bridge. Although their paper identifies relatively low values of modal damping for the bridge-foundation system ($\xi_i = 6\%$ to 8%), a later publication by Werner (1994) indicates modal damping ratios ranging from 19% to 26%. About the same time, Crouse et al. (1987) conducted experimental and analytical studies to determine the significance of soil-structure interaction on the response of a single span overcrossing with monolithic abutments on spread footings. The small displacement gradient generated from the ambient quick-release and forced-vibration tests resulted in small values of damping and large values of stiffness that are not representative under earthquake loading. The present report essentially builds on and extends the work of Wilson and Tan (1990a, b), Werner (1994), Goel and Chopra (1997), McCallen and Romstad (1994) and Makris et al. (1994).

Wilson and Tan (1990a) was the first study that presented a simple analytical model to estimate the static transverse and vertical stiffnesses of approach embankments of typical short- and medium-span highway bridges. Their closed-form expressions that account for the sloped geometry of the embankment provide a realistic estimate of the static stiffnesses of a unit-width wedge and are consistent with the shear-wedge model that can be easily used to estimate the amplification functions of approach embankments. Their study, however, did not provide any information on the embankment stiffnesses along the longitudinal direction nor any information on the embankment damping in any direction. Furthermore, in their companion paper (Wilson and Tan 1990b) while initial calculations resulted in a soil shear modulus as low as $G = 2.4MPa$, subsequent values of the embankment stiffnesses are calculated using a shear modulus value as high as $G = 7.2MPa$ (three times larger). In this report, the concept of the shear-wedge model established by Wilson and Tan (1990a,b) is utilized to develop kinematic response functions and dynamic stiffnesses (stiffness and damping) of the approach embankments. A dependable estimation of the crest response not only allows for a more appropriate support motion at the end abutments but also reveals realistic levels of dynamic strains which are subsequently used to estimate the stiffness and damping coefficients of embankments.

The work of S. D. Werner and others on two-span short bridge overcrossings was summarized in a paper in an effort to evaluate Caltrans procedures for seismic response analysis of freeway overcrossings (Werner 1994). That study underlined the significance of soil-structure interaction and offered selected recommended values on some modal parameters. Emphasis was given to the transverse response of the bridge. As in the Wilson and Tan (1990a) study, the Werner (1994) study did not provide any information on the embankment stiffnesses and damping along the longitudinal direction. Information on modal response quantities was limited to the first transverse mode only. Despite its limitations and occasional sweeping statements, the Werner (1994) study identifies several of the challenges associated with this problem. This study revisits the Werner (1994) paper by refining and extending several of the concepts advanced therein.

The development of realistic values of kinematic response functions and dynamic stiffnesses of the approach embankments and pile foundations (which are also presented in this report) are used to synthesize a simple dynamic model to estimate the dynamic response of freeway overcrossings. The numerical simulations that employ a simple stick model and a more sophisticated finite element model build on the work presented by McCallen and Romstad (1994). Nevertheless, the methodology presented in this study adopts the substructure approach, where the kinematic response functions and dynamic stiffnesses are computed separately and subsequently are incorporated in a simple dynamic model where the mechanical behavior of each of its components can be calculated with any desired level of sophistication.

Lastly, the structural characteristics that we compute for the Painter Street Overcrossing are compared with those reported by Goel and Chopra (1997), who employed an equilibrium-based approach to back-figure abutment stiffnesses at different levels of shaking. The follow-up work of Goel (1997) is also used to compare the estimated values of modal periods and damping ratios of the entire bridge-foundation system.

1.2 SOIL-STRUCTURE INTERACTION

Figure 1.1(a) shows the schematic of a typical two-span overcrossing with its approach embankments. During ground shaking the dynamic response of the deck is affected: (a) from the dynamic

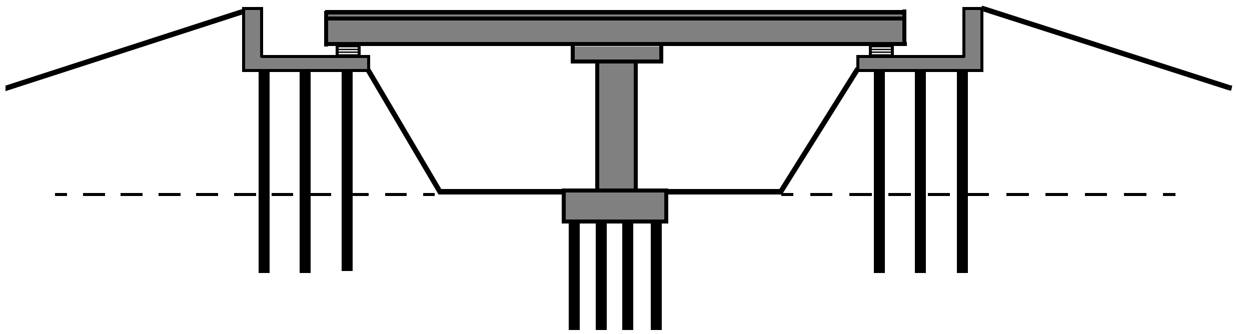

(a) Real System

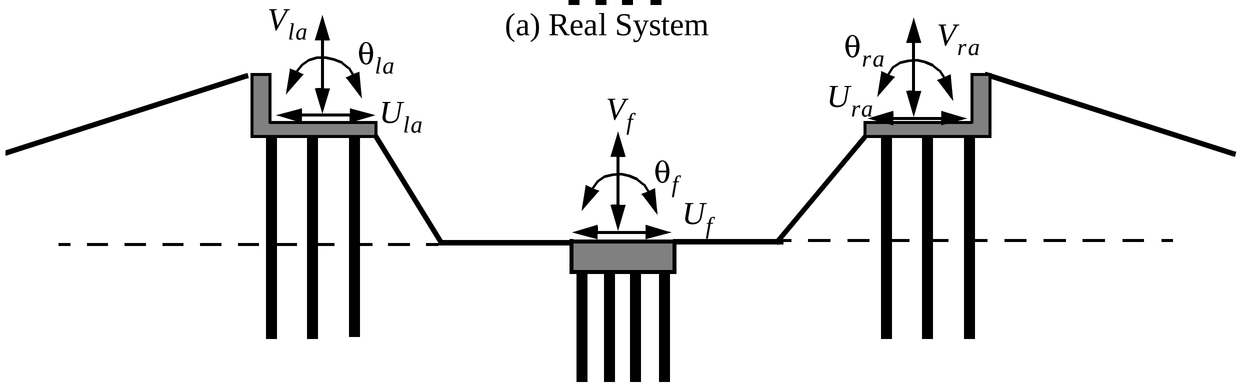

(b) Kinematic-Seismic Response

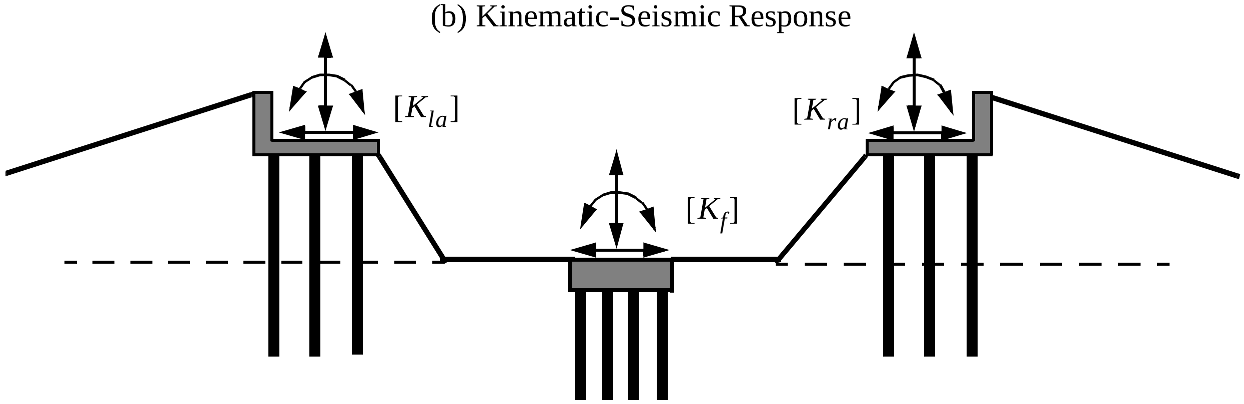

(c) Dynamic Stiffnesses of Pile Group and Embankments

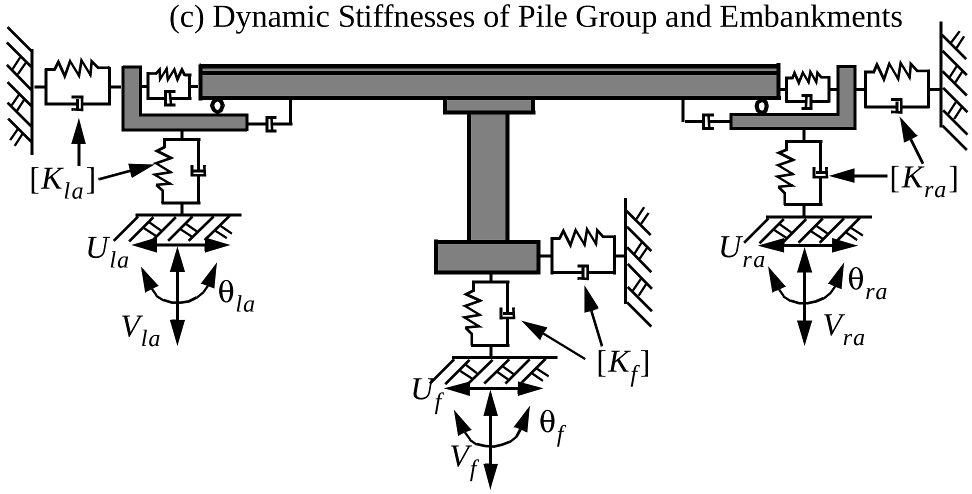

(d) Idealization of Soil-Bridge Interaction

Figure 1.1. General procedure for seismic soil-foundation-superstructure interaction

response of the embankments that support the end abutment and (b) from the dynamic response of the pile foundations at the center bent. The need to account for this interaction motivated finite element studies that involved the discretization of the bridge superstructure and a large volume of the embankments and supporting soil (Sweet 1993; McCallen and Romstad 1994 among others). Although such studies elucidated the significance of deck-abutment-embankment interaction, they do not provide direct information on the distinct mechanical characteristics of approach embankments and pile foundations and their influence on the dynamic response of the bridge structure. This might be a possible reason for the lack of practical procedures to account for soil-structure interaction when computing the seismic response of freeway overcrossings. This report concentrates on addressing the issue of the importance of soil-structure interaction on the seismic response of freeway overcrossings and presents practical methodologies to include its effect in association with simple bridge models.

Owing to its computational efficiency the substructure method is a popular approach to address the soil-foundation-superstructure problem (Tseng and Penzien 2000). Assuming linear soil-foundation-superstructure response, the analysis of the system can be performed in three consecutive steps as shown in Figure 1.1. First, find the motion at the end abutments and pile cap of the center bent in the absence of the bridge superstructure (the so-called foundation input motion), which includes translational as well as rotational components; second, determine the dynamic stiffnesses (frequency dependent springs and dashpots) associated with longitudinal, transverse, vertical, rocking and cross-horizontal-rocking oscillations of the embankments and pile groups; third, compute the seismic response of the superstructure (deck and abutments) supported on springs and dashpots and subjected to the foundation input motion.

An earlier attempt to investigate the effect of soil-pile-structure interaction was presented by Makris et al. (1994). In that study the Painter Street Overcrossing was idealized with a plane six-degree-of-freedom lumped-parameter model, whereas the influence of the approach embankments was neglected. The limitations of the plane model restricted the analysis of the response only along the transverse direction. Despite its limitations, the study indicates some of the shortcomings that may result by neglecting the resilience of the pile foundations at the center bent and outlines a simple integrated procedure that one can follow in order to compute the stiffnesses and damping of pile foundations. The same procedure was adopted and extended in this study which examines the two-dimensional coupled longitudinal and transverse response of highway overcrossings. Figure 1.2 shows the elevation and plan views of the model adopted in this study and

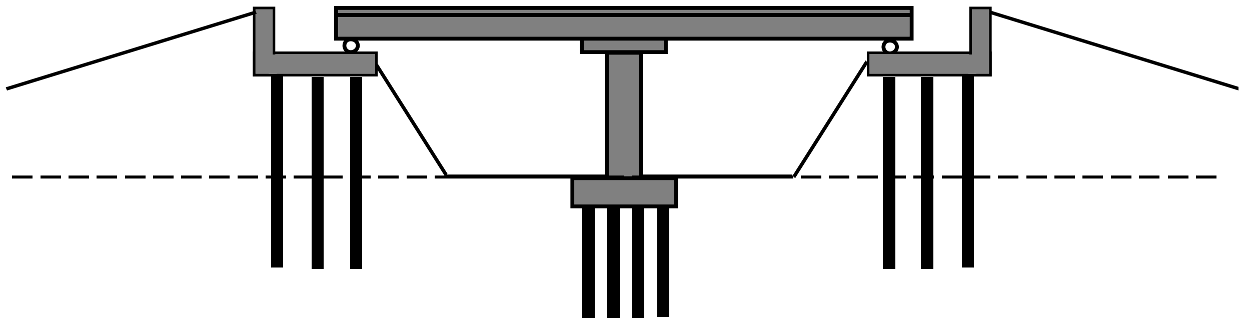

(a) Real System

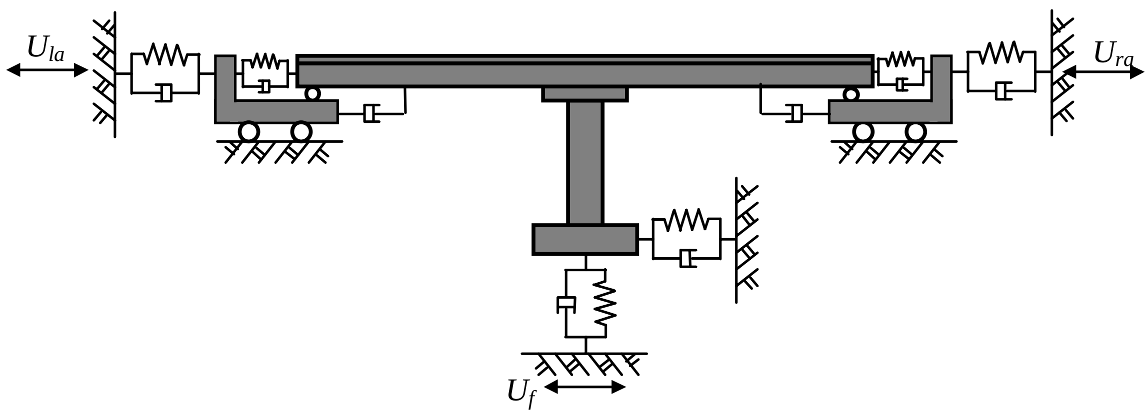

(b) Elevation View of Idealized Model

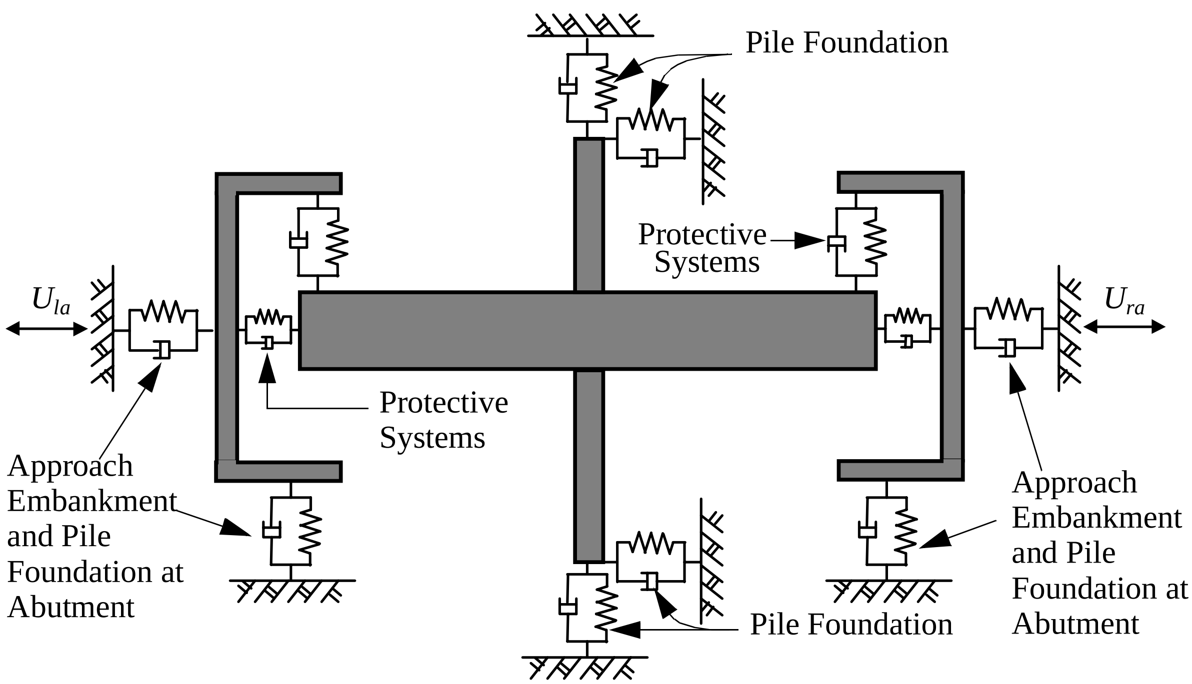

(c) Plan View of Idealized Model

Figure 1.2. Schematic of a highway overcrossing and its idealized model

the springs and dashpots that are proposed to approximate the interaction of the bridge superstructure with its foundation and the surrounding soil.

2 Kinematic Response Functions and Dynamic Stiffnesses of Bridge Embankments

2.1 CONSIDERATIONS FOR RESPONSE ANALYSIS

Understanding of the dynamic response of embankments has been substantially advanced due to a large number of studies on the seismic response of earth dams (Chopra 1967). During the last two decades a considerable amount of published research has focused on refining, expanding and verifying the basic dynamic models developed in the 1960s for predicting the seismic response of earth dams and embankments. As a result several improved analytical models have appeared by which parametric studies have been performed to elucidate the importance of dam geometry and material inhomogeneity (Dakoulas and Gazetas 1985, 1986). Many of these early studies conducted limit state analysis on the stability of embankments or concentrated on the dependability of proposed liquefaction procedures. The behavior of bridge embankments at their limit states is beyond the scope of this report.

In this chapter we focus on developing dependable amplification functions, together with springs and dashpots that can replace the presence of the bridge embankments with various geometries. It is well known from experimental studies (Romstad et al. 1995) and theoretical considerations (Siddharthan et al. 1997, among others) that the behavior of bridge abutments is increasingly nonlinear as displacement increases. Nevertheless, analytical studies on recorded motions have indicated that even under strong earthquake motion the force-displacement loops of bridge abutments resemble elliptical shapes (Goel and Chopra 1997). Earlier studies that were based on a system identification methodology indicated that linear models provide a good fit with the measured response of a bridge (Werner et al. 1987). Such observations indicate that even for the design earthquake an equivalent linear analysis can provide dependable estimates of the bridge response.

Strong-motion records near and on highway overcrossings revealed that the crest motion of the approach embankment can be more than two times the motion recorded near the pile cap of the center bent (Maroney et al. 1990), indicating that the kinematic response of embankments might have a substantial effect on the bridge response. No established procedures are presently available to account for this amplification. Current design procedures used by Caltrans (1989) assume only an equivalent linear distributed spring to approximate the resilience of the embankment without considering the energy absorbed by the embankment and the overall dynamic nature of the problem. Apparently, the evaluation of such quantities is not of prime interest when a traditional design is adopted, since the entire design philosophy is based on strength. When, however, the evaluation of displacements is of prime interest, a more detailed analysis is needed, since it has been stressed by several researchers that the effect of soil-structure interaction is increasingly important as the intensity of the ground shaking increases.

The numerical study presented herein is conducted within the context of equivalent linear viscoelasticity and is based on a three-dimensional (3-D) finite element analysis that is partly used to validate the dependability of approximate transfer functions and dynamic stiffnesses computed with the shear-wedge model. The proposed transfer functions, springs and dashpots, are expected to improve the estimation of displacements and forces that develop at the end abutments. It is shown that the presented formulation provides dependable estimates of the response even under larger abutment displacements when the soil of the embankment is strained in the nonlinear range. Evaluation of realistic energy dissipation levels together with the resilience of the embankments will provide more dependable indications on the need to equip overcrossings with supplemental dampers.

2.2 KINEMATIC RESPONSE FUNCTIONS

The approach earth embankments on many highway overcrossings usually have a length that is several times larger than the dimension of the trapezoidal cross section of the embankment. Typical approach embankments of highway overcrossings extend 150 m or more beyond each end abutment of the bridge. Because of this geometry several researchers have adopted a two-dimensional (2-D) plane-strain idealization to derive approximate response quantities.

2.2.1 The Shear Beam Approximation

Sixty years ago, Mononobe (1936) was perhaps the first to consider that earth dams and embankments are deformable bodies, and introduced the ingredients of what has come to be called the “shear-wedge” or the “shear-beam” model. This concept has served as the basis for many of the newly developed models and has been revisited in detail in the review paper by Gazetas (1987). In this section the shear-wedge or the shear-beam model is discussed briefly to show the advantages and limitations of a one-dimensional (1-D) approximation when applied to three-dimensional approach embankments.

Figure 2.1 (top) represents the cross section of an infinitely long embankment subjected to a horizontal rigid-base excitation, $\ddot{u}_g(t)$, under the condition of plane strain deformations. Assuming that only horizontal shearing deformations develop and that horizontal displacements are uniform across the embankment ($u_x(z, t)$ are independent of x), the dynamic equilibrium of a slice of the embankment gives

$$\rho_s \frac{\partial^2}{\partial t^2}[u_x(z,t) + u_g(t)] = \frac{1}{z}\frac{\partial}{\partial z}\left(G_s(z) \cdot z \cdot \frac{\partial}{\partial z} u_x(z,t)\right) \tag{2.1}$$

where ρ_s and $G_s(z)$ are the density and the shear modulus of the soil material of the embankment. In general the shear modulus, $G_s(z)$, is a function of z. For instance, a reasonable assumption is to assume that $G_s(z)$ is proportional to the square root of the confining pressure (Gazetas 1987). In this study the shear modulus of the embankment has been assumed to be a constant.

Under free vibrations ($u_g(t) = 0$), the solution of equation (2.1) gives the free vibration characteristics of the shear-wedge. The natural frequencies, ω_n, are given by

$$\omega_n = k_n V_s \tag{2.2}$$

where $V_s = \sqrt{G_s/\rho_s}$, is the shear-wave velocity of the soil material and k_n is the nth wave number that is obtained from the solution of the characteristic equation

$$J_0[k_n(z_0 + H)]Y_1(k_n z_0) - J_1(k_n z_0)Y_0[k_n(z_0 + H)] = 0 \tag{2.3}$$

The value of the constant z_0 depends on the geometry of the embankment. In the general case of an unsymmetrical embankment, $z_0 = B_c H/(B_b - B_c)$; whereas in the case of a symmetric embank-

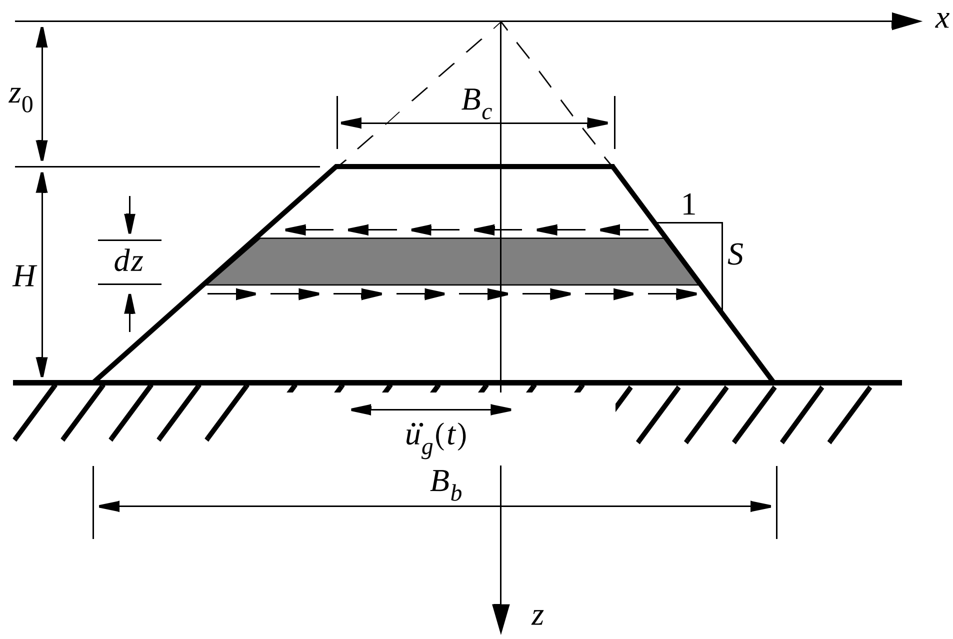

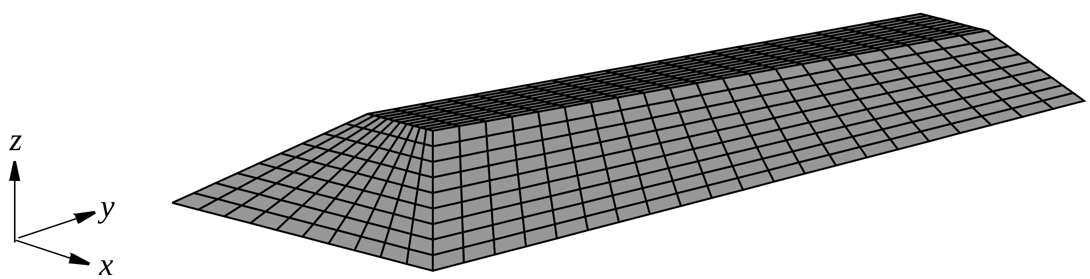

Geometry/Material Parameter	Meloland Road Overcrossing	Painter Street Overcrossing	91/5 HOV
B_c	34' (10.36 m)	50' (15.24 m)	42.5' (12.95 m)
H	26' (7.92 m)	31.5' (9.60 m)	36' (10.97 m)
S	1/2	1/2	1/2
ρ_s	1600 kg/m^3	1600 kg/m^3	1800 kg/m^3
V_s	110 m/s	200 m/s	200 m/s
Configuration	symmetric	symmetric	unsymmetric

Figure 2.1. Cross section of infinitely long embankment (top); isoparametric view of approach embankment (center); geometrical and material characteristics of embankments of three instrumented bridges in California (bottom)

ment with slope S, $z_0 = SB_c/2$. B_c is the crest width and H is the height of the embankment. The geometrical characteristics of three approach bridge embankments of interest, two of which have been instrumented and subjected to strong shaking are shown in Figure 2.1 (bottom). In equation (2.3) J_0, J_1, Y_0, and Y_1 are the zero- and first-order Bessel functions of the first and second kind respectively (Abramowitz and Stegun 1970). The mode shapes are given by

$$\phi_n(z) = J_0(k_n z)Y_1(k_n z_0) - J_1(k_n z_0)Y_0(k_n z) \tag{2.4}$$

Figure 2.2 plots the characteristic function (top) together with the first (center) and second (bottom) mode of a symmetric wedged beam for different values of the slope, S. Figure 2.3 compares the shear-wedge solution for the first undamped natural frequency of trapezoidal embankments with various slopes with the 2-D finite element solution that assumes plane strain conditions and the 3-D finite element solution of trapezoidal nonprismatic embankments with finite length that is equal to 10 times the width of the crest near the abutment. In the 3-D solution an approaching slope, *i=5%*, is assumed. An isoparametric sketch of a trapezoidal nonprismatic embankment is shown in Figure 2.1 (center).

When the ground input in (2.1) is a harmonic motion, $u_g(t) = u_{g0}e^{i\omega t}$ of frequency ω, equation (2.1) can be solved analytically. The quantity of interest is the ratio of the amplitude of the crest motion, $|u_x(z_0) + u_g|$, to the amplitude of the base motion, u_g. This transfer function is the kinematic response function of the shear wedge and is given by

$$|I(\omega)| = \left|1 + \frac{u_x(z_0)}{u_{g0}}\right| = \left|\frac{c_1 J_0(kz_0) + c_2 Y_0(kz_0)}{u_{go}}\right| \tag{2.5}$$

where $k = \omega/V_s$. c_1 and c_2 are integration constants given by

$$c_1 = \frac{u_{g0}}{J_0(k(z_0 + H)) - \dfrac{J_1(kz_0)}{Y_1(kz_0)}Y_0(k(z_0 + H))} \tag{2.6}$$

$$c_2 = -\frac{J_1(kz_0)}{Y_1(kz_0)}c_1 \tag{2.7}$$

In the case where the soil is assumed as a purely elastic material, its shear modulus is real and the kinematic response function given by (2.5) is singular at all natural frequencies given by (2.2). In reality soil material has internal damping and the kinematic response function is finite along the entire frequency spectrum. Experimental studies in the 1960s indicated that the storage and loss modulus of sand is nearly frequency independent (Hardin 1965). Following Hardin's pioneering

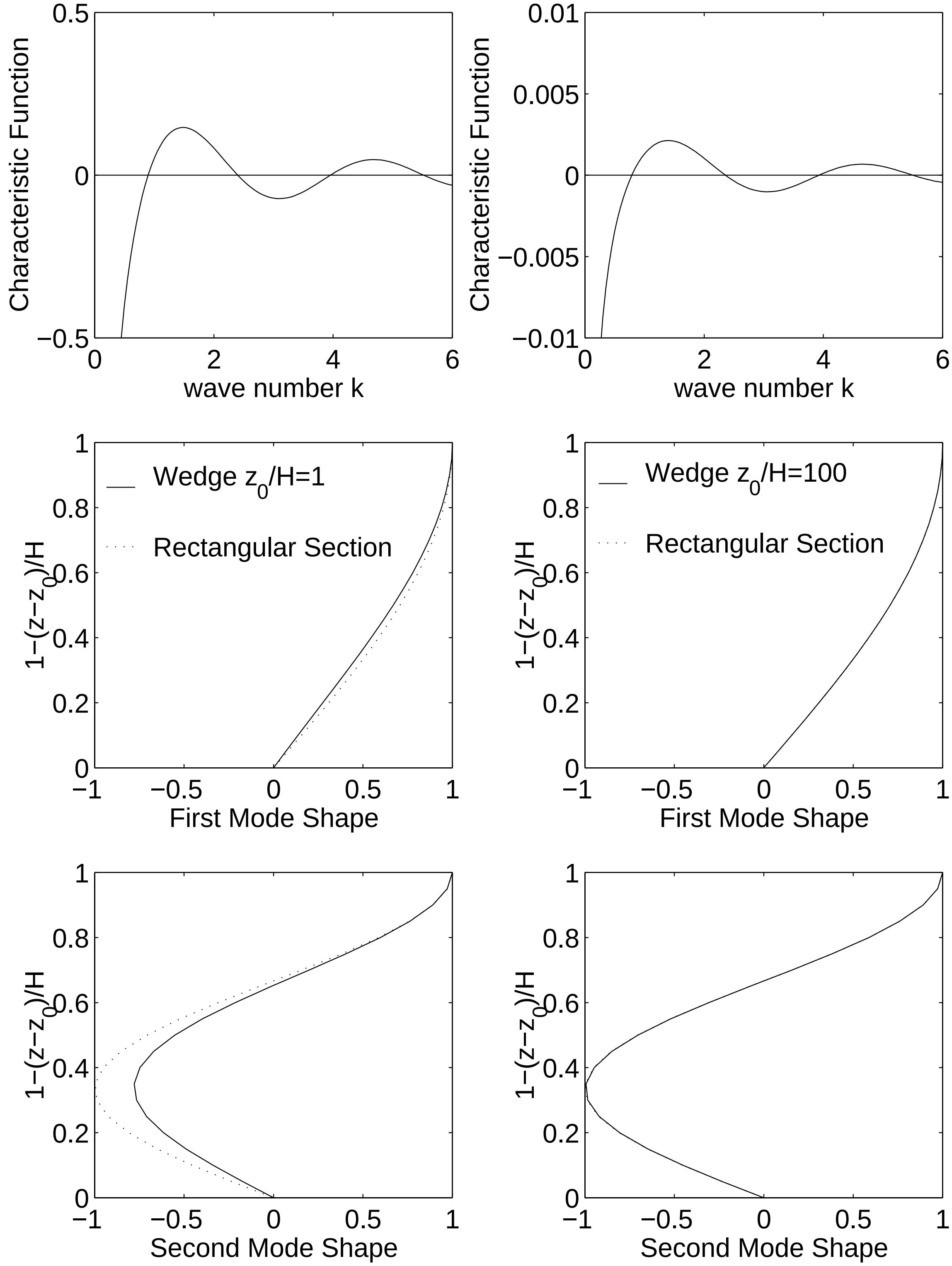

Figure 2.2. Characteristic function (top) and first and second transverse modes (center and bottom) of shear-wedge model with variable cross sections

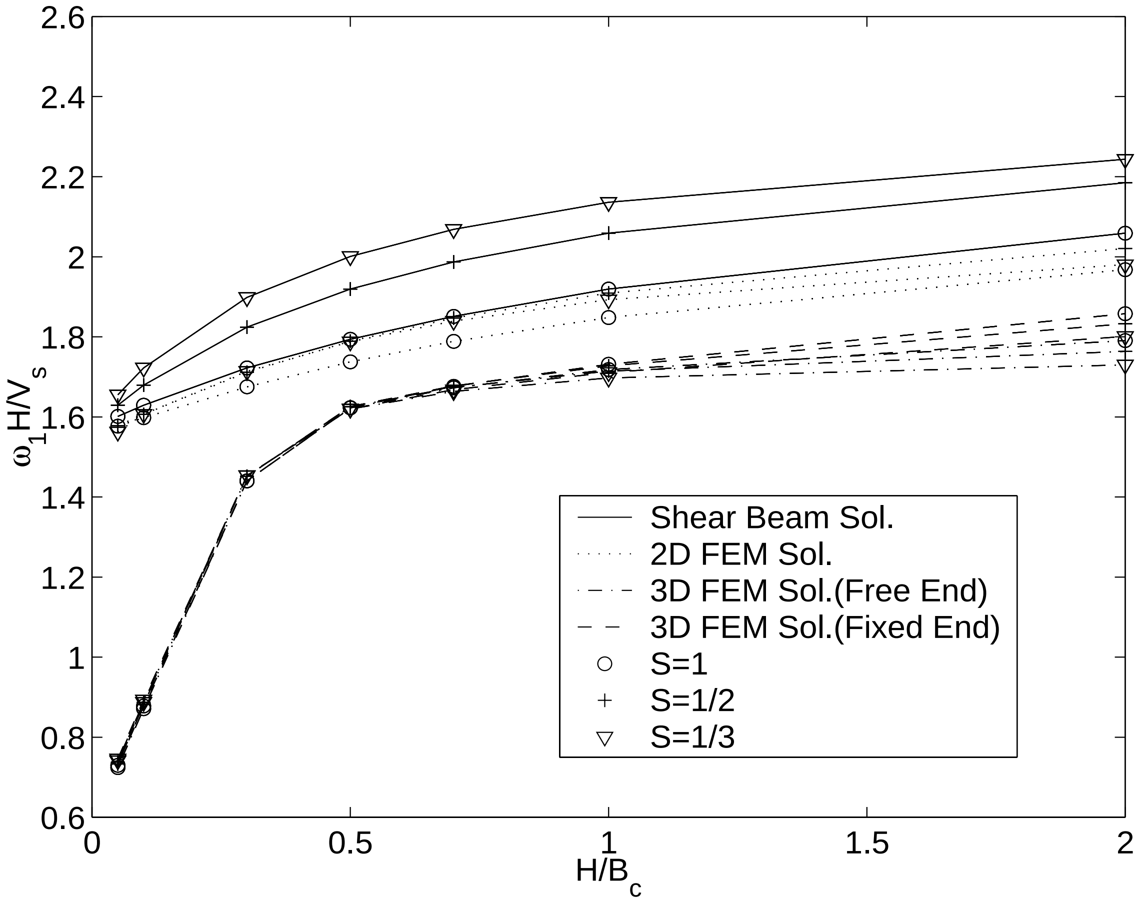

Figure 2.3. First natural frequency of prismatic embankment

work it has become a practice to use the following simple expression of the dynamic modulus of soil materials

$$G(\omega) = G_1 + iG_2 \mathrm{sgn}(\omega) = G_1(1 + i\eta\, \mathrm{sgn}(\omega)) \tag{2.8}$$

where G_1 and G_2 are frequency independent quantities and ω is the frequency variable. The signum function $\mathrm{sgn}(\omega)$ is appended at the imaginary part of (2.8) so that the loss modulus of the proposed model is an odd function of frequency. This condition ensures that under a real valued strain history, $\gamma(t)$, with Fourier transform, $\gamma(\omega) = \int_{-\infty}^{\infty} \gamma(t) e^{-i\omega t} dt$, the resulting stress history

$$\tau(t) = \frac{1}{2\pi}\int_{-\infty}^{\infty} (G_1 + iG_2 \mathrm{sgn}(\omega))\gamma(\omega) e^{i\omega t} d\omega \tag{2.9}$$

is real valued. Since the real part, G_1 (storage modulus) in (2.8) is frequency independent it assumes the static value of the shear modulus of the material G_s; whereas the constant, $\eta = G_2 / G_1$, appearing in (2.8) is the hysteretic damping coefficient. Accordingly the constant hysteretic model has been traditionally expressed as $G(\omega) = G_s(1 + i\eta\, \mathrm{sgn}(\omega))$, where G_s and η are strongly strain dependent. Figure 2.4 plots selected curves published in the literature based on the work of Seed and Idriss (1970), Iwasaki et al. (1978), Tatsuoka et al. (1978), Vucetic and Dobry (1991), among others. The darker line on Figure 2.4 represents an averaged curve of these reported curves, and is the curve used for iteration in this report. Note that in the bottom of Figure 2.4 the material damping of soil is presented in terms of $\eta = G_2 / G_1$ and not in terms of the modal damping of the embankment, ξ_n. It should be noted that the constant hysteretic model given by (2.8) is a pathological model since it does not process a real-valued constitutive law in the time domain. The main flaw of this model that is due to its noncausality is well known to the literature (Caughey 1962; Crandall 1963, 1970; Inaudi and Kelly 1995) and has been rigorously addressed by Makris (1997) and Makris and Zhang (2000). Despite its noncausal behavior the constant hysteretic model given by (2.8) is a reliable model for the dynamic analysis of earth structures, in particular when the excitation has several cycles.

Using the correspondence principle (Flugge 1975) the harmonic response of an embankment that consists of viscoelastic material is given from the same equations that are derived by assuming a purely elastic material after replacing the real shear modulus, G_s, with the complex shear modulus $G_s(1 + i\eta\, \mathrm{sgn}(\omega))$. With this substitution the shear-wave velocity, V_s, and natural frequencies, ω_n, become complex quantities. As an example, the modal frequencies, ω_n, are given by

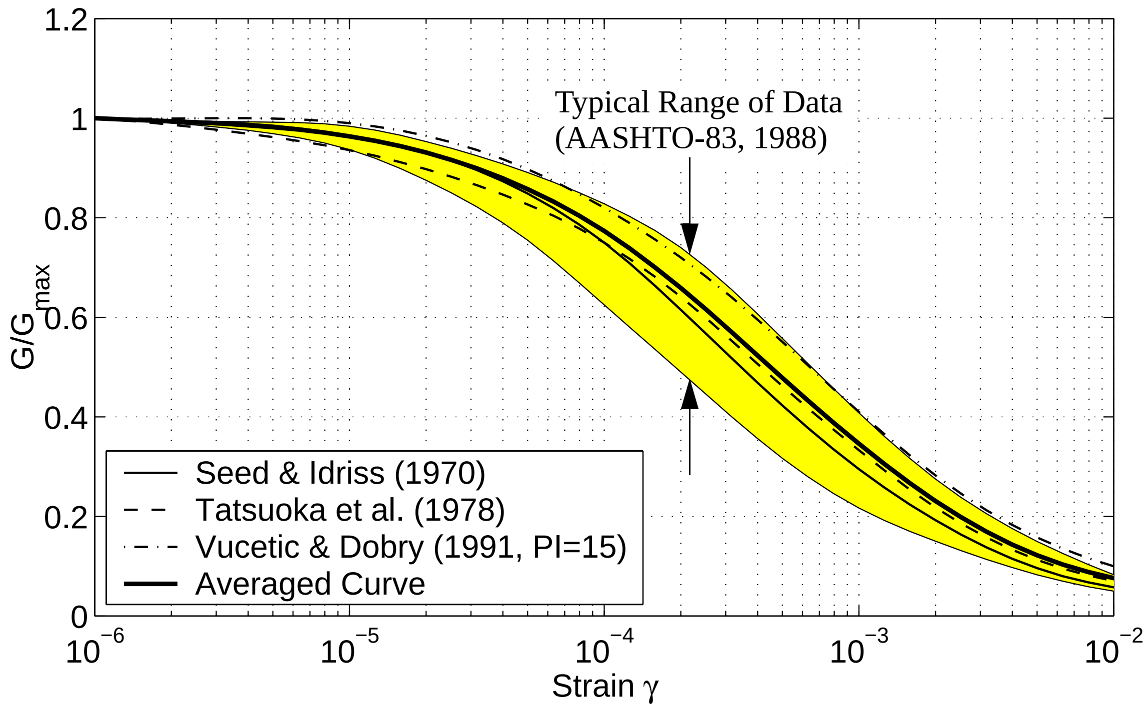

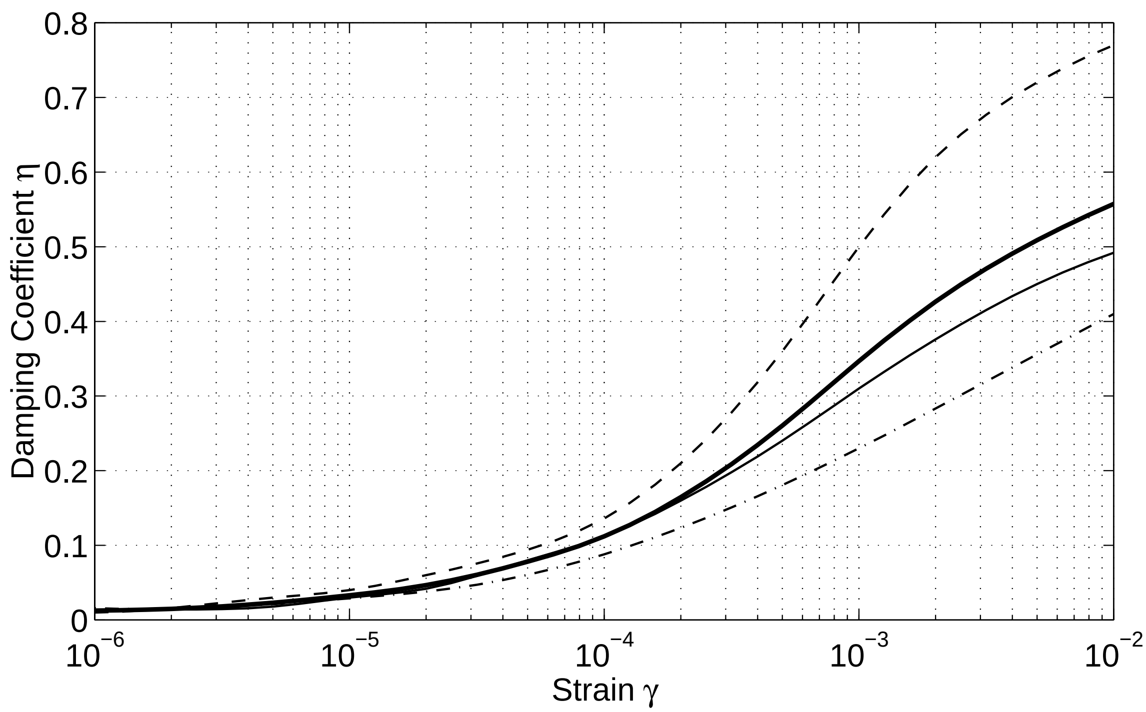

Figure 2.4. Normalized soil shear modulus and damping coefficient ($\eta = 2\xi$) as function of shear strain

$$\omega_n = k_n\sqrt{\frac{G_s}{\rho_s}}\cdot\sqrt{1+i\eta} \tag{2.10}$$

in which k_n is again the nth wave number that is obtained from the solution of the characteristic equation (2.3). The modal damping ratio, ξ_n, is given by

$$\xi_n = \frac{Im\{\omega_n\}}{\sqrt{(Re\{\omega_n\})^2+(Im\{\omega_n\})^2}} \approx \frac{\eta/2}{1+\eta^2/8} \approx \frac{1}{2}\eta \tag{2.11}$$

It is important to emphasize that the modal damping ratio, ξ_n, appearing on the left of equation (2.11), is a quantity that characterizes the modal damping of the entire soil embankment; whereas, the hysteretic damping coefficient, $\eta = G_2/G_1$, appearing on the right of (2.11), characterizes the dissipation of the soil material at a point. It is partly because of the simple relation give by (2.11) that the modal damping ratio and the hysteretic damping coefficient are often confused in the literature without distinguishing between the modal damping ratio of an entire structure, ξ_n, and the loss factor, η, of a viscoelastic material.

In selecting the values of G and η iterations are required, since their values are strain dependent and the strain level is not known a priori. Initially, a strain level is projected, the associated shear modulus and damping coefficient are estimated, and response time histories are computed. Seed and Idriss (1969) suggested that two thirds of the response strain should be used as the average strain to evaluate $G(\gamma)$ and $\eta(\gamma)$ for the next iteration. With a finite element analysis different values of soil parameters can be assigned at various locations according to local strain level (Idriss et al. 1974). With the shear-wedge formulation only a macroscopic value of an average strain $\hat{\gamma} = \hat{u}_x^c/H$ can be evaluated, where $\hat{u}_x^c$ is some representative crest displacement (say $\hat{u}_x^c = \frac{2}{3}u_{x,\,max}^c$) and H is the height of the shear wedge.

The dependability of the shear-wedge model to predict the transverse seismic response of bridge embankments is illustrated by examining the crest response of the embankments of the Meloland Road Overcrossing (Werner et al. 1987) and the Painter Street Bridge (McCallen and Romstad 1994). Each embankment is subjected to the corresponding free-field horizontal motion recorded during the 1979 Imperial Valley earthquake and the 1992 Petrolia earthquake. The two input motions are shown in figures 2.10 and 2.14 (left column).

Figure 2.5 shows computed crest relative displacement, relative velocity and total acceleration histories of a shear wedge with the physical and geometrical characteristics of the embankment of the Meloland Road Overcrossing (see Figure 2.1). The input motion is the one shown in

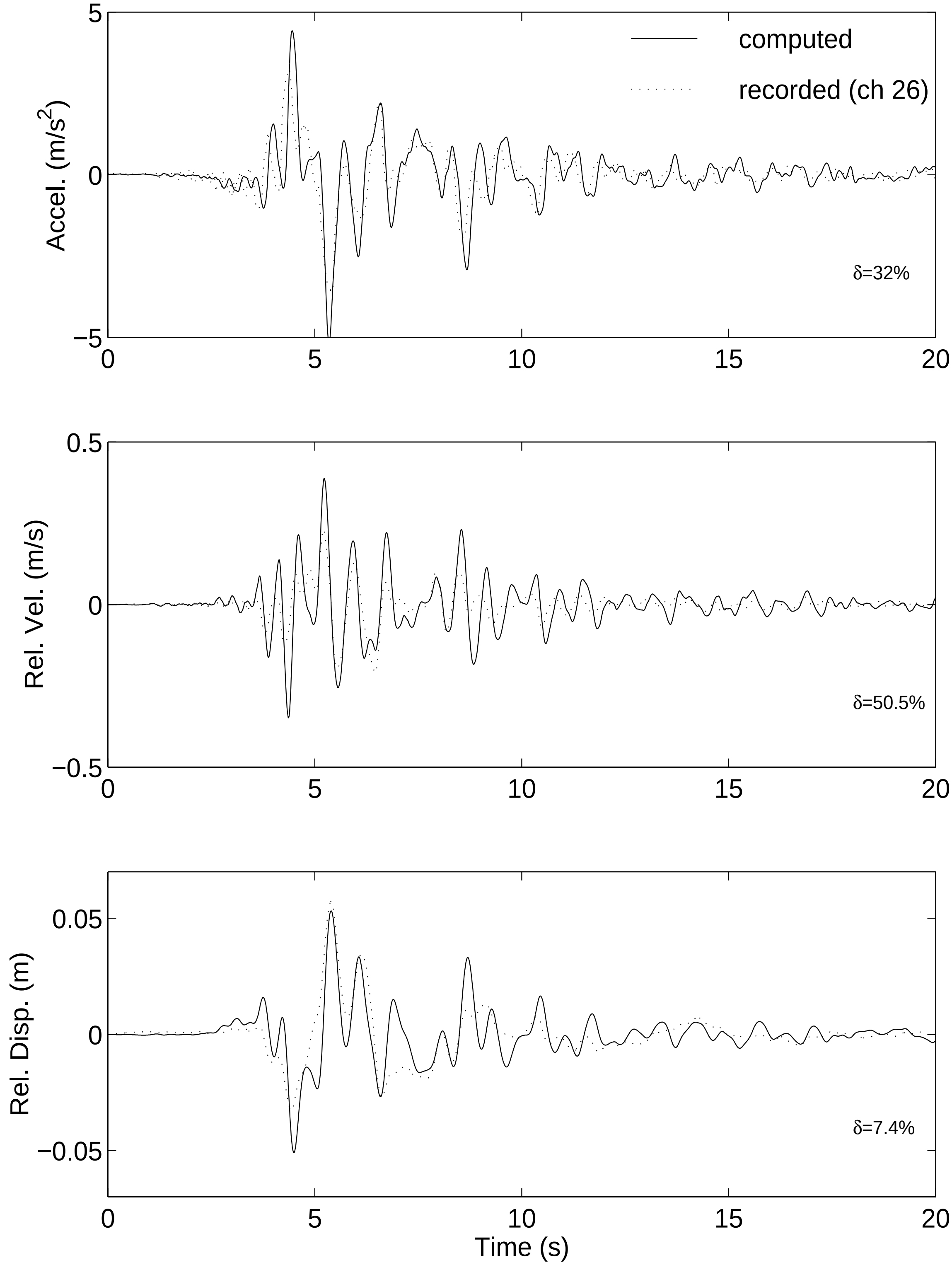

Figure 2.5. Crest total acceleration, relative velocity, and relative displacement time histories computed with shear-beam approximation for Meloland Road Overcrossing embankment ($G = 2.0MPa$, $\eta = 0.52$)

Figure 2.10. With $\rho_s = 1.6\ Mg/m^3$ and $V_s = 110\ m/s$, the small-strain shear modulus $G_{max} = \rho_s V_s^2 = 20\ MPa$. Following the averaged curve shown in Figure 2.4 and the aforementioned iterative procedure, our analysis converged at an approximate strain $\gamma = 6.7\times10^{-3}$, where $G/G_{max} = 0.1$ and $\eta = 0.52$.

When a shear wedge with the physical and geometrical characteristics of the embankment of the Painter Street Bridge is subjected to the input motion shown in Figure 2.14, our analysis converges at an approximate strain $\gamma = 4.8\times10^{-3}$, where $G/G_{max} = 0.125$ and $\eta = 0.50$.

2.2.2 Finite Element Analysis

The shear-wedge model presented in the previous section is a one-dimensional approximation of a three-dimensional structure. In this section the solution of the shear-wedge approximation is compared with the results of a 2-D and 3-D finite element analysis. The computer software ABAQUS (1997) is used in this study to conduct free- and forced- vibration dynamic analyses of the embankment. In the 2-D formulation isoparametric elements were used, whereas in the 3-D analysis eight node solid elements were used. In the 3-D model the approach slope along the longitudinal direction is included.

The response is computed in the time domain where damping is approximated with the Rayleigh approach. The damping matrix, $[C]$, of the soil structure is assumed to be a linear combination of the mass matrix, $[M]$, and the stiffness matrix, $[K]$

$$[C] = \alpha[M] + \beta[K] \tag{2.12}$$

in which α and β are frequency-independent coefficients. With this ad hoc approach the elements of the damping matrix, $[C]$, can be constructed by using the information on the modal damping of the soil structure at two distinct modes

$$\xi_j = \frac{\eta}{2} = \frac{1}{2}\left(\frac{\alpha}{\omega_j} + \beta\omega_j\right) \tag{2.13}$$

At every iteration where the new strain level is established and the values of G and η are updated, new values of the parameters α and β are established. In this analysis the values of α and β were computed by using the first and second modal frequencies ($j = 1\ and\ j = 2$).

Figure 2.6 plots the computed time histories of the converged strains at the base, mid-height and crest of the north embankment of the Meloland Road Overcrossing subjected to the

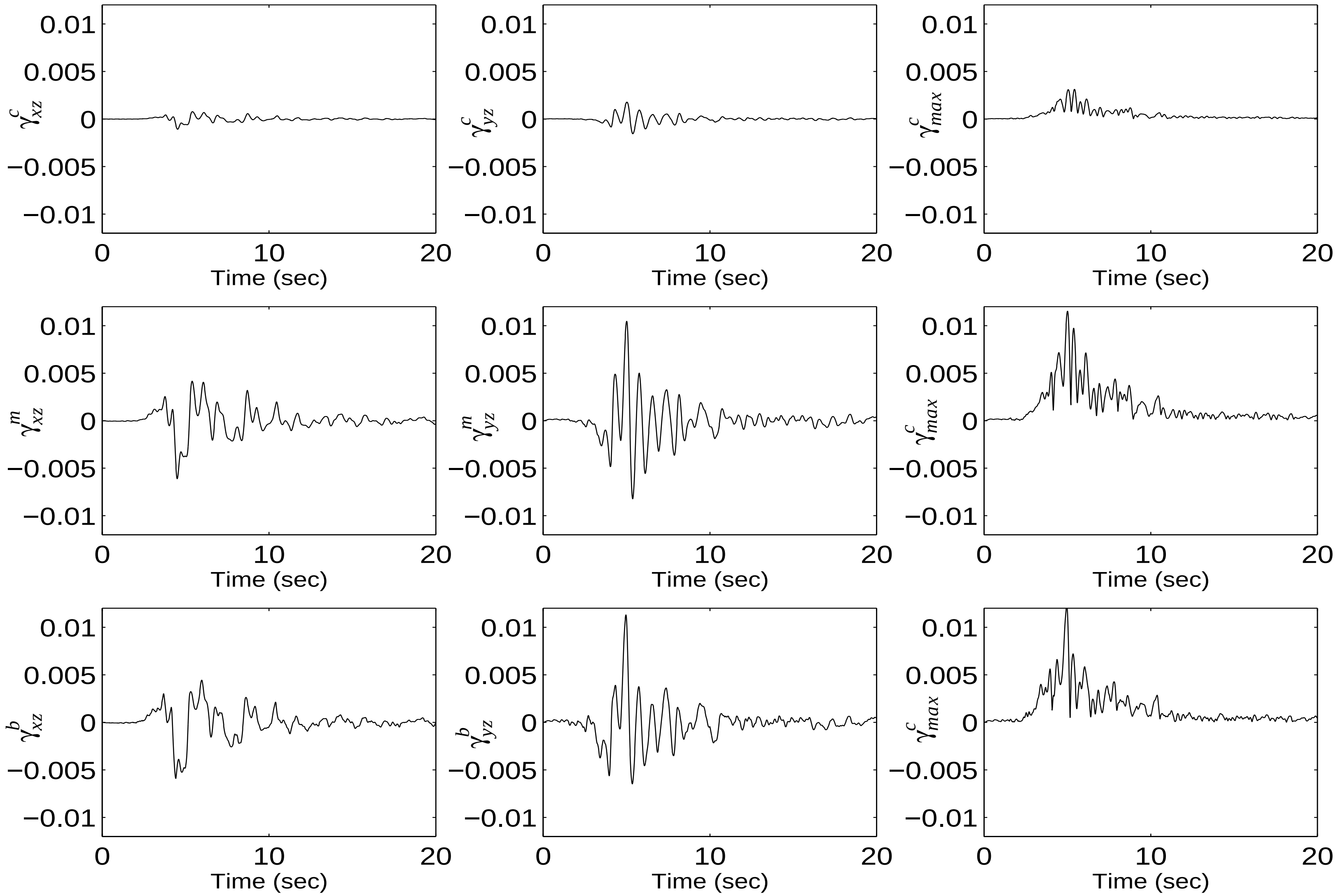

Figure 2.6. Strain time histories at base, center, and near top of Meloland Road Overcrossing soil embankment under 1979 Imperial Valley earthquake, computed with Rayleigh damping approximation ($G = 2.0MPa$, $\eta = 0.52$, $\alpha = 2.3057$, and $\beta = 2.9312\times10^{-2}$)

1979 Imperial Valley earthquake. The left column plots the time history of strains due to transverse shearing (γ_{xz}), the center column plots the time history of strains due to longitudinal shearing (γ_{yz}), whereas the right column plots the amplitude of the maximum shear strains as a function of time. Following the Seed and Idriss suggestion, Figure 2.6 indicates that an appropriate value for the converged strain is $\hat{\gamma} \approx 6.7 \times 10^{-3}$. This corresponds to $G = 2.0MPa$ ($G/G_{max} \approx 0.1$), and $\eta \approx 0.52$. These values are close to the values computed with the shear-wedge approximation.

Figure 2.7 plots the converged strain histories at the west embankment of the Painter Street Bridge subjected to the 1992 Petrolia earthquake. In this case the converged strain level is somehow smaller than the strain level shown in Figure 2.6, to a value of $\hat{\gamma} \approx 4.8 \times 10^{-3}$. The equivalent linear values for the stiffness and damping coefficient adopted are $G = 8.0MPa$ ($G/G_{max} \approx 0.125$), and $\eta = 0.50$.

Once the converged strains have been established they can be integrated in the time domain to yield the displacement profile of the embankment. In the special case of a harmonic steady-state excitation, $\ddot{u}_g = \ddot{u}_{go}e^{i\omega t}$, the software ABAQUS allows for a frequency domain evaluation of the response for any frequency dependence of the shear modulus and damping coefficient, including the noncausal compromise given by (2.8). With a frequency domain calculation of the response, one can directly compute the kinematic response function $I(\omega)$ using equation (2.5).

2.2.3 Kinematic Response Functions

Figure 2.8 (left) plots the kinematic response functions along the transverse direction (top) and longitudinal direction (bottom) of the north embankment of the Meloland Road Overcrossing computed with converged values of $G = 2.0MPa$ and $\eta = 0.52$. Figure 2.8 (right) plots the corresponding kinematic response functions of the west embankment of the Painter Street Bridge for converged value $G = 8.0MPa$ and $\eta = 0.5$. Along the transverse direction, results are obtained with the shear beam approximation (equation (2.5)) and a 2-D and 3-D finite element analysis. Along the longitudinal direction only a 3-D finite element analysis is meaningful. The results shown on Figure 2.8 (top) indicate that the shear-beam approximation captures most of the transverse response; whereas the responses computed by assuming a tapered or a prismatic geometry

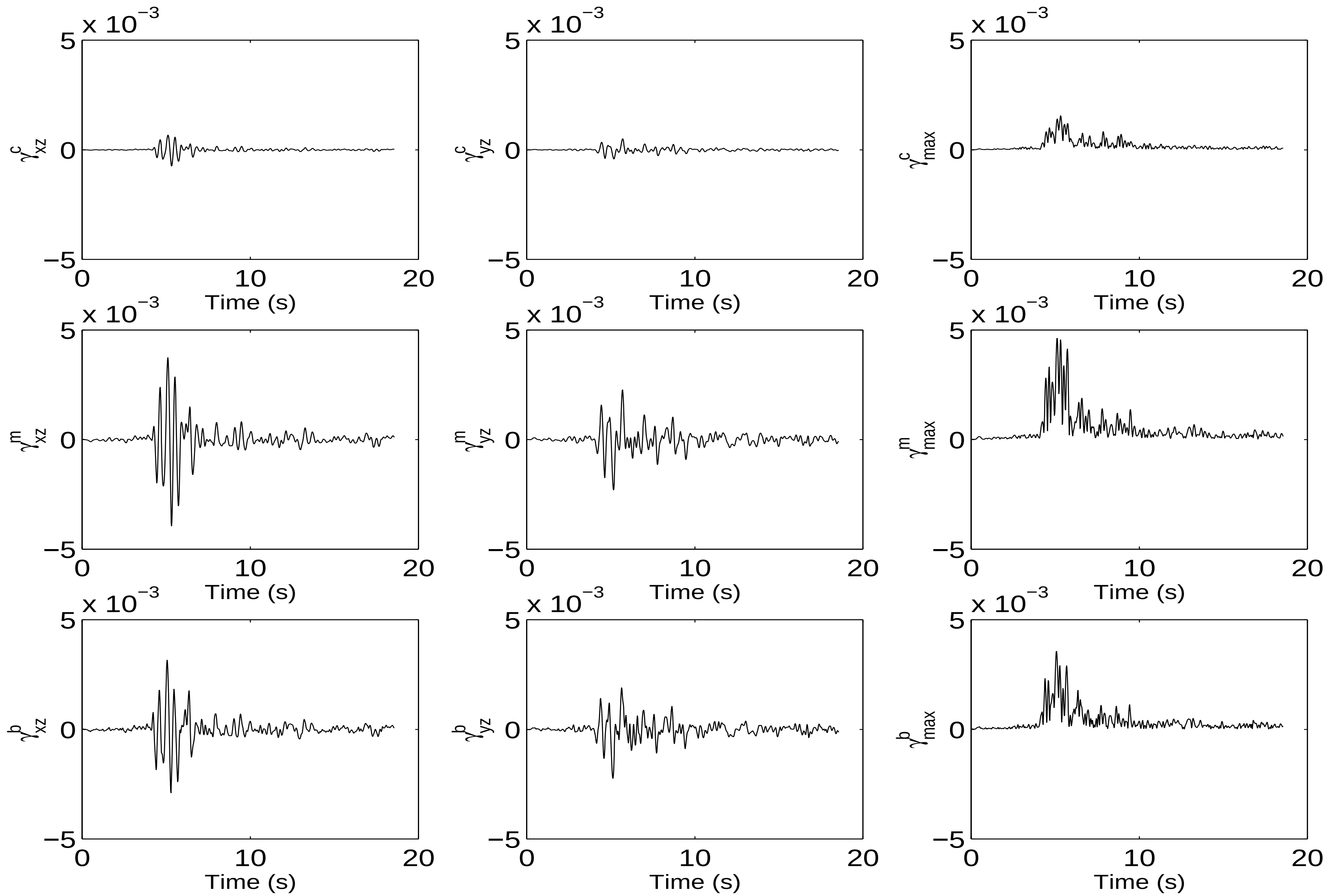

Figure 2.7. Strain time histories at base, center and near top of Painter Street Bridge soil embankment under 1992 Petrolia earthquake, computed with Rayleigh damping approximation ($G = 8.0MPa$, $\eta = 0.50$, $\alpha = 3.6461$, and $\beta = 1.7140\times10^{-2}$)

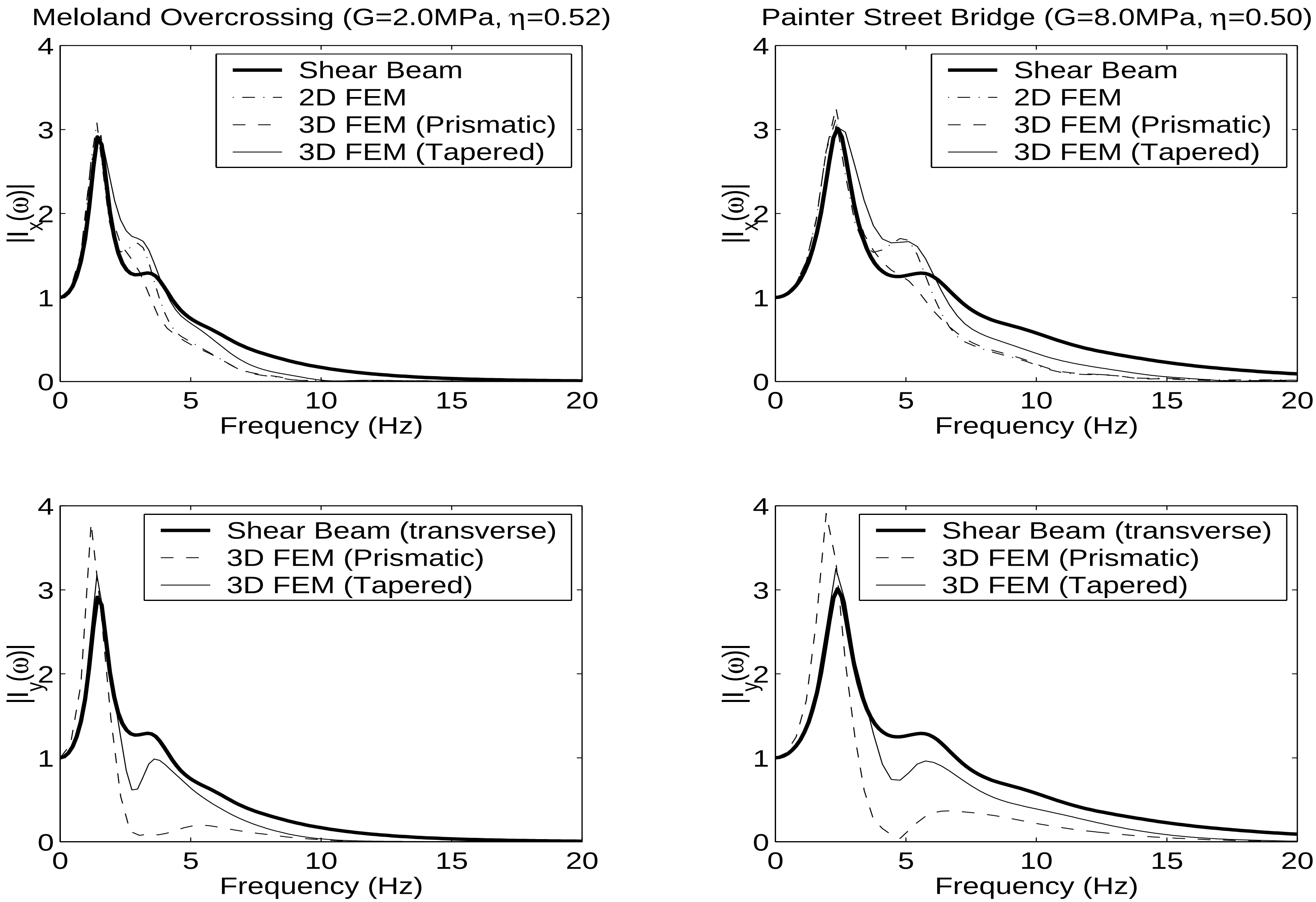

Figure 2.8. Kinematic response functions of Meloland Road Overcrossing embankment (left) and Painter Street Overcrossing embankment (right)

might differ appreciably only at higher frequencies of the longitudinal response. In the bottom plots of Figure 2.8 we included the kinematic response function along the transverse direction obtained with the shear-wedge approximation in order to show that it can capture most of the amplification generated due to a longitudinal excitation. This comparison is presented in order to validate the use of a single amplification function which can be easily derived from the shear-wedge model and can be applied for both transverse and longitudinal shaking.

2.2.4 Validation of Method — Crest Response

The kinematic response functions shown in Figure 2.8 can be used to compute the displacement time history at the crest of the embankment

$$u^c(t) = \frac{1}{2\pi}\int_{-\infty}^{\infty} I(\omega)u^b(\omega)e^{i\omega t}d\omega \qquad (2.14)$$

The validity of the equivalent linear approach expressed with equation (2.14) is established with motions recorded on the crests of bridge embankments that have been instrumented and subjected to strong shaking. In this study we use records from the Meloland Road Overcrossing and the Painter Street Bridge.

The Meloland Road Overcrossing, located near El Centro in southern California, is a concrete box-girder, two-span bridge with monolithic abutments and a single central column that was designed in 1968. The structure has two spans, each being 104 ft (31.7 m) long and 34 ft (10.36 m) wide. The single-column pier at the center of the bridge is approximately 20 ft (6.1 m) high and is supported by a pile group consisting 25 (5×5) driven concrete friction piles. The bridge has monolithic abutments supported by 7 concrete piles driven into stiff clay embankments overlaying native alluvium. The superstructure, abutments, embankments, and free field were instrumented with 26 strong-motion accelerometers (Werner et al. 1987). Figure 2.9 shows the elevation and plan views of the Meloland Road Overcrossing together with the location of the accelerometers. The bridge was strongly shaken by the October 15, 1979, Imperial Valley earthquake ($M_L = 6.4$) with a peak transverse acceleration of 0.51g recorded on the bridge deck. Figure 2.10 (left) shows the free-field motions recorded with channels 24 (EW), 15 (NS) and 14 (UP), while Figure 2.10 (center and right) shows the motions recorded on the north and south embankment respectively.

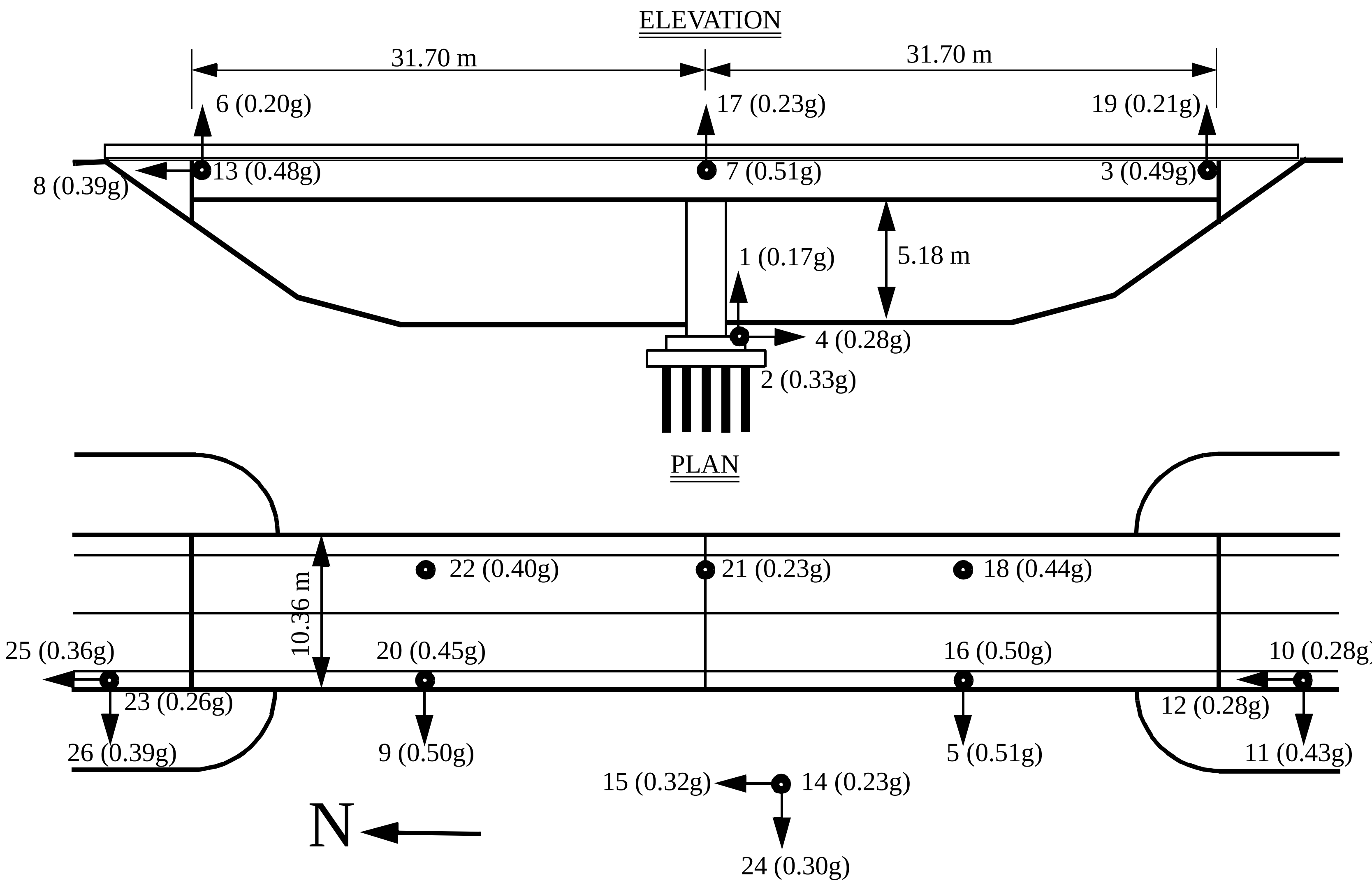

Figure 2.9. Elevation and plan views of Meloland Road Overcrossing along with locations of accelerometers

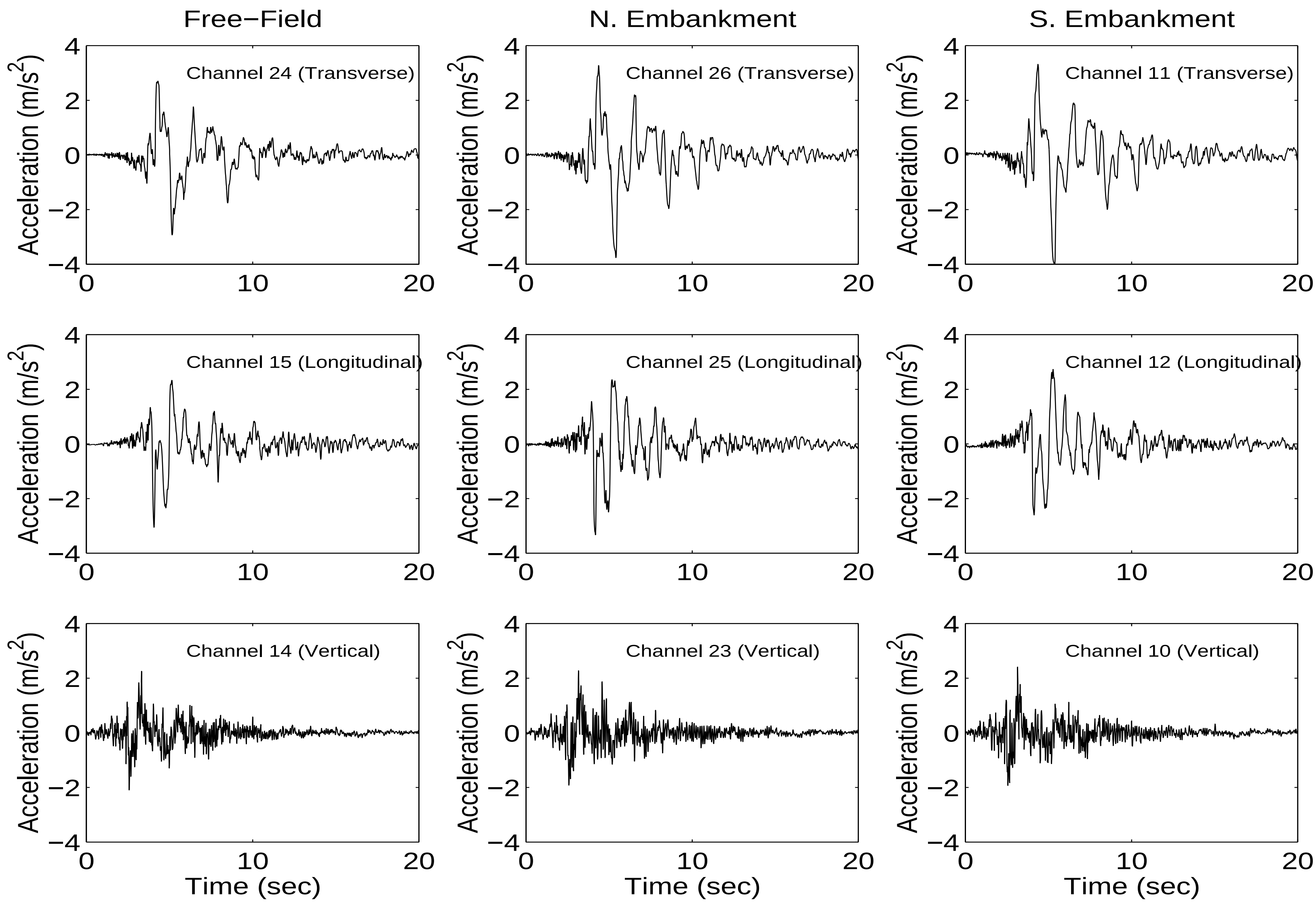

Figure 2.10. Recorded acceleration time histories at free field (left), north embankment (center) and south embankment (right) of Meloland Road Overcrossing during 1979 Imperial Valley earthquake.

Figure 2.11 (left column) plots the transverse crest response of the Meloland Road embankment when computed with equation (2.14) in which $I(\omega)$ is given by (2.5); whereas in the center and right columns, the values of $I(\omega)$ were computed with a 2-D and 3-D finite element analysis. In the 3-D finite element analysis the 4.4% approach slope of the MRO-embankment was used. The final values of shear modulus and the damping coefficient are $G = 2.0MPa$ and $\eta = 0.52$. These values correspond to an average macroscopic strain $\hat{\gamma} = 6.7\times10^{-3}$, as indicated in Figure 2.6. The relative difference, δ, between the maximum values of a computed and recorded response quantity, say v, is expressed as

$$\delta = 2\frac{|v^R|_{max} - |v^C|_{max}}{|v^R|_{max} + |v^C|_{max}} \tag{2.15}$$

where $|v^R|_{max}$ and $|v^C|_{max}$ are the maximum recorded and computed response quantities.

Figure 2.12 plots the longitudinal response of the Meloland Road embankment computed with equation (2.14) in which $I(\omega)$ is the corresponding kinematic response function under longitudinal vibrations, shown on the bottom-left of Figure 2.8. The left column plots the longitudinal response computed with (2.14) in which $I(\omega)$ is the kinematic response function obtained with the shear-wedge model in the transverse direction. The center column plots the longitudinal response computed with (2.14) in which $I(\omega)$ is the kinematic response function obtained with the prismatic geometry, while the right column plots the longitudinal response computed with $I(\omega)$ obtained with the tapered geometry.

The foregoing study shows that an equivalent linear analysis yields dependable results on the crest response of a non-skewed bridge embankment. Furthermore, the 1-D shear-beam approximation offers a realistic estimate for the transverse response of a mildly inclined embankment provided that the equivalent linear properties of the soil material are evaluated at realistic strains. Interestingly, the shear-beam approximation also provides an acceptable prediction of the longitudinal response. Our study proceeds with the validation of our method against the motions recorded on the skew embankments of the Painter Street Bridge.

The Painter Street Bridge, located near Rio Dell in northern California is a continuous, two-span, cast-in-place, prestressed post-tensioned, concrete, box-girder bridge that was instrumented in 1977 by the California Division of Mines and Geology. Several earthquakes from 1980 to 1987, ranging in magnitude from $4.4M_L$ to $6.9M_L$, have produced significant accelerograms,

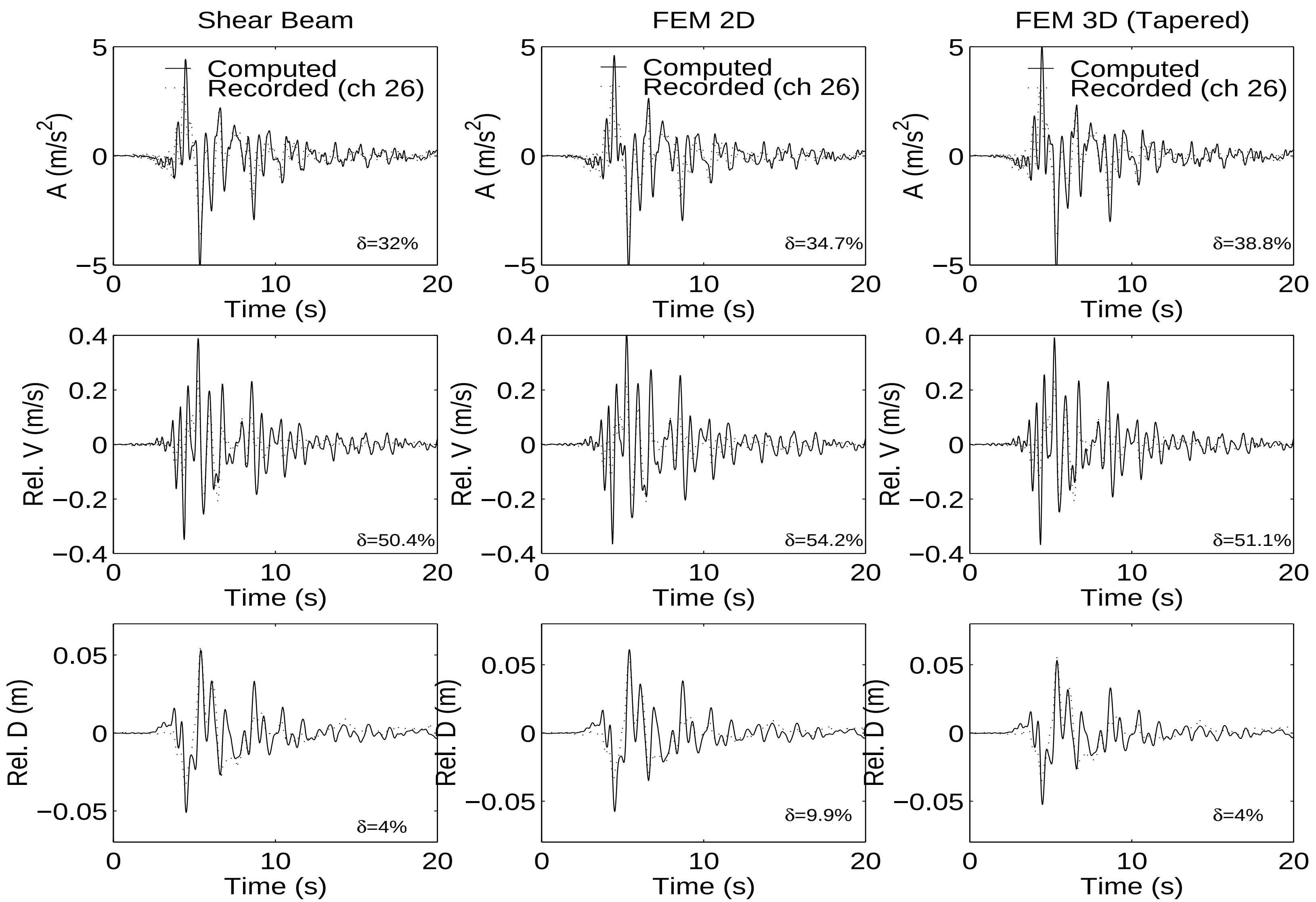

Figure 2.11. Transverse crest response of Meloland Road Overcrossing embankment computed with shear beam approximation (left), two-dimensional finite element method (center), and three-dimensional finite element method (right)

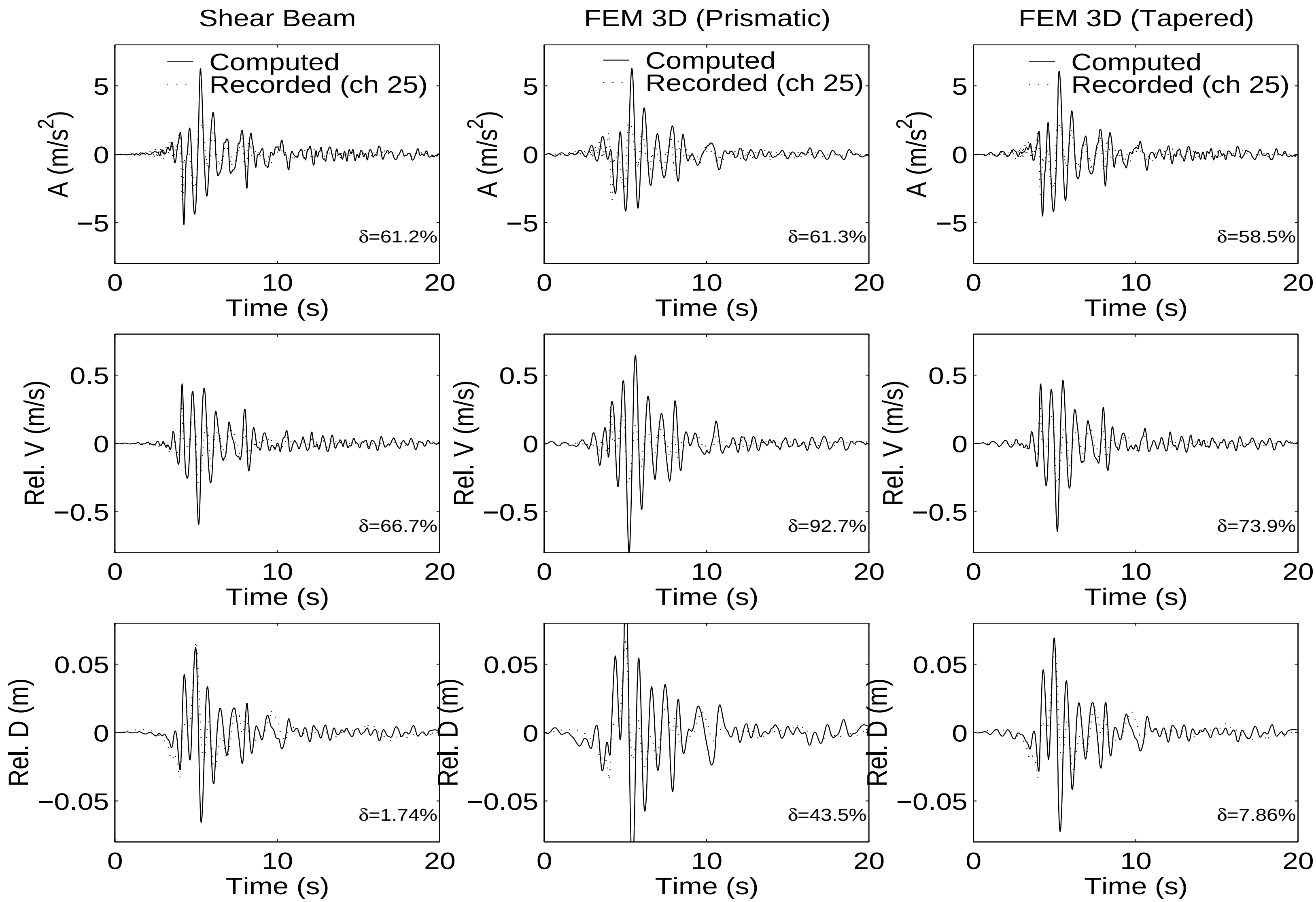

Figure 2.12. Longitudinal crest response of Meloland Road Overcrossing embankment computed with shear-beam approximation (left), three-dimensional prismatic geometry (center), and three-dimensional tapered geometry (right)

the peak values of which are summarized by Maroney et al. (1990). The largest peak acceleration of 0.59g was near the center of the bridge deck during a small ($M_L = 4.4$) nearby earthquake.

Maroney et al. (1990) used these records in conjunction with a number of finite element and lumped parameter (stick) models of the entire bridge. However, none of these models accounted for soil-foundation-superstructure interaction. At each abutment, soil-wall interaction was modeled using a single real-valued transverse spring, the stiffness of which was back-calculated from the interpreted small-amplitude fundamental natural period, $T \approx 0.3s$, in lateral vibration.

On April 25, 1992, the bridge was severely shaken by the Petrolia earthquake ($M_L = 7.1$, distance to the fault $R = 18km$) with a peak transverse acceleration of 0.92g recorded on the bridge deck. Figure 2.13 shows the elevation and plan views of the Painter Street Bridge together with the location of accelerometers. Motions were recorded in all accelerographs shown. Figure 2.14 (left) shows the free-field motions recorded with channel 14 (NS), 12 (EW) and 13 (UP), while Figure 2.14 (center and right) shows the motions recorded on the west and east embankment respectively.

Before construction, a geotechnical exploration at the locations of the piers was conducted. Using standard penetration test (SPT) measurements from the ground surface down to a depth of about 10 m, moderately stiff/dense soil layers were identified, which consisted of clayey sand, sandy silt, and gravelly sand. SPT blowcounts varied from 8 near the surface to 34 at 10 m depth. The underlying stratum was a very dense gravelly and silty sand, where blowcounts exceeded 100 blows/ft.

In a geophysical exploration by Heuze and Swift (1991) six so-called seismic refraction surveys were reported, along from lines parallel to the highway. Four different idealized soil profiles have emerged as shown in Figure 2.15. Evidently, the differences in the S-wave velocities and shear moduli among these profiles are substantial, given that they are 20-30 m apart from each other. For instance, the resulting low-strain shear modulus from the data along line 2 is 1.5 times the value of that resulting from the data along line 1. It is quite possible that some of these differences merely reflected inadequacies (general and specific) of the seismic refraction technique. The soil properties used for the dynamic analysis of embankments is taken as a set of uniform values, i.e., $\rho_s = 1.6Mg/m^3$, $V_s = 200\ m/s$, and $\nu = 0.4$ for both west and east embankments. The small-strain shear modulus is $G_{max} = \rho_s V_s^2 = 64MPa$.

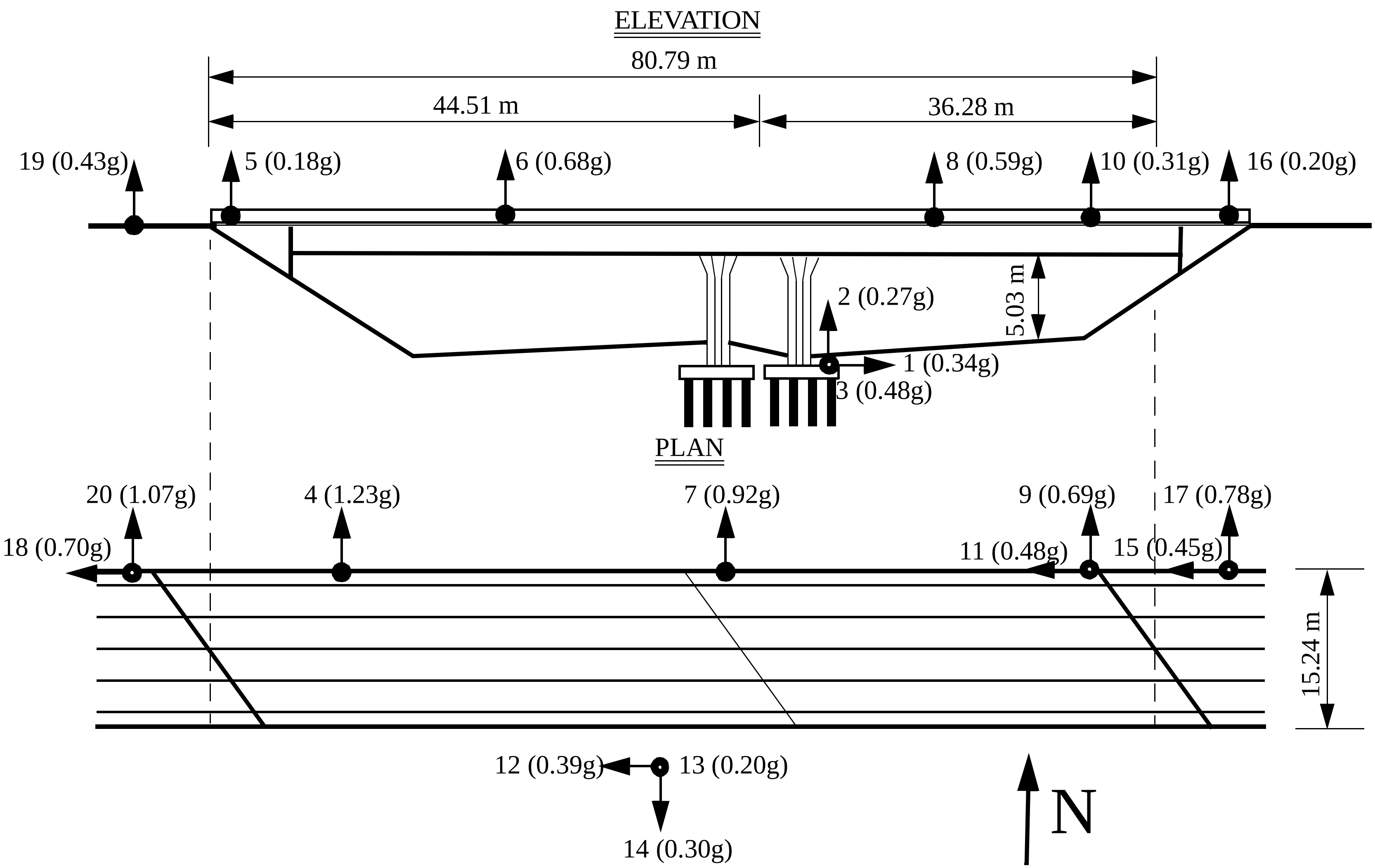

Figure 2.13. Elevation and plan views of Painter Street Overcrossing along with locations of accelerometers

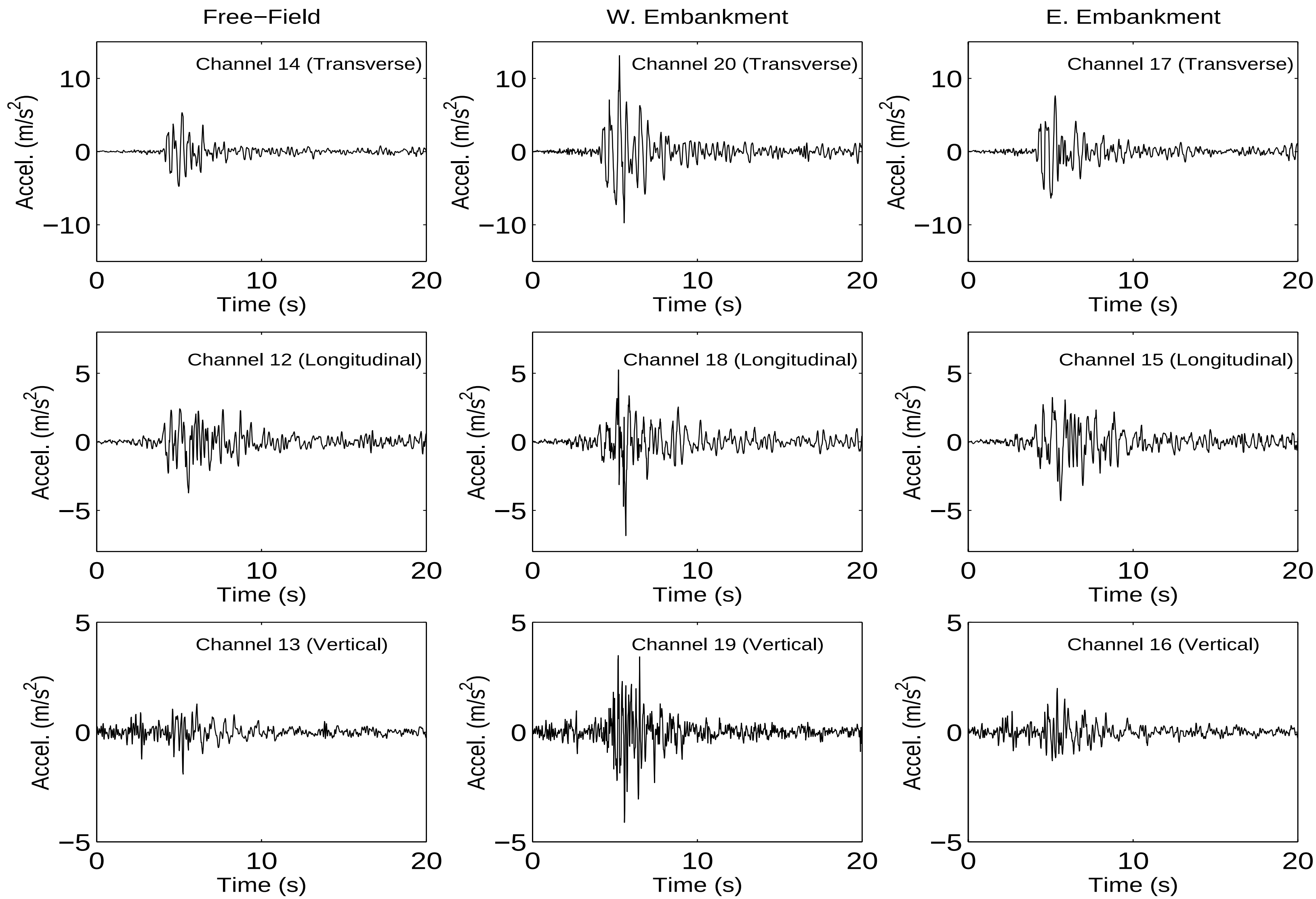

Figure 2.14. Recorded acceleration time histories at free field (left), west embankment (center), and east embankment (right) of Painter Street Overcrossing during 1992 Petrolia earthquake

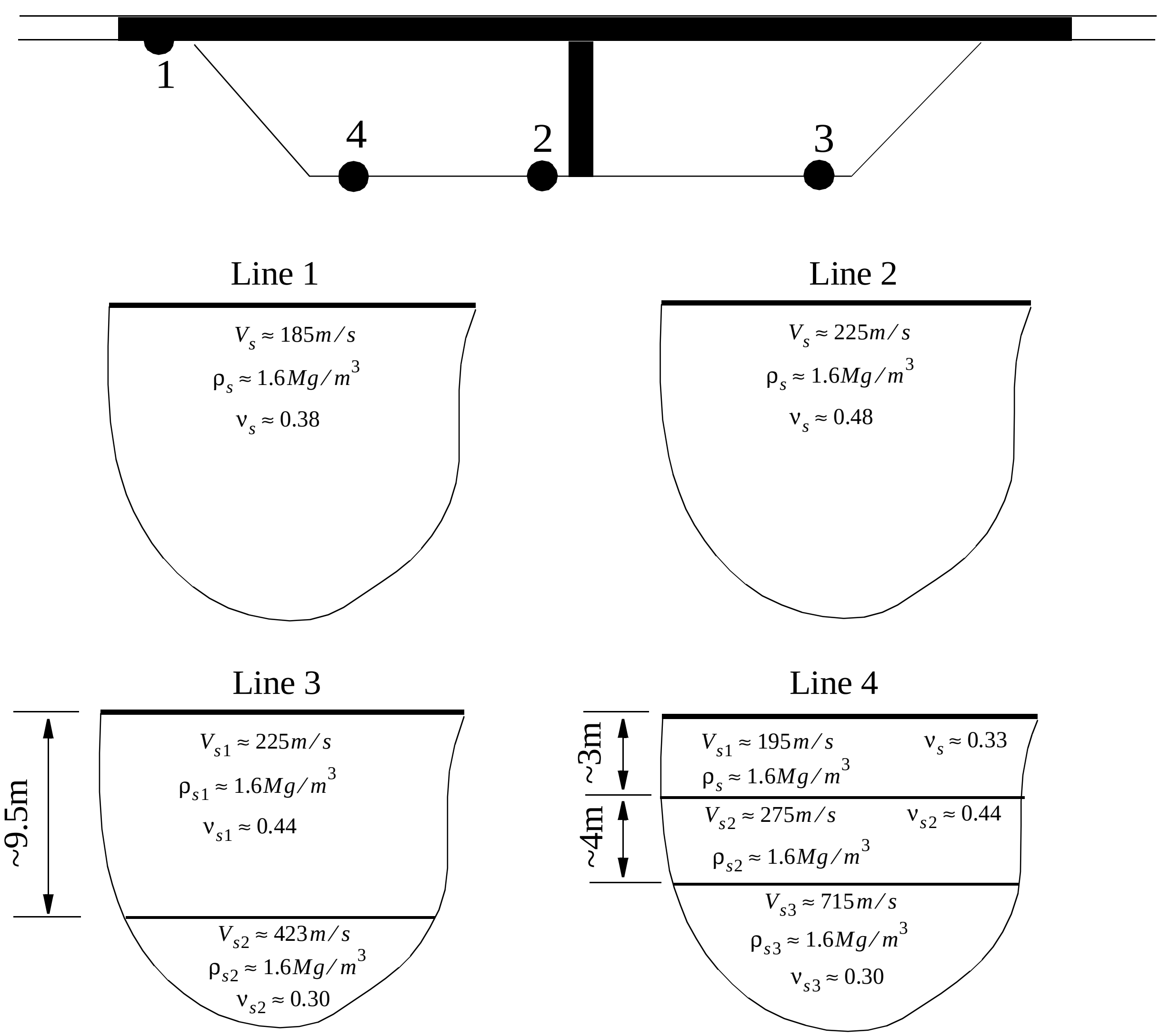

Figure 2.15. Idealized soil profiles that emerged from refraction surveys (Heuze and Swift 1991)

Figure 2.16 (left column) plots the transverse crest response of the west embankment at Painter Street Bridge when computed with equation (2.14) in which $I(\omega)$ is given by (2.5). In the center and right columns, the values of $I(\omega)$ used to compute the crest response were evaluated with 2-D and 3-D finite element analysis. In the 3-D finite element analysis the 5% approach slope of the Painter Street Bridge embankment is used. The converged values of the shear modulus and damping coefficient used are $G = 8.0MPa$ and $\eta = 0.50$ as indicated in Figure 2.7. Again, it is observed that the shear-beam approximation gives an acceptable estimate of the response provided that the equivalent linear soil properties are evaluated at a realistic strain level.

Figure 2.17 plots the longitudinal response of the west embankment of the Painter Street Bridge. The left column plots the computed longitudinal response using the kinematic response function, $I(\omega)$, obtained with shear-beam approximation in the transverse direction. The center column plots the computed response when the geometry of the embankment is assumed to be prismatic (zero approaching slope); whereas the right column plots the computed response when the tapered geometry is considered with a slope $i = 5\%$. The formulation that accounts for the tapered geometry of the embankment offers better predictions of the relative velocity and displacement histories than the formulation with prismatic geometry. At the same time, the shear-beam approximation gives equally good prediction of longitudinal response, compared to 3-D finite element analysis that accounts for the tapered geometry of the embankments.

The convincing results offered by the shear-beam approximation shown in both the Meloland Road Overcrossing and Painter Street Bridge cases indicate that the shear-beam approximation, despite its simplicity, is a dependable procedure for estimating the transverse and longitudinal response of bridge embankments.

2.2.5 Summary of Procedure to Compute the Kinematic Response Functions of Embankments

1. Compute the kinematic response functions with equation (2.5);

2. Compute the crest displacement response with equation (2.14);

3. Obtain the shear modulus, G, and damping coefficient, η through iterations so that the averaged strain, $\hat{\gamma} = \frac{2}{3}\frac{u^c_{x,\,max}}{H}$, converges.

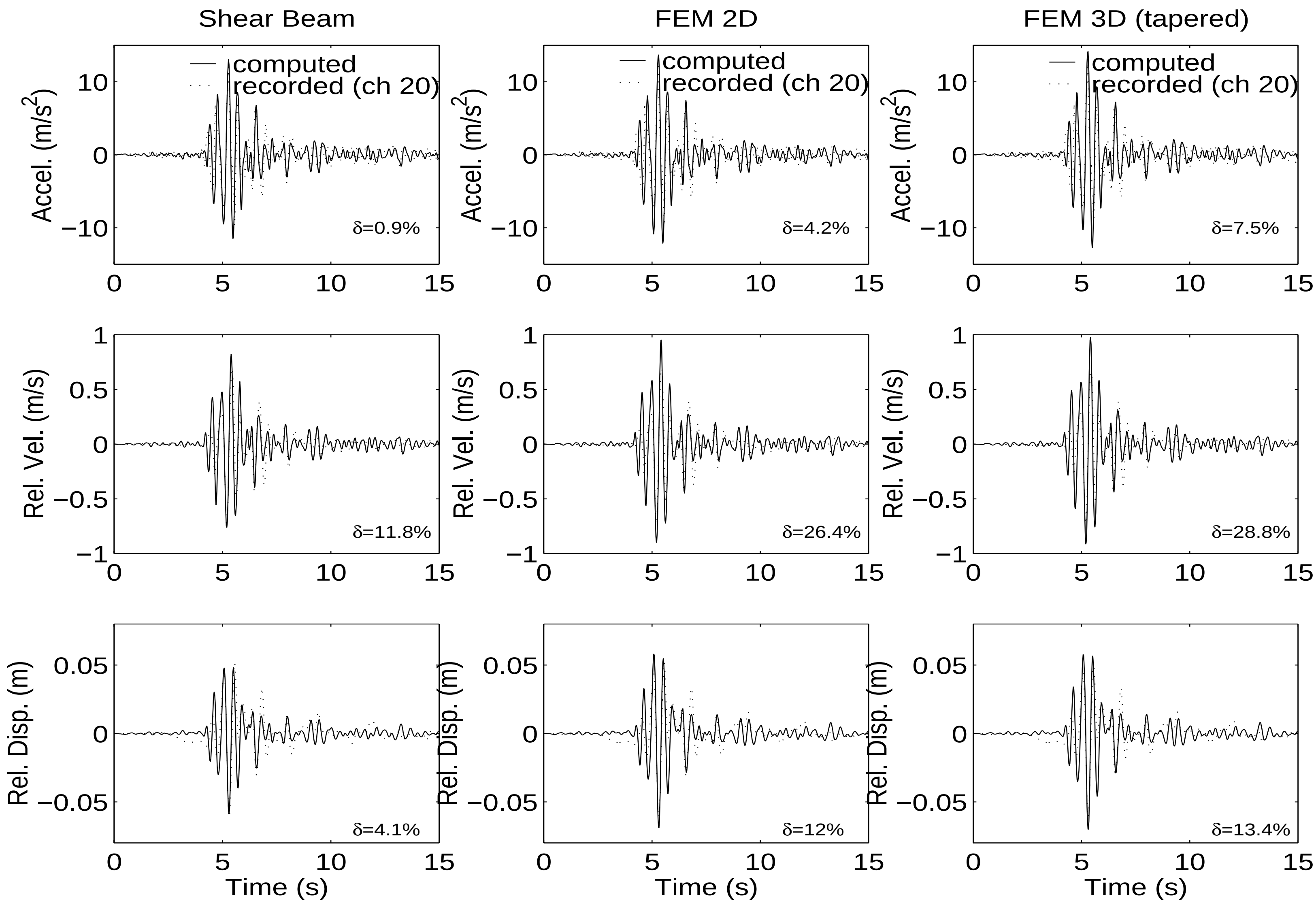

Figure 2.16. Transverse crest response of Painter Street Overcrossing embankment computed with shear-beam approximation (left), two-dimensional finite element method (center), and three-dimensional finite element method (right)

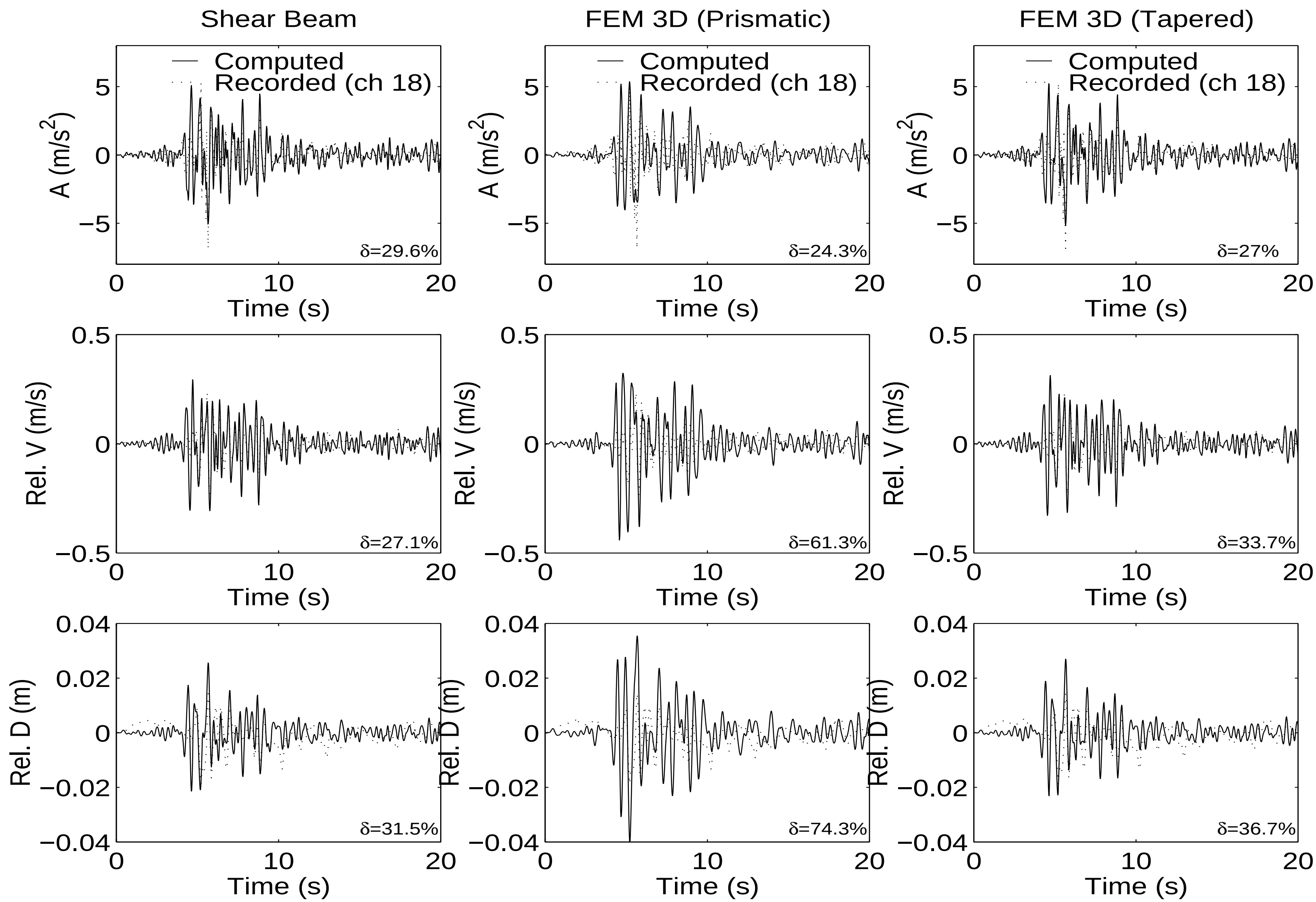

Figure 2.17. Longitudinal crest response of Painter Street Overcrossing embankment computed with shear-beam approximation (left), three-dimensional prismatic geometry (center), and three-dimensional tapered geometry (right)

2.3 DYNAMIC STIFFNESSES

2.3.1 Resilience of Abutments

The need to account for the resilience of abutments when subjected to the inertia forces of the deck has been recognized by several researchers who approached this problem in various ways. Maragakis (1985) proposed a Winkler foundation model to approximate the reaction of soil embankments on bridge abutments supported on spread footings. The spring values of the Winkler model were derived using soil mechanics concepts. Recently, his approach was extended by Siddharthan et al. (1993, 1997), who derived simple expressions for the values of the secant stiffnesses of abutments along the longitudinal, vertical, and transverse directions. Their simple expressions were found to agree with the experimental data from large-scale experiments conducted by Romstad et al. (1995). Crouse et al. (1987) conducted small-amplitude harmonic tests on the Horsethief Road Bridge and subsequently back-figured the values of distributed springs that approximated the interaction between abutment wall and backfill soil. The spring value that resulted from such small-amplitude tests is at the high end and is not practical for design under intense earthquake loading, since abutment stiffnesses are amplitude dependent. Motivated from the need to obtain more realistic values of abutment stiffnesses under strong ground motions, Goel and Chopra (1997) back-figured the force-displacement loops at the abutments of the Painter Street Bridge by investigating its recorded response under several earthquakes. Other studies have been conducted by Werner et al. (1994) and McCallen and Romstad (1994), who concluded that abutment stiffnesses are much lower and modal damping ratios much higher than previously deduced from low-amplitude tests. A large-scale experimental program was conducted by Romstad et al. (1995) to evaluate the stiffnesses and strengths of abutments. Table 2.1 summarizes various values of stiffnesses of bridge abutments that have been reported in the literature or that have been calculated with proposed methods. Table 2.1 includes the values used by Caltrans and the values that one computes using the closed-form expressions derived by Wilson and Tan (1990a). All stiffness values have been normalized by the width of the embankment with a unit of [Force]/[Length]^2. The large discrepancies shown in Table 2.1 is an indication of the lack of the dependable procedure in estimating the resilience of abutments.

Table 2.1: Comparisons of estimated abutment/embankment stiffnesses

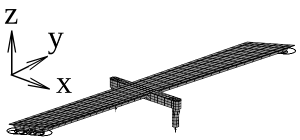		**Meloland Road Overcrossing** **H=7.92 m, B=10.36 m, S=1/2** $\rho = 1.6\ Mg/m^3$, $G_{max} = 16MPa$, $G = 2MPa$, $\eta = 0.52$			**Painter Street Bridge** **H=9.6 m, B=15.24 m, S=1/2** $\rho = 1.6\ Mg/m^3$, $G_{max} = 64MPa$, $G = 8MPa$, $\eta = 0.5$			**Large Scale Field Test** **H=2.06 m, B=4.72 m, S=1/2** $\rho = 1.8\ Mg/m^3$, $\nu = 0.4$, $G_{max} = 72MPa$		
Stiffnesses (MN/m^2**)**		k_x	k_y	k_z	k_x	k_y	k_z	k_x	k_y	k_z
1	Douglas et al. 1991	8.8	8.8	25.4	/	/	/	/	/	/
2	Maroney et al. 1993	/	/	/	/	/	/	2.6~7.4	3.7~11.1	/
3	McCallen & Romstad 1994	/	/	/	56.0	53.0	/	/	/	/
4	Werner 1994	10.3	/	/	/	/	/	/	/	/
5	Goel & Chopra 1997	/	/	/	9.6~14.0	9.6~46.9	/	/	/	/
6	Price and Eberhard 1998	/	/	/	4.7	/	/	/	/	/
7	Caltrans: Method A	58.6	57.5	/	53.2	57.5	/	44.6	57.5	/
8	Caltrans: Method B	7.4	/	/	6.9	/	/	2.6~3.4	/	/
9	Wilson 1988	12.1	12.1	16.1	24.6	24.9	52.5	/	/	/
10	Wilson & Tan 1990a	3.3	/	9.2	13.2	/	37	/	/	/
11	Siddharthan et al 1997	10~48	0.3~1.5	12~54	27~126	0.7~3.4	21.6~101.3	1.5~6.8	0.1~0.4	1.1~4.9
12	FEM 3D	2~3	2~3.1	7.5	9~14	9~13.8	38.2	/	/	/
13	Proposed Simple Procedure	2	2	/	10	10	/	/	/	/
Note	1. Values are identified from records, pile foundation stiffnesses are included. 2. Experimental results, pile foundation stiffnesses are included. 3. Per Caltrans procedure A, pile foundation stiffnesses are not included. 4. Best identified value, including pile foundation stiffnesses. 5. Back-figured values, including pile foundation stiffnesses. 6. Pile foundation stiffnesses are not included. 7. Use (200kips/in/ft)*(2/3 wingwall length)*4/3 in transverse direction and (200kips/in/ft)*(0.5*embankment width) in longitudinal direction. 8. Use 7.7ksf*(effective wingwall area)/0.2 ft. 9. Use converged shear modulus and damping coefficient without including pile foundation stiffnesses. 10. Same as 9. 11. Unable to reproduce the results in longitudinal direction with the formulations presented in their paper. Pile foundation stiffnesses are not included. 12. Same as 9. 13. Use unit-width shear-wedge solution multiplied by critical length, L_c. Pile foundation stiffnesses are not included.									

2.3.2 The Shear Beam Approximation

The Wilson and Tan expressions, given by equations (2.16) and (2.17) of this report, were derived by integrating the incremental displacements of a slice of unit width of the wedge due to a distributed load at the crest.

$$\hat{k}_x(0) = \frac{2G}{S\ln\left(1 + \frac{2H}{SB_c}\right)} \tag{2.16}$$

$$\hat{k}_z(0) = \frac{2E}{S\ln\left(1 + \frac{2H}{SB_c}\right)} \tag{2.17}$$

where G is the converged value of the shear modulus that is concluded from the kinematic response analysis and $E = 2(1 + \nu)G$ is the associated Young's modulus. The expressions given by (2.16) and (2.17) assume that the ground beneath the embankment is rigid and does not undergo any deformation; whereas its geometry is symmetric, having the same slope on each side. For the general case of a nonsymmetric cross section (see Figure 2.1(top)), the transverse displacement at the top of unit-width wedge due to a distributed load, p_x, at the crest is given by

$$u_x = \int_{z_0}^{z_0+H} \gamma dz = \int_{z_0}^{z_0+H} \frac{p_x}{G} \cdot \frac{z_0}{zB_c} dz = \frac{p_x z_0}{GB_c} \ln\left(\frac{z_0 + H}{z_0}\right). \tag{2.18}$$

and the transverse static stiffness of the unit-width wedge is thus given by

$$\hat{k}_x(0) = \frac{p_x}{u_x} = \frac{GB_c}{z_0 \ln\left(\frac{z_0 + H}{z_0}\right)}. \tag{2.19}$$

Similarly, the vertical static stiffness due to a distributed load at the crest is given by

$$\hat{k}_z(0) = \frac{p_z}{u_z} = \frac{EB_c}{z_0 \ln\left(\frac{z_0 + H}{z_0}\right)}. \tag{2.20}$$

For the case of a symmetric embankment equations (2.19) and (2.20) reduce to equations (2.16) and (2.17), since $z_0 = \frac{1}{2} B_c S$.

The static solutions derived by Wilson and Tan (1990a) for the case of a symmetric embankment or the more general expressions offered by equations (2.19) can be extended for harmonic distributed loads at the crest. With reference to Figure 2.18 (top), considering a distributed

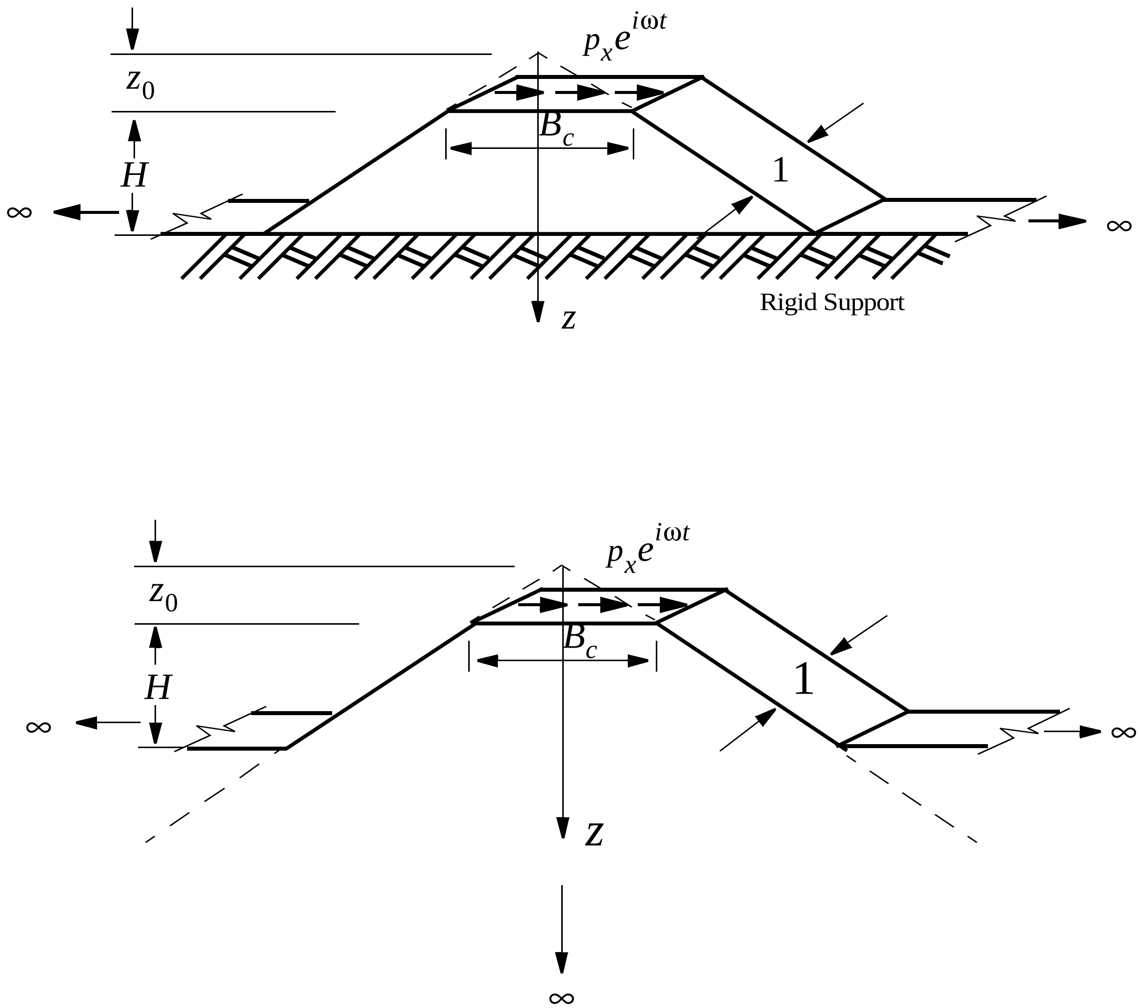

Flexible Support — Infinite Wedge

Figure 2.18. Unit-width finite wedge (top) and infinitely tall wedge (bottom)

harmonic loading, $p_x e^{i\omega t}$, that creates horizontal crest displacement, $u_x e^{i(\omega t - \varphi)}$, dynamic equilibrium of a section, dz, of the wedge gives

$$\frac{\partial}{\partial z}Q(z, t) = \rho A(z)\frac{\partial^2}{\partial t^2}u_x(z, t) \tag{2.21}$$

where $Q(z, t)$ is the time-dependent shear force at depth z. Using that

$$\frac{Q(z,t)}{A(z)} = \tau(z) = G\gamma(z) = G\frac{\partial}{\partial z}u_x(z,t) \tag{2.22}$$

equation (2.21) becomes

$$\frac{\partial^2}{\partial z^2}u_x(z,t) + \frac{1}{z}\frac{\partial}{\partial z}u_x(z,t) = \frac{1}{V_s^2}\frac{\partial^2}{\partial t^2}u_x(z,t) \tag{2.23}$$

The solution of equation (2.23) is offered below for limiting cases where (a) the supporting soil is rigid and does not accommodate any deformation and (b) the supporting soil is deformable to the extent that the embankment wedge can be extended into the halfspace over a large depth. The boundary conditions for case (a) are that the displacements at depth $z = z_0 + H$ are zero, while the shear force at the crest is equal to the external load, i.e., $Q(z_0, t) = p_x e^{i\omega t}$. The boundary condition for the case (b) is that there are no incoming waves (Somerfield radiation condition — see Wolf (1994) among others), while the shear force $Q(z_0, t) = p_x e^{i\omega t}$. With these boundary conditions the solution of (2.23) for case (a) is

$$u_x(z,t) = \frac{1}{GB_c k}\cdot\frac{Y_0[k(z_0+H)]J_0(kz) - J_0[k(z_0+H)]Y_0(kz)}{J_1(kz_0)Y_0[k(z_0+H)] - J_0[k(z_0+H)]Y_1(kz_0)}p_x e^{i\omega t} \quad \text{(rigid supporting soil)} \tag{2.24}$$

and for case (b) is

$$u_x(z,t) = \frac{1}{GB_c k}\cdot\frac{H_0^{(2)}(kz)}{H_1^{(2)}(kz_0)}p_x e^{i\omega t} \quad \text{(infinitely tall wedge)} \tag{2.25}$$

At the crest of the embankment

$$p_x(z_0, t) = \hat{k}_x(\omega)u_x(z_0, t) \tag{2.26}$$

and for each of these cases (a) and (b) equation (2.26) gives

$$\hat{k}_x(\omega) = G(1+i\eta)B_c k\cdot\frac{J_1(kz_0)Y_0[k(z_0+H)] - J_0[k(z_0+H)]Y_1(kz_0)}{Y_0[k(z_0+H)]J_0(kz_0) - J_0[k(z_0+H)]Y_0(kz_0)} \quad \text{(rigid supporting soil)} \tag{2.27}$$

and

$$\hat{k}_x(\omega) = G(1+i\eta)B_c k\frac{H_1^{(2)}(kz_0)}{H_0^{(2)}(kz_0)} \quad \text{(infinitely tall wedge)} \tag{2.28}$$

Figures 2.19 and 2.20 plot the real and imaginary parts of the dynamic stiffnesses given by equation (2.27) (left, rigid support) and equation (2.28) (right, infinitely tall wedge). In Figure 2.19 the material and geometrical properties, $G = 2MPa$, $\eta = 0.52$, $z_0 = 2.59m$, $H = 7.92m$, and $B_c = 10.36m$ of the Meloland Road Overcrossing are used; whereas in Figure 2.20 the material and geometrical properties, $G = 8MPa$, $\eta = 0.5$, $z_0 = 3.81m$, $H = 9.6m$, and $B_c = 15.24m$ of the Painter Street Bridge are used.

2.3.3 Finite Element Analysis

The ability of the shear-wedge model to approximate the transverse dynamic stiffness of an approach embankment is examined in this section by conducting finite element analysis on a unit-width wedge. Figures 2.19 and 2.20 show finite element solutions for the transverse dynamic stiffness of the unit-width wedge. In the case of the infinitely tall wedge (flexible support), the supporting soil is represented by the 2-D infinite element with the soil properties same as that of the embankments. The solution is computed by imposing a transverse oscillating load, $p_x e^{i\omega t}$ at the crest of the wedge and computing the resulting displacement, $u_x e^{i(\omega t - \phi)}$. By definition, the dynamic stiffness is

$$\hat{k}_x(\omega) = k_{1x}(\omega) + ik_{2x}(\omega) = \frac{p_x e^{i\omega t}}{u_x e^{i(\omega t - \phi)}} = \frac{p_x}{u_x}e^{i\phi} \tag{2.29}$$

The dashed lines in Figures 2.19 and 2.20 are the results from a 2-D finite element analysis; whereas the chain line in these figures is the finite element solution that is obtained by restraining the vertical degree of freedom. The real part of solutions given by (2.27) at static limit agrees with the solution of Wilson and Tan (1990a), while the solutions from 2-D finite element analysis follow the similar trend with the analytical solution but with slightly lower values. Because of the unit-width of the wedge, the units of equation (2.29) are [Force]/[length]^2. To translate the results of equations (2.27) to (2.29) to spring values that reflect the dynamic stiffness of the entire embankment, one has to multiply the computed values with a critical length L_c. Wil-

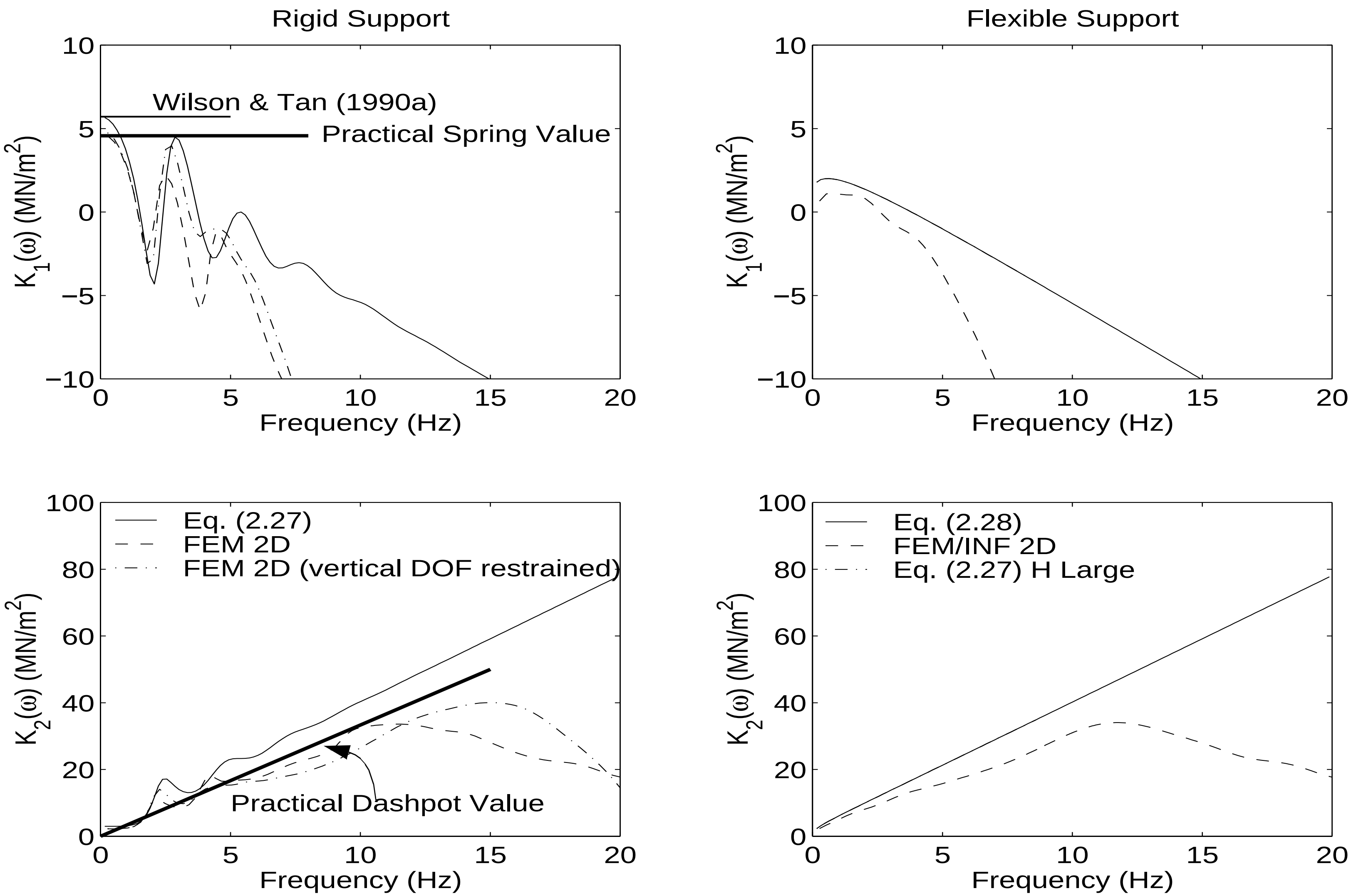

Figure 2.19. Transverse dynamic stiffnesses of shear-wedge model and solution of two-dimensional finite element formulation. Left: finite wedge on rigid support; Right: infinitely tall wedge. Material and geometrical properties are those of Meloland Road Overcrossing ($G = 2MPa$, $\eta = 0.52$, $z_0 = 2.59m$, $H = 7.92m$, and $B_c = 10.36m$).

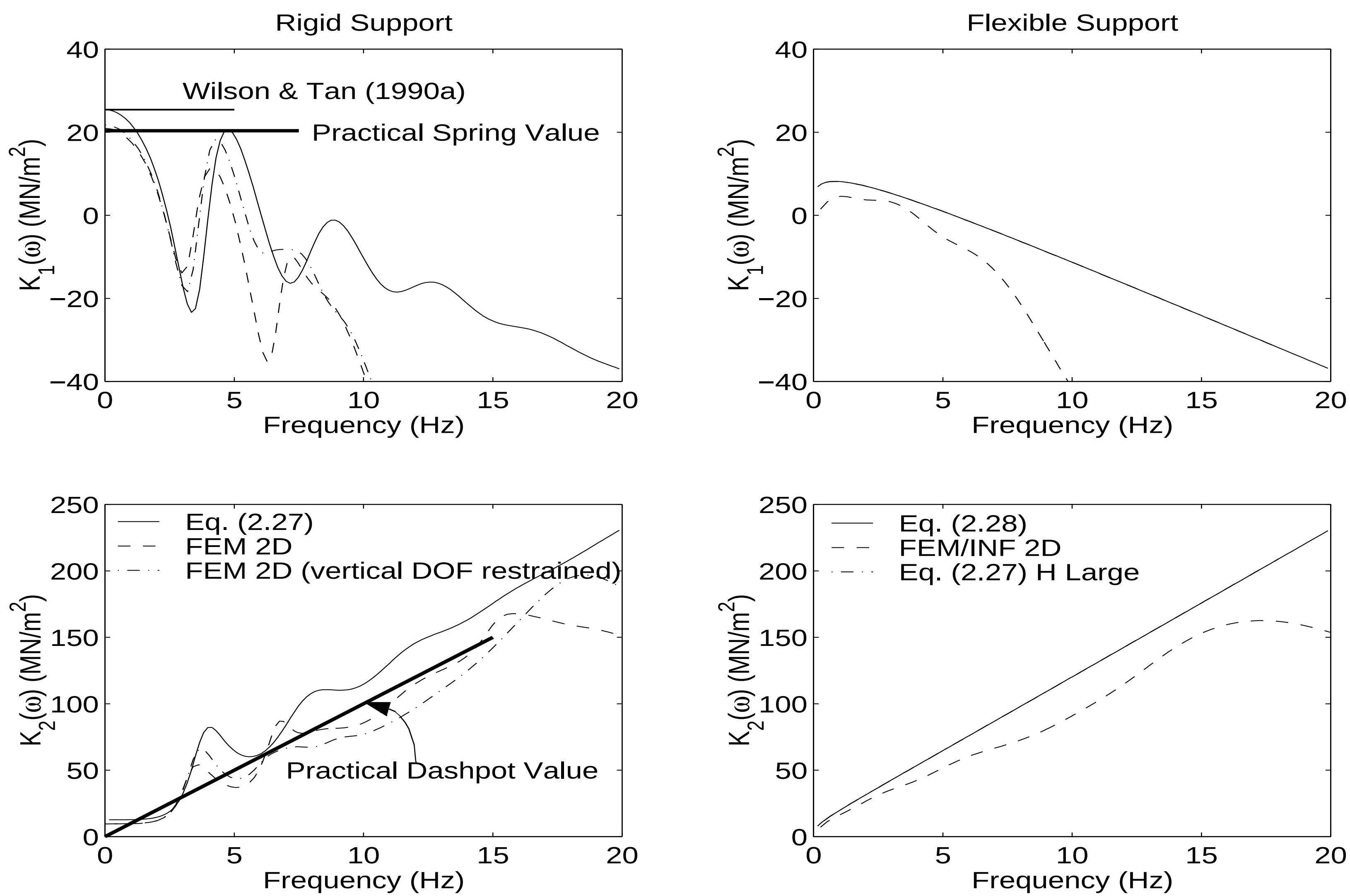

Figure 2.20. Transverse dynamic stiffnesses of shear-wedge model and solution of two-dimensional finite element formulation. Left: finite wedge on rigid support; Right: infinitely tall wedge. Material and geometrical properties are those of Painter Street Overcrossing ($G = 8MPa$, $\eta = 0.5$, $z_0 = 3.81m$, $H = 9.6m$, and $B_c = 15.24m$).

son and Tan (1990b) proposed to use as critical length the length of the wing wall. Herein a 3-D finite element study is conducted to further investigate this issue.

Figure 2.21 shows an isoparametric schematic of an approach embankment subjected to transverse (top) and longitudinal (bottom) oscillatory loads, $p_x e^{i\omega t}$ and $p_y e^{i\omega t}$. Under harmonic loading along direction j $(j \in (x, y))$, the resulting displacement is harmonic, $u_j e^{i(\omega t - \phi)}$, where ϕ is the phase difference between displacement and force. Along any direction, j, the dynamic stiffness is defined as

$$\tilde{k}_j(\omega) = k_{1j}(\omega) + ik_{2j}(\omega) = \frac{p_j e^{i\omega t}}{u_j e^{i(\omega t - \phi)}} = \frac{p_j}{u_j} e^{i\phi} \tag{2.30}$$

The ratio p_j/u_j is a real and frequency-dependent quantity known as the total distributed stiffness, $k_{0j} = p_j/u_j$, whereas $k_{1j}(\omega) = p_j/u_j \cos(\phi)$ is the distributed storage stiffness and $k_{2j}(\omega) = p_j/u_j \sin(\phi)$ is the distributed loss stiffness.

The computer software ABAQUS (1997) is used to conduct the forced-vibration dynamic analysis of bridge embankments under the loadings shown in Figure 2.21. Figure 2.22 plots the computed real part (storage stiffness) and the imaginary part (loss stiffness) of the Meloland Road Overcrossing embankments under transverse, longitudinal, and vertical distributed loadings. The values of G and η of embankment soil used in the elastic analysis are the converged values of $G = 2.0MPa$ and $\eta = 0.52$ that were determined from the forced vibration of the embankment under base shaking. The shear modulus of supporting soil underneath the embankment is taken as $G_s/G = \infty$, 10 and 1, respectively. Figure 2.22 indicates that the effect of the stiffness of the supporting soil is marginal in both the transverse and longitudinal directions; therefore the solution of the embankment sitting on a rigid support can be used with confidence. Similarly, Figure 2.23 plots the computed real and imaginary parts of Painter Street Bridge embankments under transverse, longitudinal, and vertical loadings. The values of G and η of embankment soil used in the elastic analysis are the converged values $G = 8.0MPa$ and $\eta = 0.5$, also determined from the forced vibration of the embankment under the corresponding base shaking. The slope of the loss stiffness gives the dashpot values. The spring and dashpot value, as shown in Figure 1.1, can be extracted by multiplying the values shown in figures 2.22 and 2.23 with the width of the embankment, B_c.

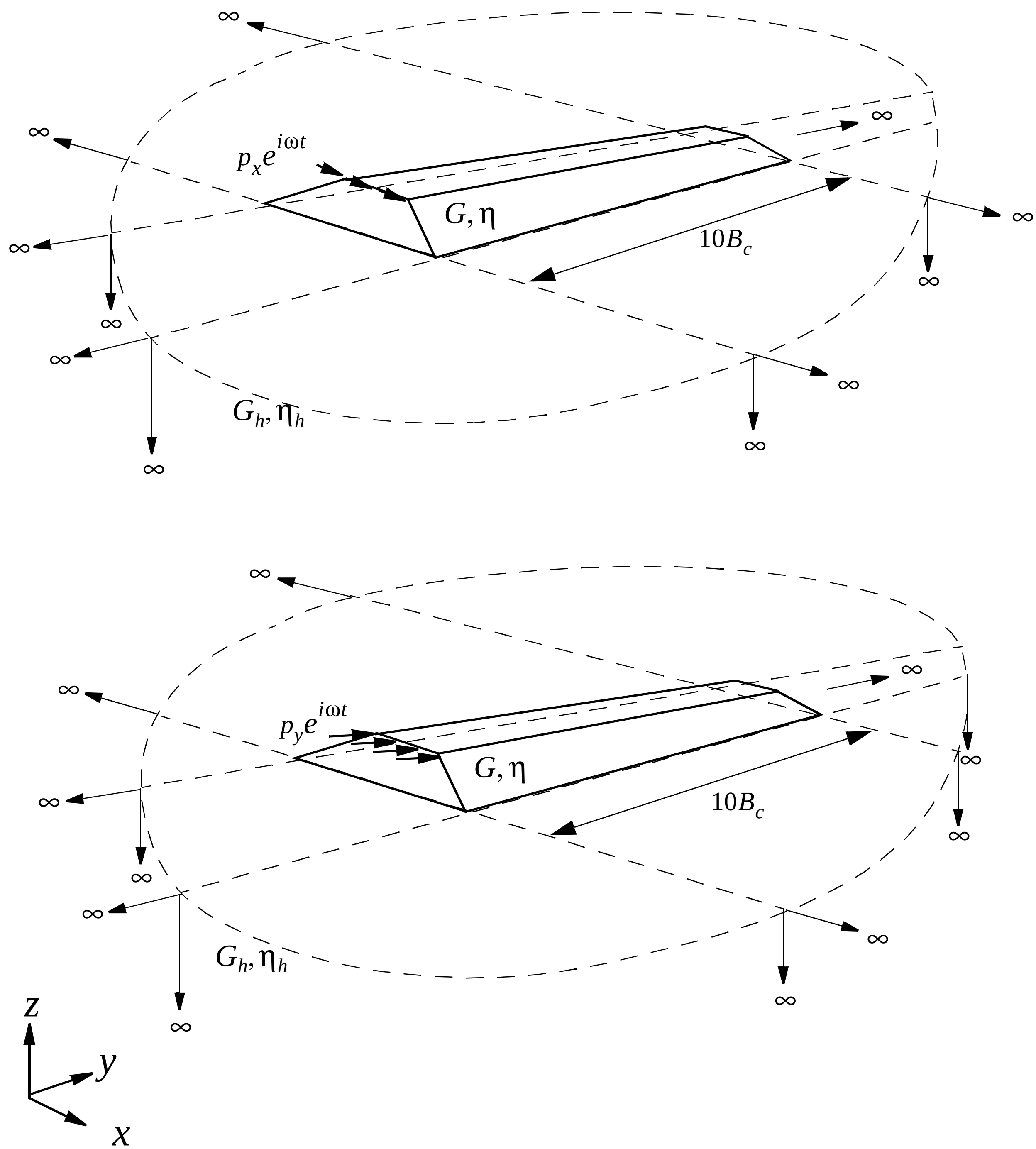

Figure 2.21. Transverse and longitudinal loading imposed to obtain dynamic stiffnesses of approach embankment with material properties, G and η, supported on halfspace with material properties, G_h and η_h

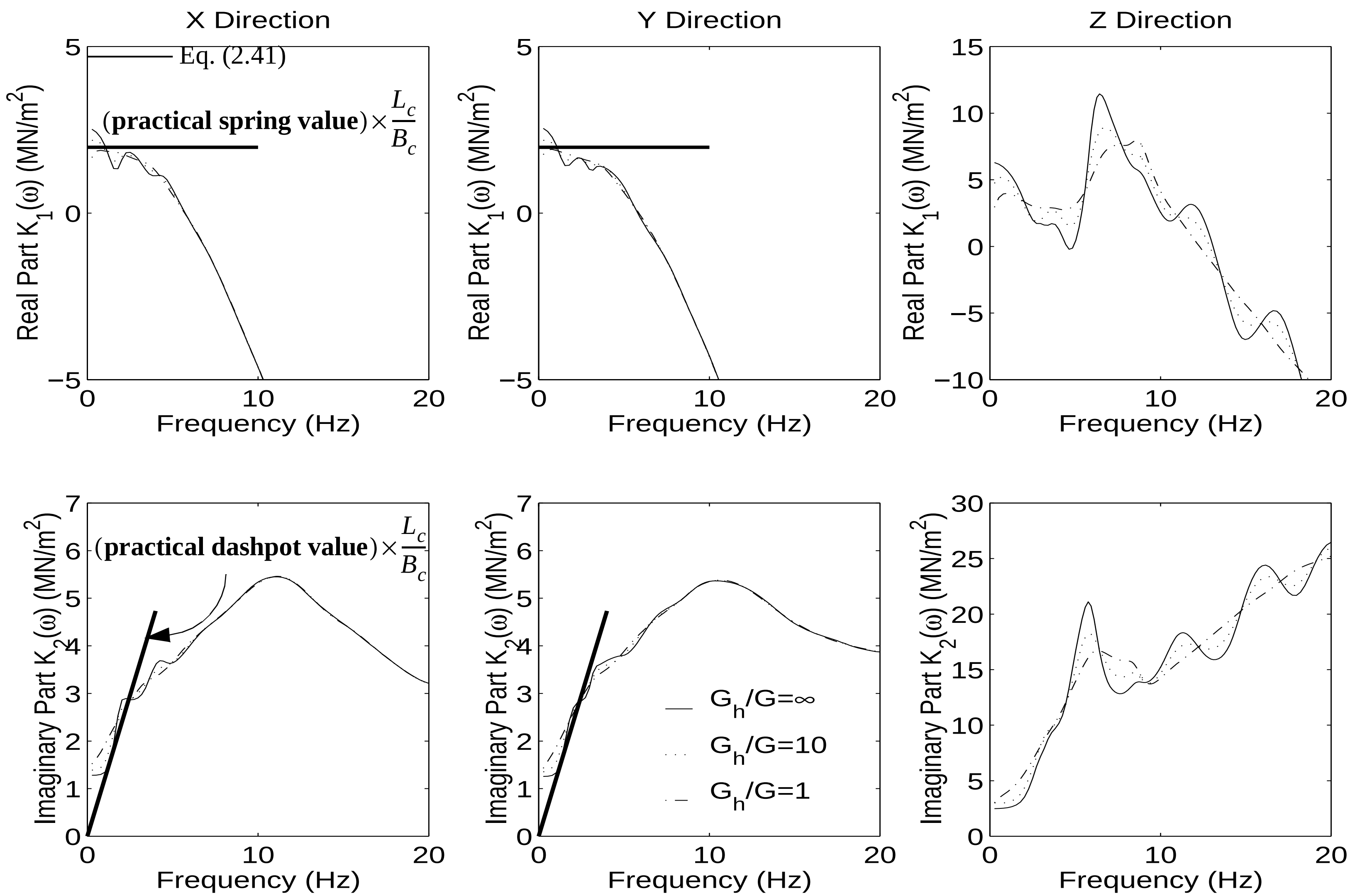

Figure 2.22. Dynamic stiffnesses of approach embankment of Meloland Road Overcrossing ($G = 2.0MPa$, $\eta = 0.52$). Spring and dashpot values shown in Figure 1.1 are extracted by multiplying values shown above with width of embankment, B_c. Stiffness and damping values along longitudinal (y) direction are equal to those of transverse direction.

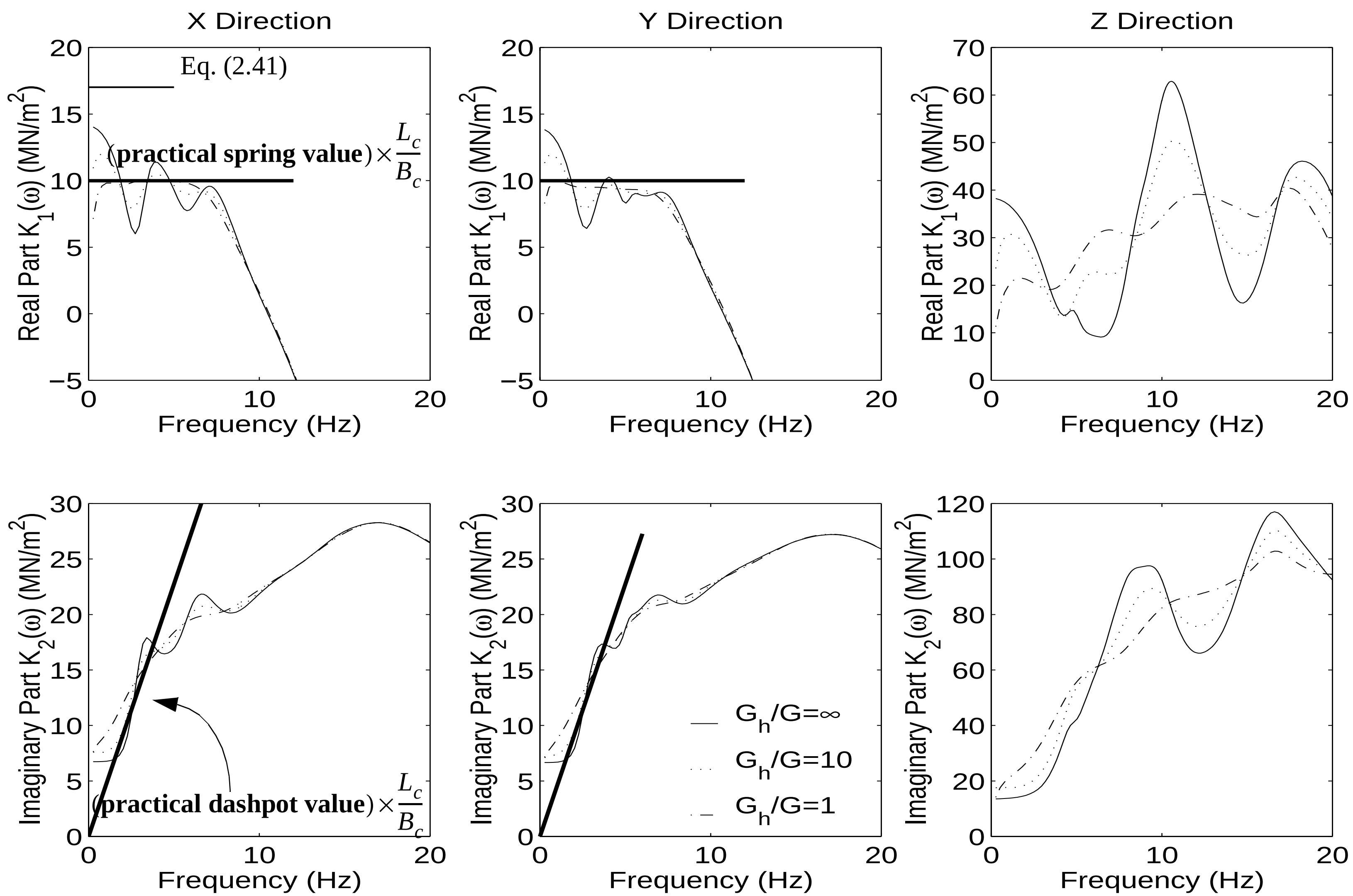

Figure 2.23. Dynamic stiffnesses of approach embankment of Painter Street Bridge (G = $8.0MPa$, η = 0.50). Spring and dashpot values shown in Figure 1.1 are extracted by multiplying values shown above with width of embankment, B_c. Stiffness and damping values along longitudinal (y) direction are equal to those of transverse direction.

2.3.4 Estimation of Critical Length L_c

While 3-D finite element calculations are necessary in this study to establish the dynamic stiffnesses of approach embankments, our study proceeds with the development of a practical procedure that allows for the estimation of the dynamic stiffnesses of the embankments by using the stiffness and damping values of a unit-width shear wedge and a critical length, L_c. The transverse mechanical behavior of an infinitely long embankment due to a concentrated load at one end is idealized with a series of unit-width wedges interacting in shear with one another. Figure 2.24 shows a long embankment subjected to a transverse load, P_x, at its front end and a slice of the embankment with width, dy. Within the context of 1-D analysis the equilibrium of the section along the transverse direction gives

$$Q(y) + \frac{d}{dy}Q(y) - Q(y) - \hat{k}_x u_x(y)dy = 0 \tag{2.31}$$

which gives

$$\frac{d}{dy}Q(y) - \hat{k}_x u_x(y) = 0 \tag{2.32}$$

In equations (2.31) and (2.32), $u_x(y)$ is the transverse displacement of some reference point on the section, $\hat{k}_x$ is the static stiffness of the unit-width wedge given by (2.16) or (2.19), and $Q(y)$ is the shear force on the face of the section of the slice that is approximated with

$$Q(y) = AG\frac{d}{dy}u_x(y) \tag{2.33}$$

substitution of (2.16) and (2.33) into (2.32) gives

$$AG\frac{d^2}{dy^2}u_x(y) - \frac{2G}{S\ln\left(1 + \frac{2H}{SB_c}\right)}u_x(y) = 0 \tag{2.34}$$

Equation (2.34) reduces to

$$\frac{d^2}{dy^2}u_x(y) - \lambda^2 u_x(y) = 0 \tag{2.35}$$

where

$$\lambda = \sqrt{\frac{2}{AS\ln\left(1 + \frac{2H}{SB_c}\right)}} \tag{2.36}$$

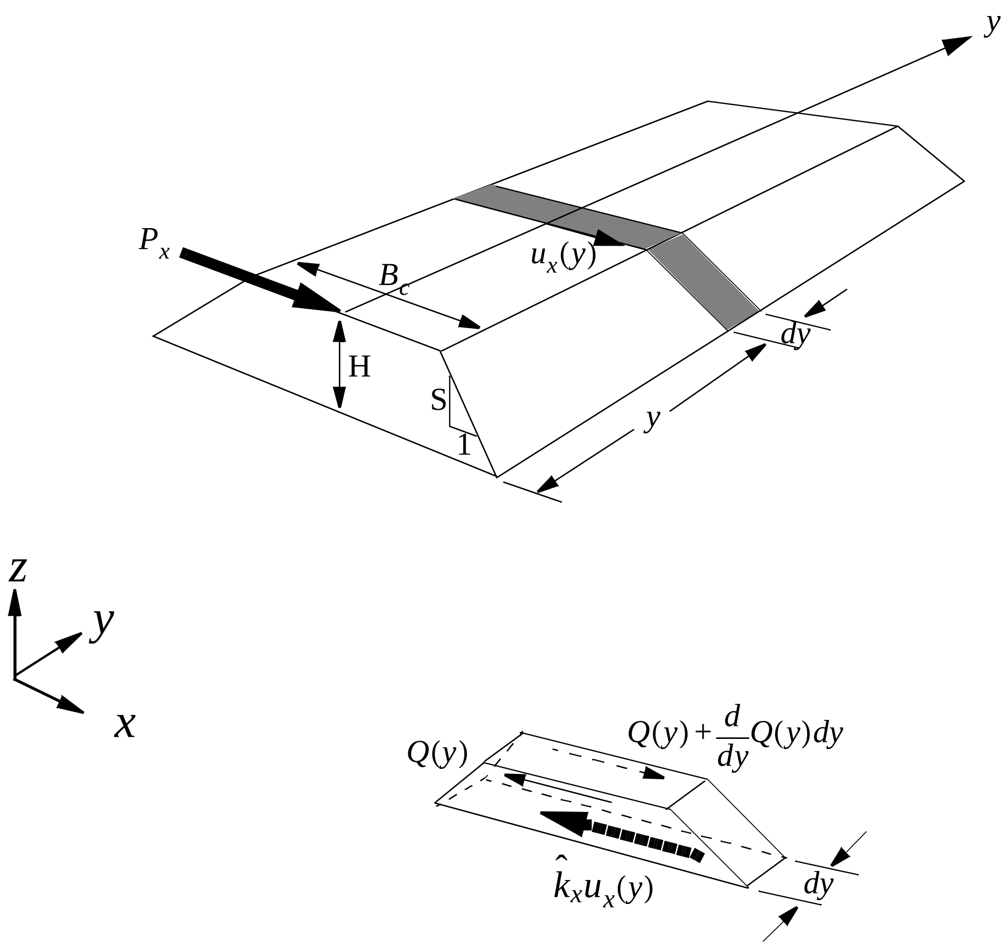

Figure 2.24. Free-body diagram of a section of a long embankment under transverse loading at one end

Using that at large values of y the displacement, $u_x(y)$, vanishes, the solution of (2.35) becomes

$$u_x(y) = Ce^{-\lambda y} \tag{2.37}$$

where C is an integration constant that is determined from the boundary conditions. The force at the origin is given by (2.33) after setting $y = 0$

$$P = -Q(0) = -AGC(-\lambda) \tag{2.38}$$

from which

$$C = \frac{P}{AG\lambda} \tag{2.39}$$

Substitution of (2.39) to (2.37) gives the approximate expression for the displacement distribution

$$u_x(y) = \frac{P}{AG\lambda}e^{-\lambda y} \tag{2.40}$$

which when evaluated at $y = 0$ gives an estimate of the dynamic stiffness of the embankment

$$K_x = \frac{P}{u_x(0)} = AG\lambda = G\sqrt{\frac{2A}{S\ln\left(1+\frac{2H}{SB_c}\right)}} \tag{2.41}$$

Equation (2.41) is the extension of the solution for the dynamic stiffness of the unit-width wedge that was derived by Wilson and Tan (1990a). Equation (2.41) in association with (2.16) yield an expression for the critical length, L_c, that is needed to multiply the static stiffness of the unit-width wedge to estimate the transverse stiffness of the embankment. Wilson and Tan (1990b) have assumed that L_c should be approximately the length of the wing wall. In this study we conclude that

$$K_x = G\sqrt{\frac{2A}{S\ln\left(1+\frac{2H}{SB_c}\right)}} = L_c\hat{k}_x = L_c\frac{2G}{S\ln\left(1+\frac{2H}{SB_c}\right)} \tag{2.42}$$

which gives

$$L_c = \frac{\sqrt{2}}{2}\cdot\sqrt{AS\ln\left(1+\frac{2H}{SB_c}\right)} \tag{2.43}$$

Equation (2.43) indicates that the critical length is independent of the shear modulus, G, and is proportional to the square root of the area, A, and the slope of the embankment, S.

Equation (2.43) was derived by relating the expression of the static stiffness of the unit-width wedge to the approximate closed-form expression of the static stiffness of the embankment given by (2.41). If instead of the values provided by (2.41) one uses the more exact finite element results, the foregoing analysis suggests that a good candidate expression for the critical length, L_c, is

$$L_c = \frac{K_x}{\hat{k}_x} = \alpha\sqrt{SB_cH} \tag{2.44}$$

where the quantity $\sqrt{SB_cH}$ accommodates the physics that emerges from $\sqrt{AS\ln(1 + 2H/(SB_c))}$ and α is a dimensionless coefficient that is expected to be nearly independent of the geometry. Figure 2.25 plots the coefficient, $\alpha = K_x/(\hat{k}_x\sqrt{SB_cH})$ for various embankment geometries. Figure 2.25 indicates that $\alpha \approx 0.7$ is indeed nearly independent of geometry for the embankment configurations of interest. Therefore, it is suggested that the critical length, L_c, is given by

$$L_c \approx 0.7\sqrt{SB_cH} \tag{2.45}$$

The concept of the critical length, L_c, which relates the stiffness of the unit-width wedge to the stiffness of the embankment, is extended for the case of damping. Accordingly, it is proposed that the dynamic stiffness of the embankment is given by

$$\mathcal{K}_x = \hat{\mathcal{k}}_x(\omega) \cdot L_c \tag{2.46}$$

where $\hat{\mathcal{k}}_x(\omega)$ is the dynamic stiffness of the unit-width wedge given by (2.27) and L_c is a critical length that is given by (2.45). The good estimates for the stiffness and dashpot values given by (2.46) where the critical length is given by (2.45), is shown in Figure 2.22 and 2.23 together with the 3-D finite element solutions.

2.3.5 Summary of Procedure to Compute the Spring and Dashpot Values of Bridge Embankments

1. Compute the dynamic stiffness of the unit-width shear wedge using equation (2.27). The values of G and η in this equation are the converged values obtained from the calculation of the kinematic response functions.

2. Plot the real and imaginary part of equation (2.27) as a function of frequency (wave number $k = \omega/V_s/(1 + i\eta)$ and $V_s = \sqrt{G/\rho}$).

3. Select practical spring and dashpot values by passing a horizontal line through the graph of the real part and an inclined line through the graph of the imaginary part at locations that capture with satisfaction the low frequency behavior (see Figures 2.19 and 2.20). If only spring values are of

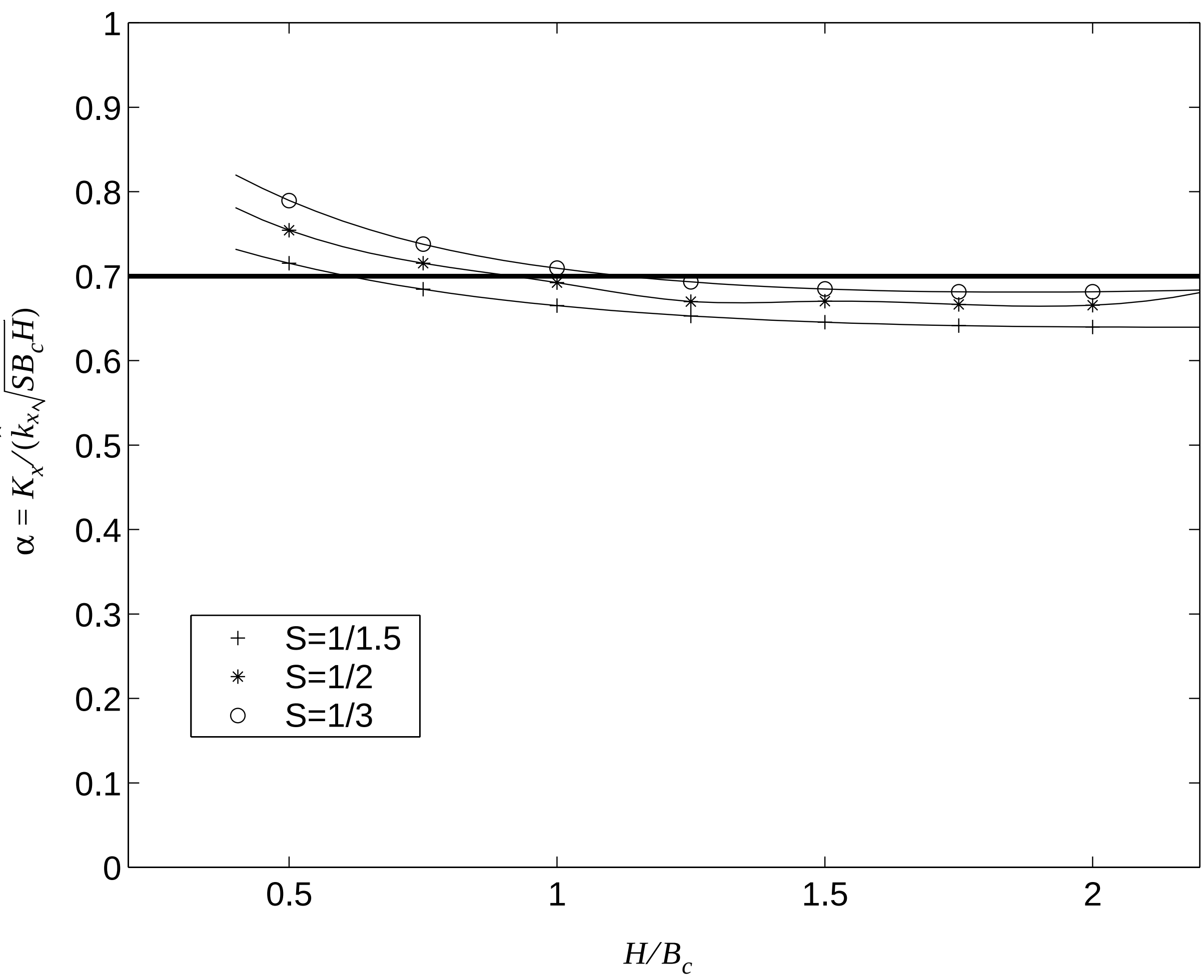

Figure 2.25. Critical length parameter $\alpha = K_x/(\hat{k}_x\sqrt{SB_cH})$ for various geometries

interest, steps 1 to 3 can be avoided by merely using the Wilson and Tan (1990a) expressions (equations (2.16) and (2.17)) or the more general expressions offered by equations (2.19) and (2.20). Steps 1 to 3 are primarily needed to estimate the dashpot values.

4. Compute the transverse spring and dashpot values of the embankment by multiplying the values indicated by the lines identified in step 3 with the critical length, $L_c \approx 0.7\sqrt{SB_cH}$.

5. Use the spring and dashpot values computed in step 4 for the longitudinal spring and dashpot values.

3 Dynamic Stiffnesses of Pile Foundations

3.1 INPUT MOTION AT PILE CAPS

The difference between the free-field motion and the motion at the cap of a pile foundation is due to the scattered wave field generated from the difference between pile and soil rigidities. Nevertheless, for motions that are not rich in high frequencies, the scattered field is weak, and the support motion can be considered to be approximately equal to that of the free field (Fan et al. 1991; Gazetas 1984; Kaynia and Novak 1992; Makris and Gazetas 1992; Mamoon and Banerjee 1990; Tajimi 1977). For instance, for Painter Street Bridge the soil deposit has an average shear velocity, V_s, of about 200 m/s (Heuze and Swift 1991); the pile diameter d is 0.36 m. Accordingly, even for the high-frequency content of the input motion ($f \approx 10\ Hz$), the dimensionless frequency, $a_0 = 2\pi fd/V_s$, is of the order of only 0.1. From studies on vertically propagating shear waves in homogeneous soil deposits (Fan et al. 1991), the kinematic-seismic response factors (head-group displacement over free-field displacement) are very close to unity, even at values of the dimensionless frequency, $a_0 > 0.1$.

Waves other than vertical S-waves also participate in ground shaking. Seismic-kinematic response factors for SV waves, P waves and Rayleigh surface waves are given by Mamoon and Banerjee (1990), Kaynia and Novak (1992), Makris (1994) and Makris and Badoni (1995). For all these types of waves that produce a vertical component of the seismic input motion, the kinematic response factors are also close to unity. Only in some cases do SV waves with a high angle of incidence result in kinematic response factors of the order of 0.90. Based on such supporting analytical evidence, in most cases the excitation input motion at the level of the pile foundation can be assumed to be equal to that of the free-field motion. Only at very high frequencies or for very soft soils will a reduction be needed. Moreover, in the case of Rayleigh waves and SV waves, a pile group produces an effective rocking input motion, whereas for oblique incidence SH waves the foundation experiences torsional excitation. These motions are the result of phase differences that the seismic input has at the locations of different piles in the group (wave passage effect); their intensity depends on the frequency content of the seismic input and the geometry of the pile group.

3.2 DYNAMIC STIFFNESSES OF A SINGLE PILE

3.2.1 Lateral Dynamic Stiffness of a Single Pile

Figure 3.1 (top) depicts the storage stiffness (real part) and loss stiffness (imaginary part) of a single pile under lateral harmonic excitation. The solid lines are the result of a rigorous numerical solution (for cylindrical pile with finite length $L/d = 15$, $E_p/E_s = 1000$) obtained by Kaynia and Kausel (1982), based on an integral equation formulation. The dashed lines are the results of an analytical solution (for an infinitely long pile) derived by Makris and Gazetas (1993), where pile-soil interaction is realistically represented through a dynamic Winkler model with frequency dependent spring, $k_x(\omega)$, and dashpot, $c_x(\omega)$, coefficients.

$$\mathcal{K}_x^{[1]}(\omega) = K_{1x}^{[1]}(\omega) + iK_{2x}^{[1]}(\omega) = \frac{E_p I_p R^3 (r_1^2 + r_2^2)}{r_1 - ir_2} \tag{3.1}$$

where $E_p I_p$ is the flexural rigidity of the pile and

$$r_1 = -a^3 - b^3 + 3a^2 b + 3ab^2 \tag{3.2}$$

$$r_2 = a^3 - b^3 + 3a^2 b - 3ab^2 \tag{3.3}$$

For values of the excitation frequency, ω, less than the characteristics frequency of the pile-soil system, $\overline{\omega_x} = (k_x(\omega)/m)^{1/2}$ (m being the pile mass per length), the values of R, a, and b are

$$R = \left(\frac{(k_x(\omega) - m\omega^2)^2 + (\omega c_x(\omega))^2}{(4I_p E_p)^2}\right)^{1/8} \tag{3.4}$$

$$a = \cos\frac{\theta}{4} + \sin\frac{\theta}{4}, \quad b = \cos\frac{\theta}{4} - \sin\frac{\theta}{4} \tag{3.5}$$

$$\theta = \operatorname{atan}\left(\frac{\omega c_x(\omega)}{k_x(\omega) - m\omega^2}\right), \qquad 0 < \theta < \frac{\pi}{2} \tag{3.6}$$

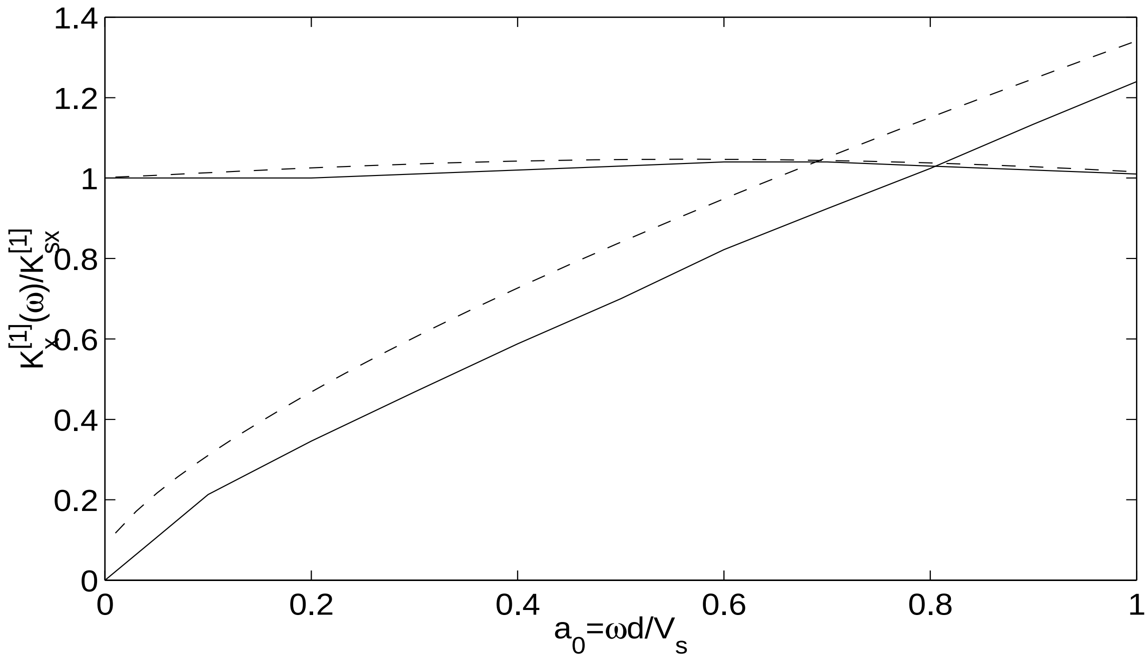

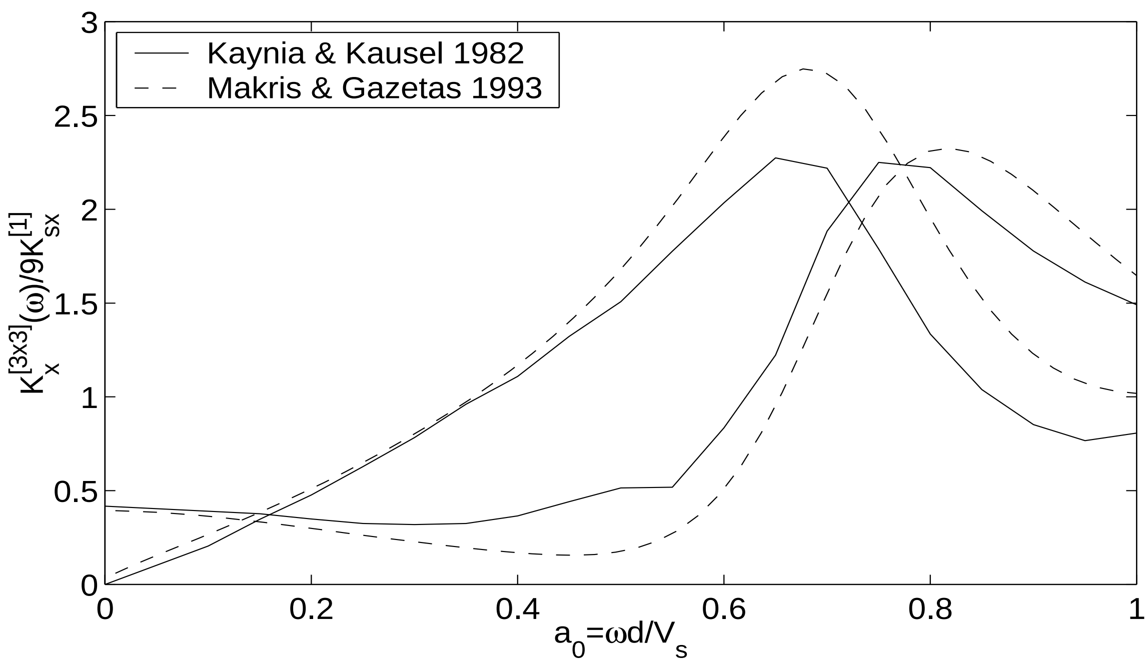

Figure 3.1. Comparison of storage (real part) and loss (imaginary part) stiffness factors along horizontal direction obtained with approximate analytical method (dashed lines) against rigorous solution of Kaynia and Kausel (solid line) for single pile (top) and 3 by 3 square group with rigid pile cap and pile spacing, $S/d = 5$ (bottom). $E_p/E_s = 1000$, $\rho_p/\rho_s = 1.42$, $L/d = 15$, $\beta_s = \eta/2 = 0.05$, $\nu = 0.4$, homogeneous halfspace.

and for values of $\omega > \overline{\omega_x} = (k_x(\omega)/m)^{1/2}$, the values of R, a, and b are

$$R = \left(\frac{(k_x(\omega) - m\omega^2)^2 + (\omega c_x(\omega))^2}{(I_p E_p)^2}\right)^{1/8} \tag{3.7}$$

$$a = \cos\frac{\theta}{4}, \qquad b = -\sin\frac{\theta}{4} \tag{3.8}$$

$$\theta = \operatorname{atan}\left(\frac{-\omega c_x(\omega)}{-k_x(\omega) + m\omega^2}\right), \qquad -\frac{\pi}{2} < \theta < 0 \tag{3.9}$$

The closed-form expression for the lateral dynamic stiffness of the single pile given by (3.1) can accommodate any variation with frequency of the distributed spring and dashpot coefficients. For example, such spring and dashpot coefficients can be obtained using Novak's plane-strain elasto-dynamic solution (Novak et al. 1978). Herein the expressions used for $k(\omega)$ and $c(\omega)$ to compute the values of the lateral dynamic stiffness of the single pile shown in Figure 3.1 with dashed line are given by (Makris and Gazetas 1992; Makris and Gazetas 1993):

$$k_x \approx 1.2 E_s \tag{3.10}$$

$$c_x = (c_x)_{rad} + (c_x)_{hyst} \approx 2d\rho_s V_s\left[1 + \left(\frac{V_{La}}{V_s}\right)\right]a_0^{-0.25} + \eta\frac{k_x}{\omega} \tag{3.11}$$

where η is the hysteretic damping coefficient of the soil defined in equation (2.8), ρ_s is mass density, E_s is Young's modulus, V_s is shear-wave velocity of the soil, $a_0 = \omega d/V_s$ is a dimensionless excitation frequency, and V_{La} is an apparent velocity of the compression-extension waves, called "Lysmer's analogue" velocity (Gazetas and Dobry 1984a, 1984b)

$$V_{La} = \frac{3.4}{\pi(1-\nu)}V_s \tag{3.12}$$

where ν is Poisson's ratio of the soil. Equations (3.10) and (3.11) are developed by matching the dynamic pile-head displacement from Winkler and dynamic finite-element analysis (Blaney et al. 1976; Roesset and Angelides 1980; Gazetas and Dobry 1984a, 1984b).

Figure 3.1 (top) shows that the prediction of the closed-form expression given by (3.1), which was derived for an infinitely long flexural beam, is in good agreement with the rigorous solution of Kaynia and Kausel (1982) obtained for a flexural beam with finite length. The reason why the infinite long beam model gives such good results in the case of lateral vibration is discussed in the paper by Makris and Gazetas (1993).

It should be noted that approximate expressions for the lateral dynamic stiffness of a single pile have also been proposed by Gazetas and Dobry (1984a). Instead of equation (3.1), which was not derived at that time, Gazetas and Dobry proposed that the storage stiffness, $K_{1x}^{[1]}(\omega)$ of the single pile for lateral motion to be constant with frequency, equal to its static value $K_{sx}^{[1]}$. Referring to Figure 3.1 (top) this is a realistic approximation for the practical frequency range. Of course at higher frequencies the dynamic stiffness diminishes due to inertia effects and eventually reaches negative values. For the loss stiffness $K_{2x}^{[1]}(\omega)$, they proposed the following engineering approximation

$$K_{2x}^{[1]}(\omega) = \omega\int_0^L c_x(\omega)Y_{sx}^2(z)dz \tag{3.13}$$

where $c(\omega)$ is given by (3.11) and Y_{sx} is the static deflection profile normalized to the unit top-amplitude. So for the low-frequency range, Gazetas and Dobry's approximation for the lateral dynamic stiffness of the single pile is

$$\mathcal{K}_x^{[1]}(\omega) = K_{1x}^{[1]}(\omega) + iK_{2x}^{[1]}(\omega) = K_{sx}^{[1]} + i\omega\int_0^L c_x(\omega)Y_{sx}^2(z)dz \tag{3.14}$$

For a homogeneous deposit equation (3.14) is not as convenient and realistic as (3.1) which is the closed-form solution of the dynamic problem. Nevertheless, when the soil is a layered deposit with different mechanical properties per layer, equation (3.14) becomes a practical alternative.

3.2.2 Vertical and Rocking Dynamic Stiffnesses of a Single Pile

For the case of a vertical and rocking vibrational mode, closed-form solutions for the dynamic stiffnesses of a single pile are not known. Accordingly, one has to use results from rigorous numerical analyses or experimental investigations. Some efforts have been conducted to justify approximate expressions similar to equation (3.14) for the case of vertical vibrational mode (Kanakari 1990). As an example, for a homogeneous soil deposit an approximation to the vertical stiffness of a single pile at the low-frequency range $a_0 < 1$ is

$$\mathcal{K}_z^{[1]}(\omega) = K_{1z}^{[1]}(\omega) + iK_{2z}^{[1]}(\omega) = K_{sz}^{[1]} + i\omega\int_0^L c_z(\omega)Y_{sz}^2(z)dz \tag{3.15}$$

where

$$k_z(\omega) \approx 0.6E_s\left(1 + \frac{1}{2}\sqrt{a_0}\right) \tag{3.16}$$

$$c_z(\omega) = (c_z)_{rad} + (c_z)_{hyst} \approx 1.2a_0^{-0.25}\pi d\rho_s V_s + \eta\frac{k_z(\omega)}{\omega} \tag{3.17}$$

where η is the hysteretic damping of the soil defined in equation (2.8).

It should be emphasized that many procedures and methods are available to estimate the dynamic stiffnesses of a single pile. The approximate expressions (3.1), (3.14), and (3.15) are attractive since they provide the stiffnesses of a single pile without involving sophisticated analysis procedure. Nevertheless, it is the engineer's task to select the best procedure(s) available to obtain the dynamic stiffnesses of the single pile.

For the extreme case of very long piles, the pile is idealized as an elastic "thin" rod with mass per unit length, m, that is attached to the surrounding soil with vertical distributed springs, $k_z(\omega)$, and dashpots, $c_z(\omega)$. For this special case the vertical dynamic stiffness of the single pile is given by

$$\mathcal{K}_z^{[1]} = K_{1z}^{[1]}(\omega) + iK_{2z}^{[1]}(\omega) = \frac{RE_pA_p}{\cos\frac{\theta}{2} - i\sin\frac{\theta}{2}} \text{ when } \omega < \overline{\omega}_z = \sqrt{\frac{k_z(\omega)}{m}}. \tag{3.18}$$

In equation (3.18),

$$R = \left(\frac{(k_z(\omega) - m\omega^2)^2 + (\omega c_z(\omega))^2}{(A_pE_p)^2}\right)^{1/4} \tag{3.19}$$

and

$$\theta = \operatorname{atan}\left(\frac{\omega c_z(\omega)}{k_z(\omega) - m\omega^2}\right), 0 < \theta < \frac{\pi}{2}. \tag{3.20}$$

When $\omega > \overline{\omega}_z = \sqrt{\frac{k_z(\omega)}{m}}$ the vertical dynamic stiffness of the single pile is

$$\mathcal{K}_z^{[1]} = K_{1z}^{[1]}(\omega) + iK_{2z}^{[1]}(\omega) = \frac{-RE_pA_p}{\sin\frac{\theta}{2} + i\cos\frac{\theta}{2}} \tag{3.21}$$

where R is given by (3.19) and

$$\theta = \operatorname{atan}\left(\frac{\omega c_z(\omega)}{k_z(\omega) - m\omega^2}\right), -\frac{\pi}{2} < \theta < 0 \tag{3.22}$$

Figure 3.2 plots the real and imaginary part of the vertical dynamic stiffness of a single pile computed by Kaynia and Kausel ($L/d = 15$, $E_p/E_s = 1000$) and the results from equations (3.18) and (3.21).

3.3 DYNAMIC STIFFNESSES OF PILE GROUP

The dynamic stiffnesses of a pile group, in any vibration mode, can be computed using the dynamic stiffnesses of a single pile in conjunction with the concept of superposition criterion, originally developed for static loads by Poulos (1968), and later justified for dynamic loads by Kaynia and Kausel (1982), Sanchez-Salinero (1983) and Roesset (1984). It can be used with confidence at least for groups with less than 50 piles. Dynamic interaction factors for various modes of loading are available in the form of non-dimensional graphs (Gazetas et al. 1991) and in some cases, closed form expressions derived from a beam on winkler foundation model in conjunction with simplified wave-propagation theory (Dobry and Gazetas 1988; Makris and Gazetas 1992).

3.3.1 Lateral Dynamic Stiffness of Pile Group

The horizontal dynamic interaction factor for two piles in a homogeneous stratum takes the form:

$$\alpha_x(S, \theta) = \alpha_x(S, 0)\cos^2\theta + \alpha_x\left(S, \frac{\pi}{2}\right)\sin^2\theta \tag{3.23}$$

where

$$\alpha_x(S, 0) = \frac{3}{4}\psi(S, 0)\frac{k_x(\omega) + i\omega c_x(\omega)}{k_x(\omega) + i\omega c_x(\omega) - m\omega^2} \tag{3.24}$$

$$\alpha_x\left(S, \frac{\pi}{2}\right) = \frac{3}{4}\psi\left(S, \frac{\pi}{2}\right)\frac{k_z(\omega) + i\omega c_z(\omega)}{k_z(\omega) + i\omega c_z(\omega) - m\omega^2} \tag{3.25}$$

where $\psi(r, \theta)$ is an approximate attenuation function proposed in the above mentioned reference.

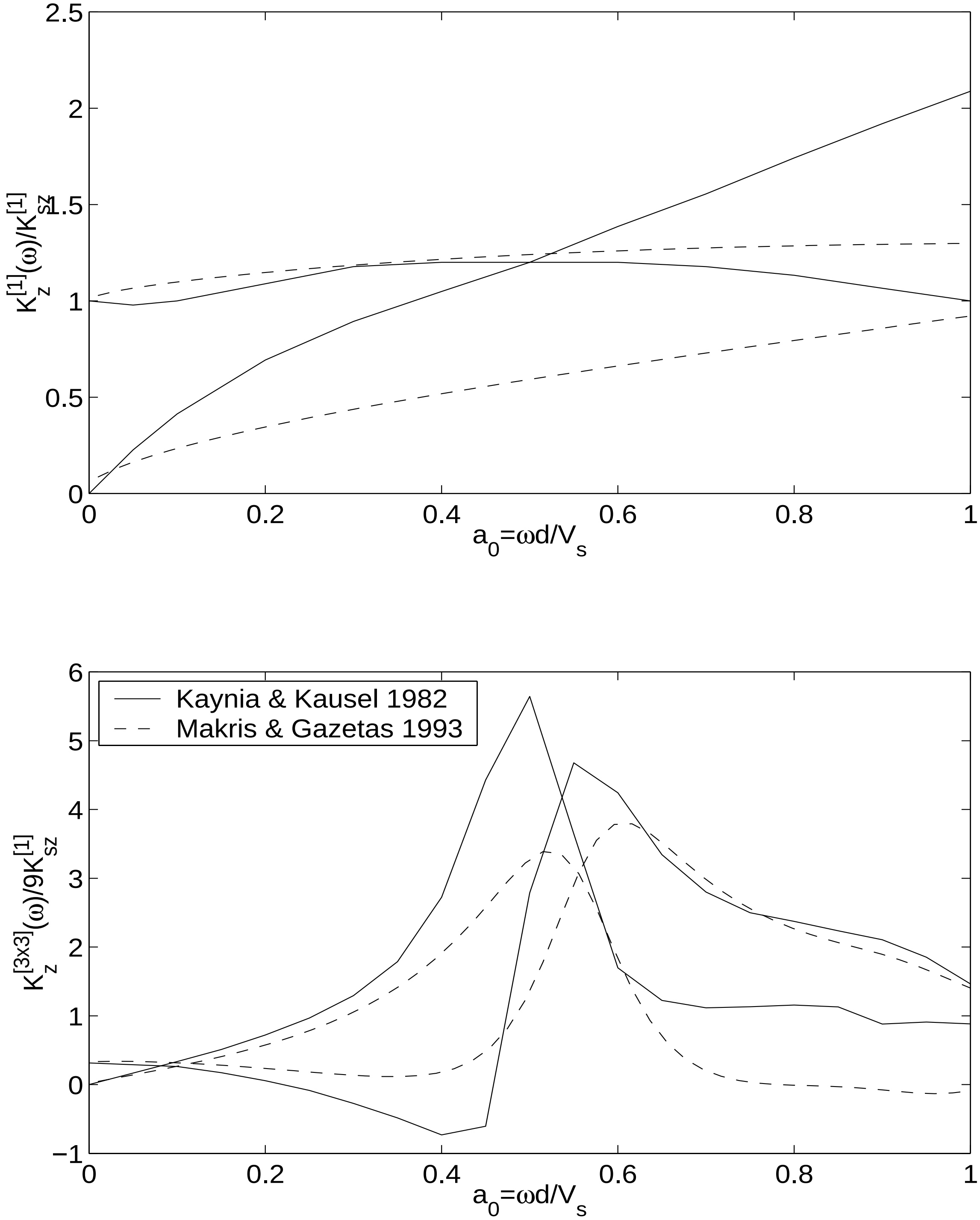

Figure 3.2. Comparison of storage (real part) and loss (imaginary part) stiffness factors along vertical direction obtained with approximate analytical method (dashed lines) against rigorous solution of Kaynia and Kausel (solid line) for single pile (top) and 3 by 3 square group with rigid pile cap and pile spacing, $S/d = 5$ (bottom). $E_p/E_s = 1000$, $\rho_p/\rho_s = 1.42$, $L/d = 15$, $\beta_s = \eta/2 = 0.05$, $\nu = 0.4$, homogeneous halfspace.

$$\psi(S,0) = \left(\frac{d}{2S}\right)^{\frac{1}{2}} \exp\left[-(\beta_s + i)\frac{\omega\left(S-\frac{d}{2}\right)}{V_{La}}\right] \tag{3.26}$$

$$\psi\left(S,\frac{\pi}{2}\right) = \left(\frac{d}{2S}\right)^{\frac{1}{2}} \exp\left[-(\beta_s + i)\frac{\omega\left(S-\frac{d}{2}\right)}{V_s}\right] \tag{3.27}$$

where S is the distance between two piles and θ is the angle between the direction of loading and the line connecting the axes of the two piles.

The lateral dynamic stiffnesses of a group of piles can now be computed using the concept of superposition in association with the dynamic stiffnesses of a single pile and dynamic interaction factors between any two piles (Makris et al. 1994). Let y_i be the horizontal displacement of pile i belonging to a group of N piles. Superposition of displacements leads to

$$y_i = \sum_{j=1}^{N} \alpha_x(i,j) y_j \tag{3.28}$$

where $\alpha_x(i,j)$ is given from Eq. (3.23); $\alpha_x(i,j) = 1$ if $i = j$. The value of y_j is obtained as

$$y_j = \frac{F_j}{\mathcal{K}_x^{[1]}} \tag{3.29}$$

where F_j is the force that *jth* pile carries, and $\mathcal{K}_x^{[1]}$ is the horizontal dynamic stiffness of a single fixed-head pile. Since all piles are connected with a rigid cap, the displacement of pile group, $y^{[G]}$, is equal to y_i for all i. Substitution of (3.29) into (3.28) gives

$$y^{[G]} \mathcal{K}_x^{[1]} = \sum_{j=1}^{N} \alpha_x(i,j) F_j \tag{3.30}$$

Repeating (3.30) for all N piles of the pile group, one obtains the matrix equation

$$\begin{bmatrix} \alpha_x(1,1) & \alpha_x(1,2) & \dots & \alpha_x(1,N) \\ \alpha_x(2,1) & \alpha_x(2,2) & \dots & \alpha_x(2,N) \\ . & . & & . \\ \alpha_x(N,1) & \alpha_x(N,2) & \dots & \alpha_x(N,N) \end{bmatrix} \begin{bmatrix} F_1 \\ F_2 \\ . \\ F_N \end{bmatrix} = y^{[G]} \mathcal{K}_x^{[1]} \begin{bmatrix} 1 \\ 1 \\ . \\ 1 \end{bmatrix} \tag{3.31}$$

Eq. (3.31) can be solved for the force vector

$$F_i = y^{[G]} \mathcal{K}_x^{[1]} \sum_{j=1}^{N} \varepsilon_x(i,j) \tag{3.32}$$

where $\varepsilon_x(i,j)$ is the element of the inverse of matrix $\alpha_x(i,j)$. Since $P_x^{[G]} = \mathcal{K}_x^{[G]} y^{[G]} = \sum_{i=1}^{N} F_i$, the lateral dynamic stiffness of the pile group for the horizontal mode is simply

$$\mathcal{K}_x^{[G]} = \mathcal{K}_x^{[1]} \sum_{i=1}^{N} \sum_{j=1}^{N} \varepsilon_x(i,j) \tag{3.33}$$

3.3.2 Vertical and Rocking Dynamic Stiffnesses of Pile Group

In these two cases where the pile motion is along the axial direction, the dynamic interaction factor for two piles in a homogeneous stratum is simply

$$\alpha_z = \left(\frac{d}{2S}\right)^{\frac{1}{2}} \exp\left[-(\beta_s + i)\frac{\omega\left(S - \frac{d}{2}\right)}{V_s}\right] \tag{3.34}$$

The vertical dynamic stiffness of the group is also given by an analysis similar to the one presented for lateral loading, where index *x* is replaced by *z*. Accordingly

$$\mathcal{K}_z^{[G]} = \mathcal{K}_z^{[1]} \sum_{i=1}^{N} \sum_{j=1}^{N} \varepsilon_z(i,j) \tag{3.35}$$

where $\varepsilon_z(i,j)$ is the element of the inverse of matrix $\alpha_z(i,j)$ obtained from (3.34).

The rocking group-dynamic stiffness can be derived by an analysis similar to the one previously presented (Dobry and Gazetas 1988; Makris and Gazetas 1993)

$$\mathcal{K}_r^{[G]} = \mathcal{K}_z^{[1]} \sum_{i=1}^{N} x_i \sum_{j=1}^{N} x_j \varepsilon_z(i,j) \tag{3.36}$$

where x_i is the distance of pile i from the axis about which the rotation occurs.

For the cross-horizontal-rocking interaction factor it has been found (Gazetas et al. 1991) that the following approximation proposed by Randolph (1977) for the static loaded piles is also valid for dynamic loads:

$$\alpha_{xr}(i,j) \approx \alpha_x^2(i,j) \tag{3.37}$$

Accordingly, the cross-horizontal-rocking group stiffness is

$$\mathcal{K}_{xr}^{[G]} = K_{xr}^{[1]} \sum_{i=1}^{N} \sum_{j=1}^{N} \varepsilon_{xr}(i,j) \tag{3.38}$$

where $\varepsilon_{xr}(i,j)$ is the element of inverse of matrix $\alpha_{xr}(i,j)$ given by (3.37). The static stiffness $K_{xr}^{[1]}$ of the single fixed-head pile is approximated by

$$K_{xr}^{[1]} \approx -0.22 E_s d^2 \left(\frac{E_p}{E_s}\right)^{0.5} \tag{3.39}$$

3.3.3 Spring and Dashpot Values of the Pile Foundations of the Meloland Road Overcrossing and the Painter Street Overcrossing

Figures 3.3 and 3.4 show the configurations of the pile groups at the center bent and abutments of the Meloland Road Overcrossing. Figures 3.5 and 3.6 show the pile group configurations at the center bent and abutments of the Painter Street Bridge. Figure 3.7 plots the normalized group dynamic stiffnesses as a function of the dimensionless frequency, $a_0 = \omega d / V_s$, of the 5 by 5 pile group of the center bent of the Meloland Road Overcrossing, whereas Figure 3.8 plots the normalized group dynamic stiffnesses as a function of the dimensionless frequency, $a_0 = (\omega d) / V_s$, of the 4 by 5 pile group of the center bent of the Painter Street Bridge. The static group stiffness is only a fraction of the sum of the individual pile static stiffnesses. Both cases show the significance of the interaction between piles. Figure 3.9 plots the normalized dynamic pile group stiffnesses at the abutments of the Meloland Road Overcrossing, while Figures 3.10 and 3.11 plot the normalized dynamic pile group stiffnesses at the west and east abutments of the Painter Street Bridge. Figures 3.7 to 3.11 indicate a vivid fluctuation of the real and imaginary parts of the dynamic stiffnesses with frequency. However, during strong shaking additional phenomena associated with nonlinear soil behavior are present that are not represented in this analysis. Nonlinear behavior, even when local, has a tendency to suppress fluctuations with frequency (Badoni and Makris 1997). This observation motivated us to abandon the frequency dependence of pile foundations and adopt a single frequency-independent spring value for the storage stiffness that is equal to the computed static stiffness; and a single frequency-independent damping value for the damping coefficient $c = K_2(\omega) / \omega$. Table 3.1 summarizes the spring and dashpot values of the pile groups of the two instrumented bridges that are the subject of this study.

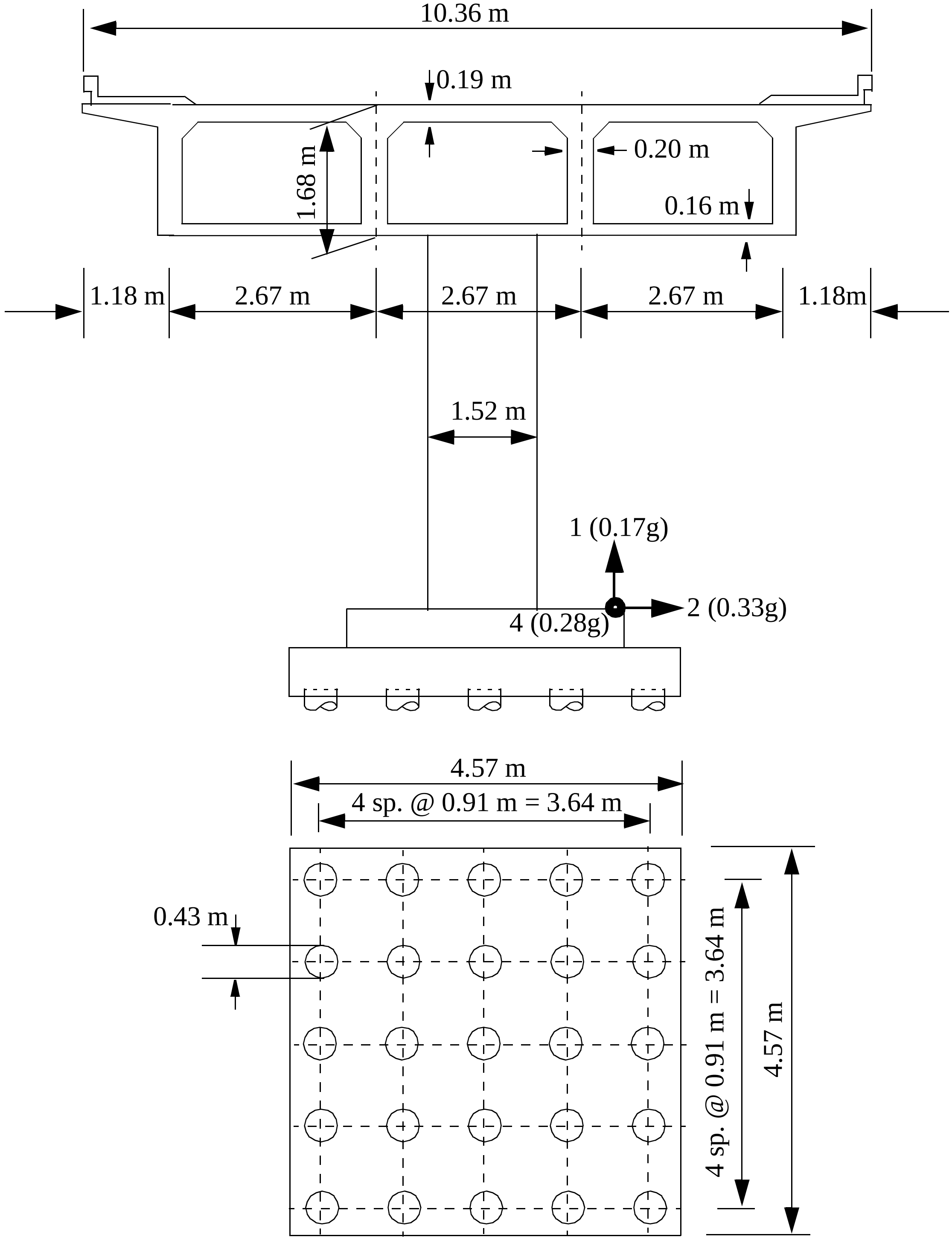

Figure 3.3. Cross-section view of Meloland Road Overcrossing and plan view of pile group at center bent

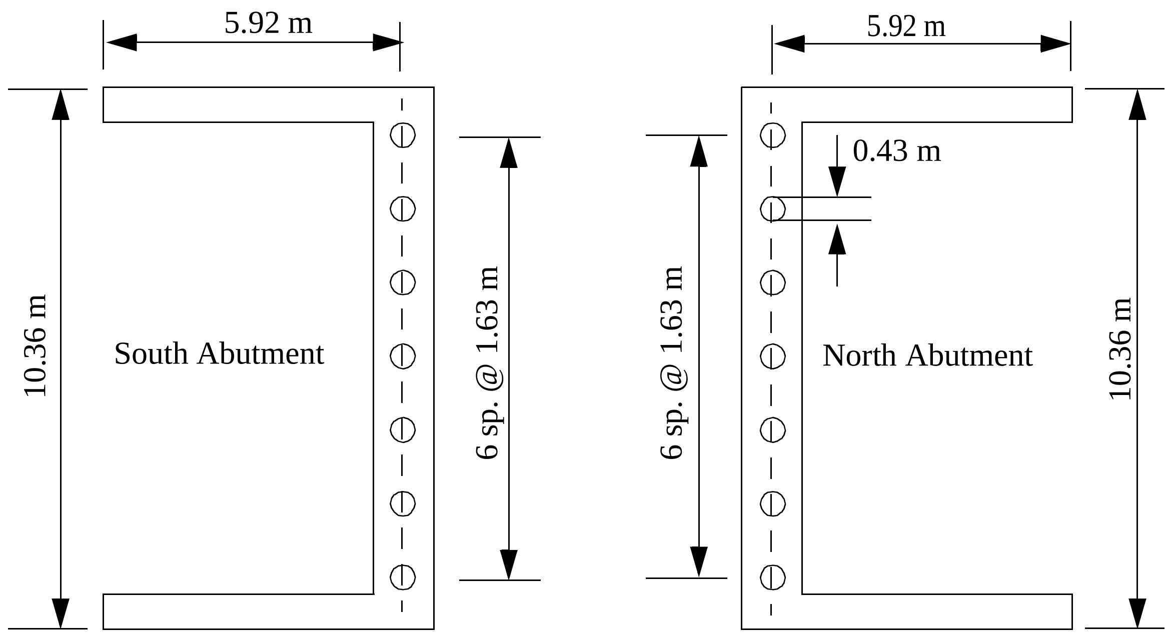

Figure 3.4. Plan view of pile groups at south and north abutments of Meloland Road Overcrossing

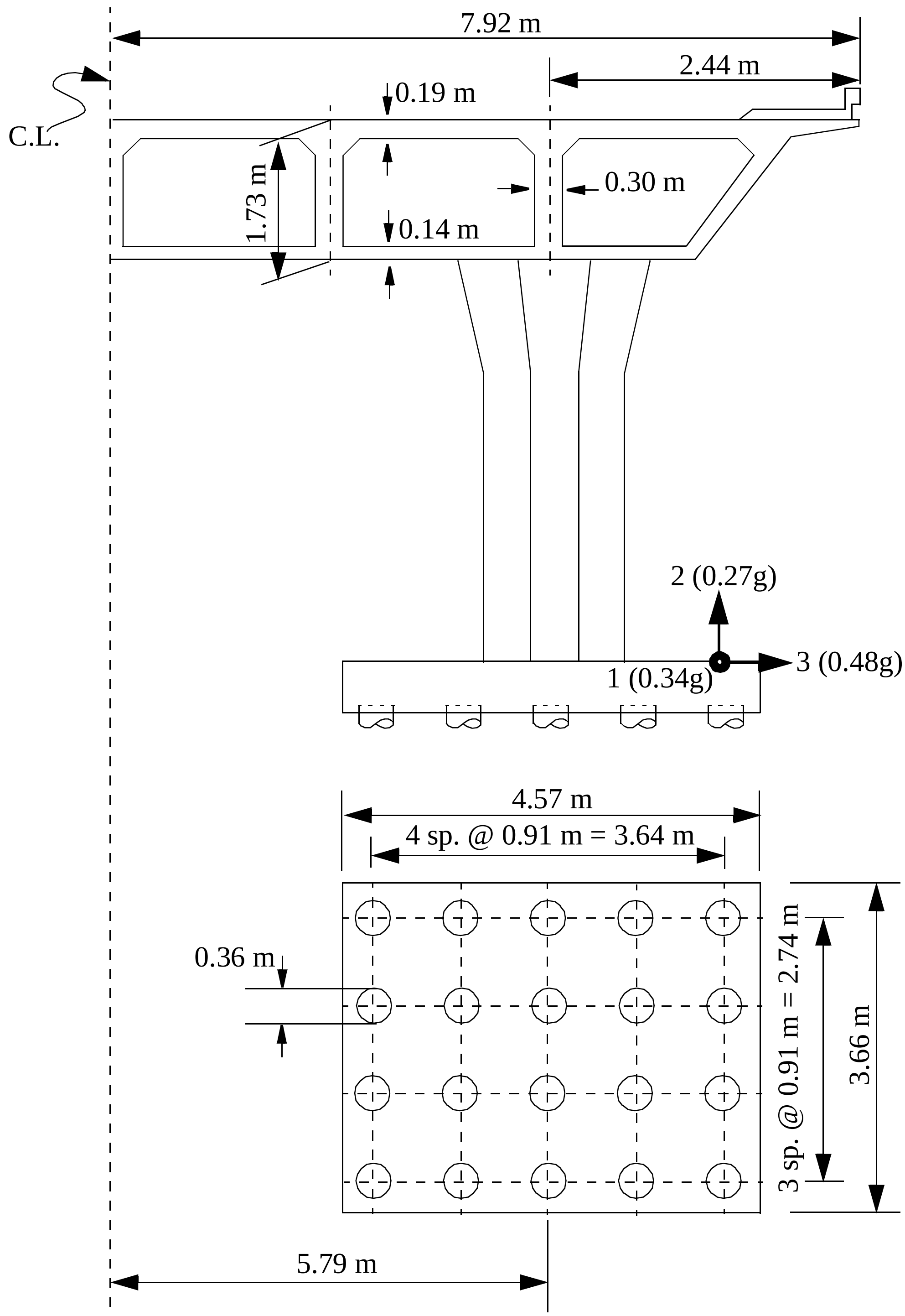

Figure 3.5. Cross-section view of Painter Street Overcrossing and plan view of pile group at center bent

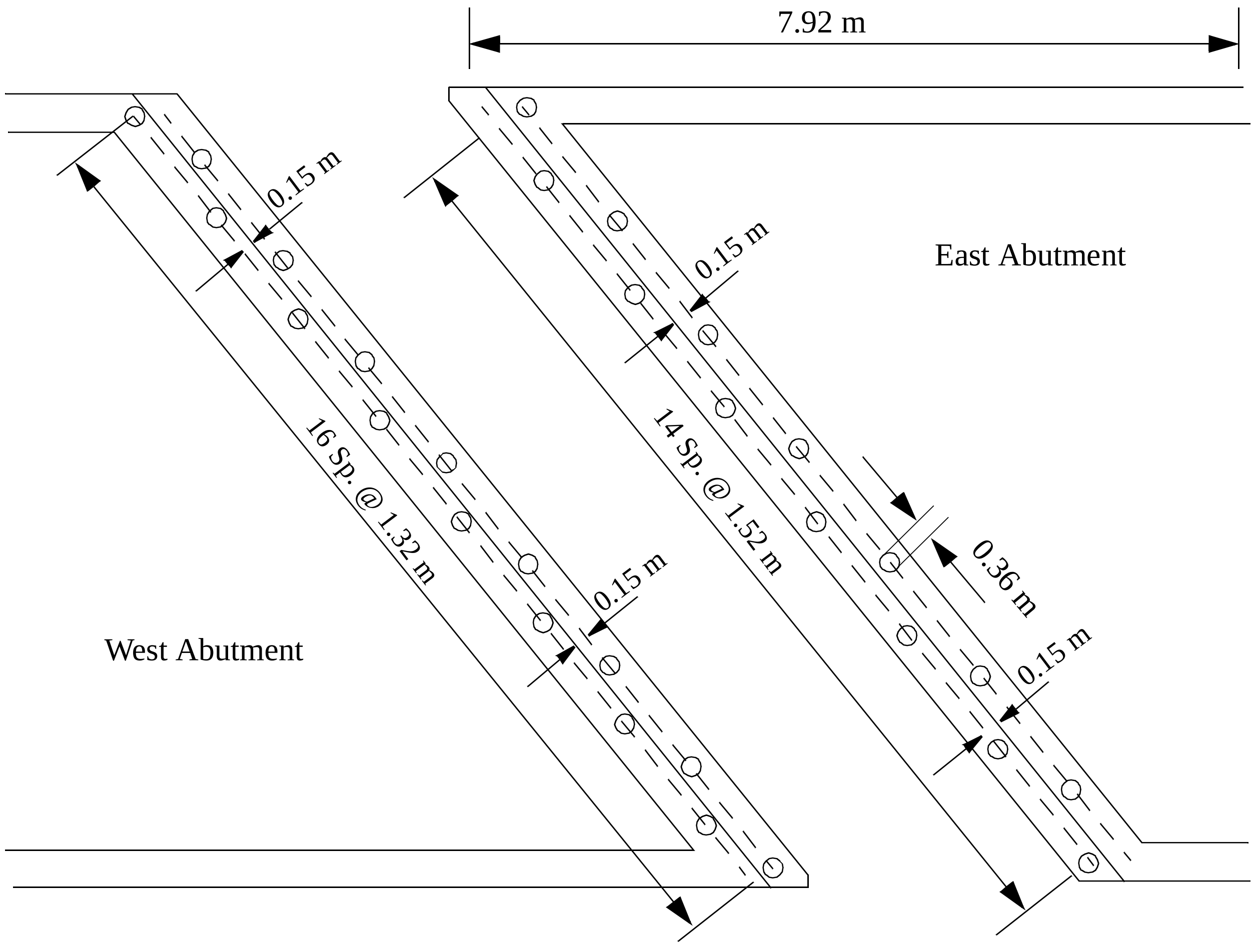

Figure 3.6. Plan view of pile groups at west and east abutments of Painter Street Overcrossing

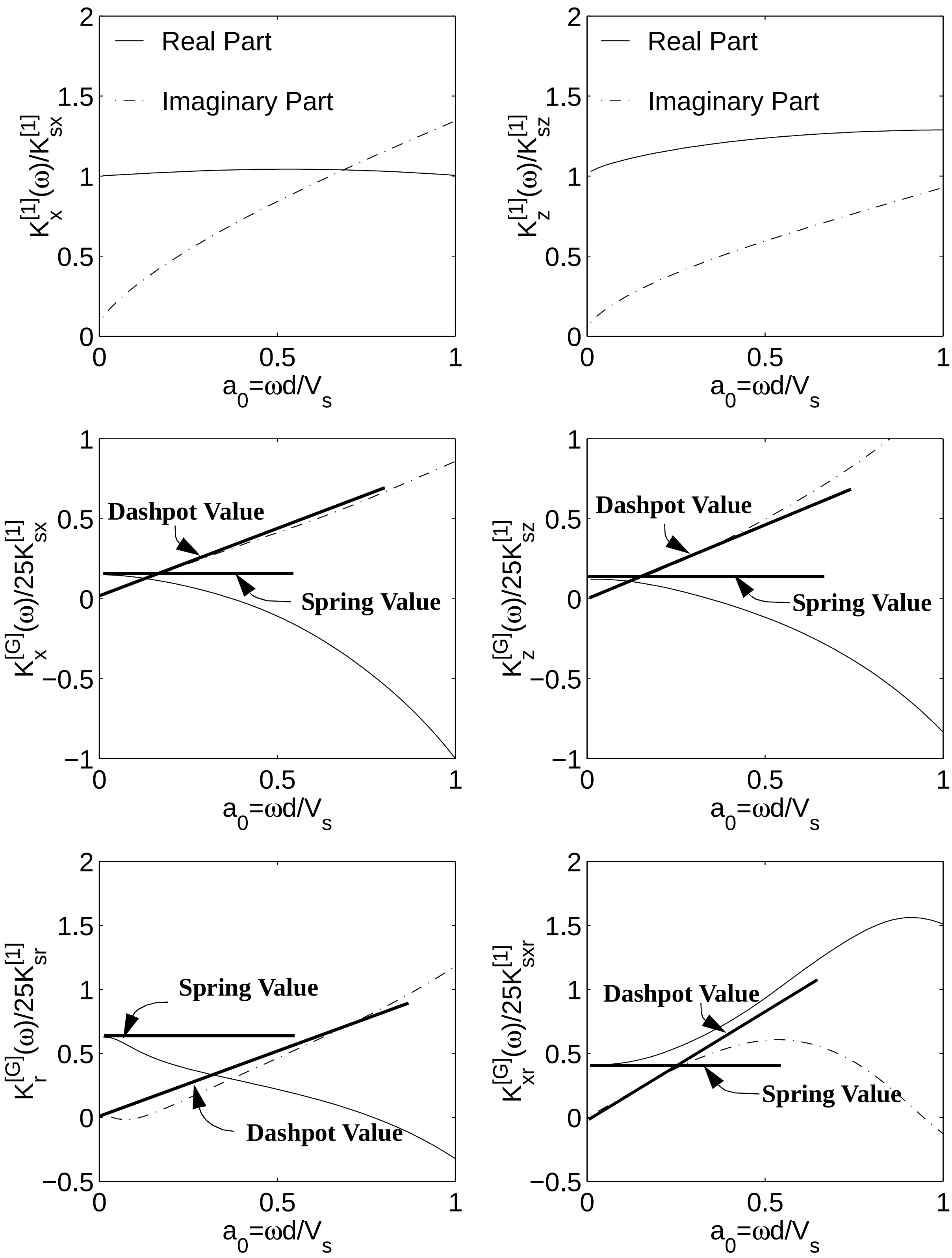

Figure 3.7. Dynamic stiffnesses of single pile and pile group at center bent of Meloland Road Overcrossing

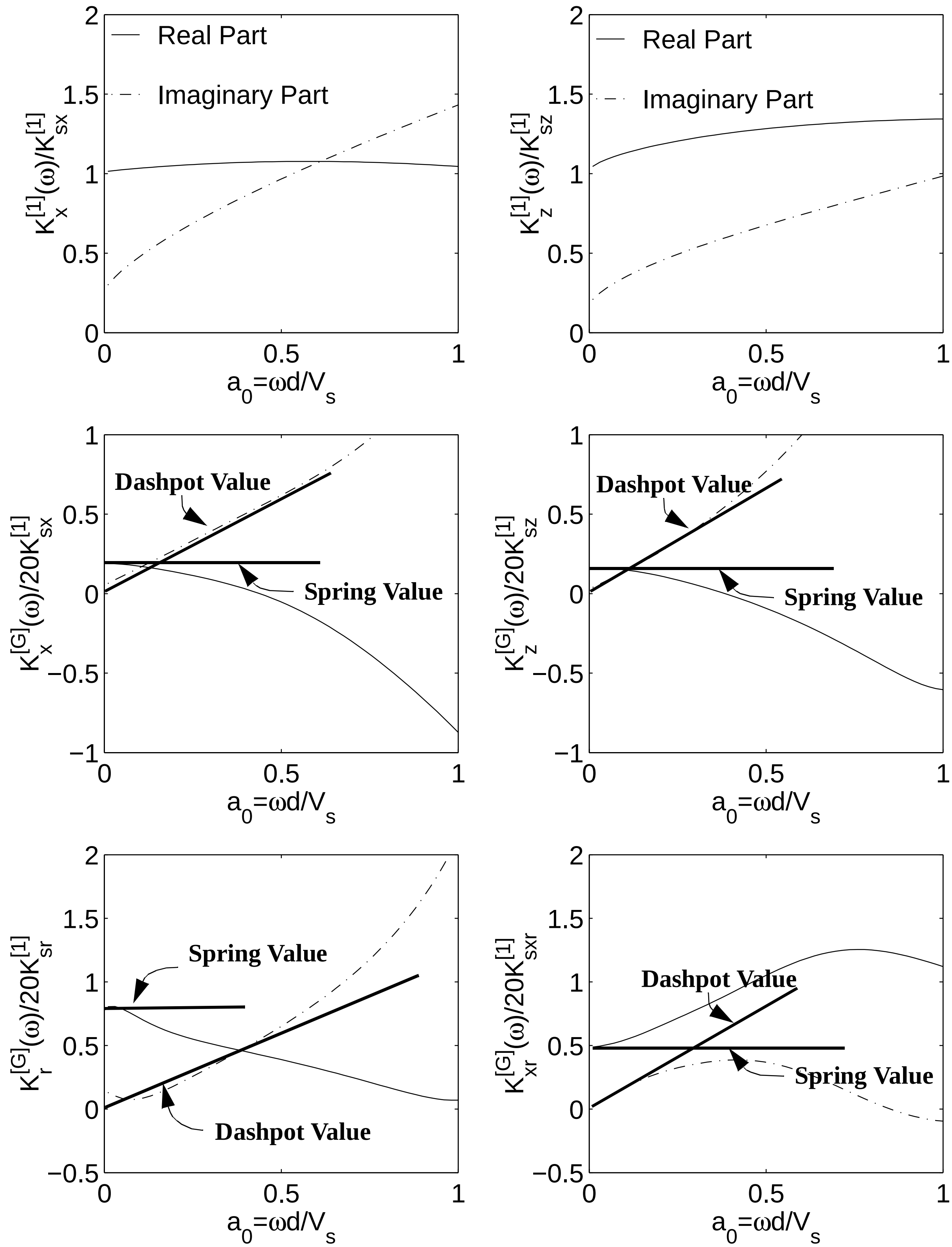

Figure 3.8. Dynamic stiffnesses of single pile and pile group at center bent of Painter Street Overcrossing

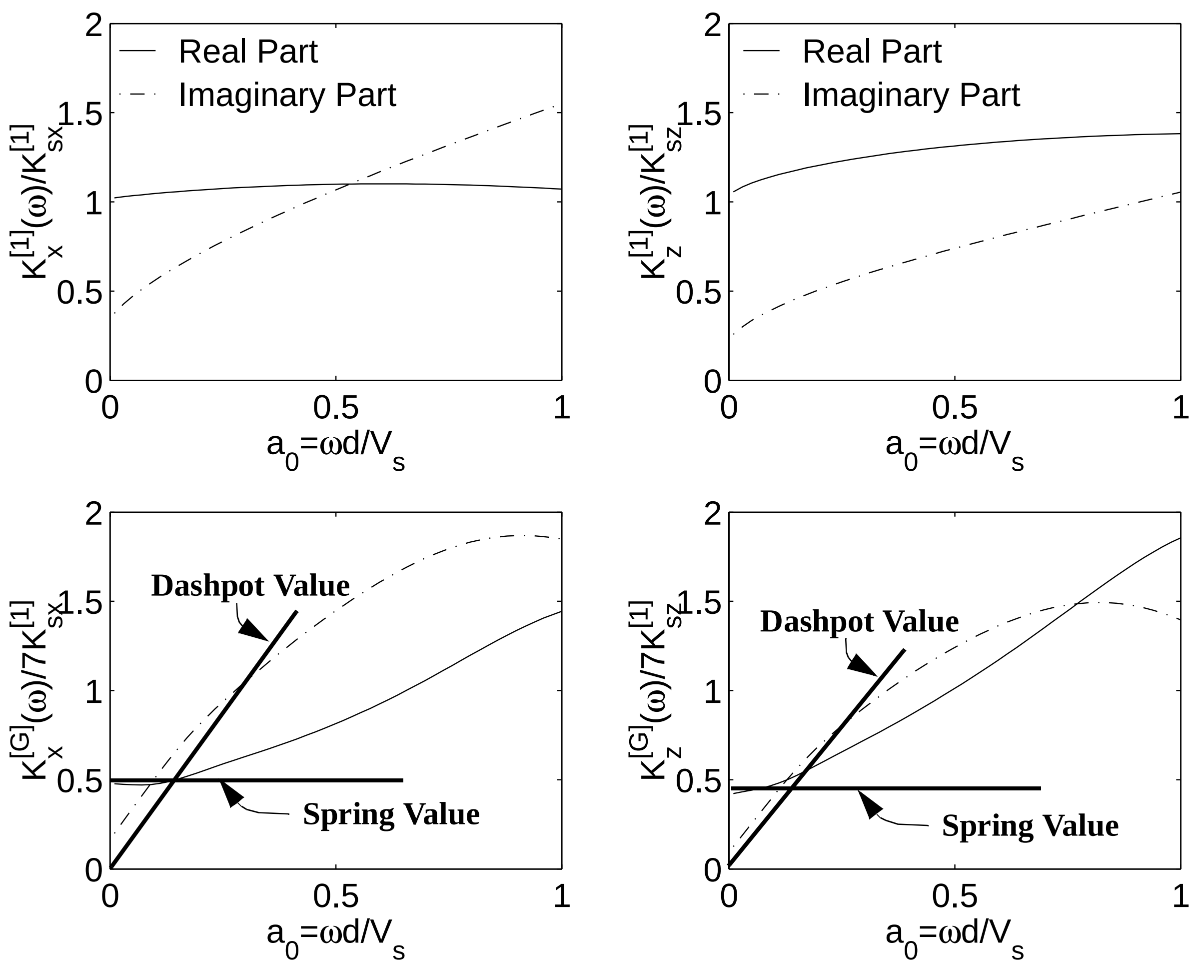

Figure 3.9. Dynamic stiffnesses of single pile and pile group at abutments of Meloland Road Overcrossing

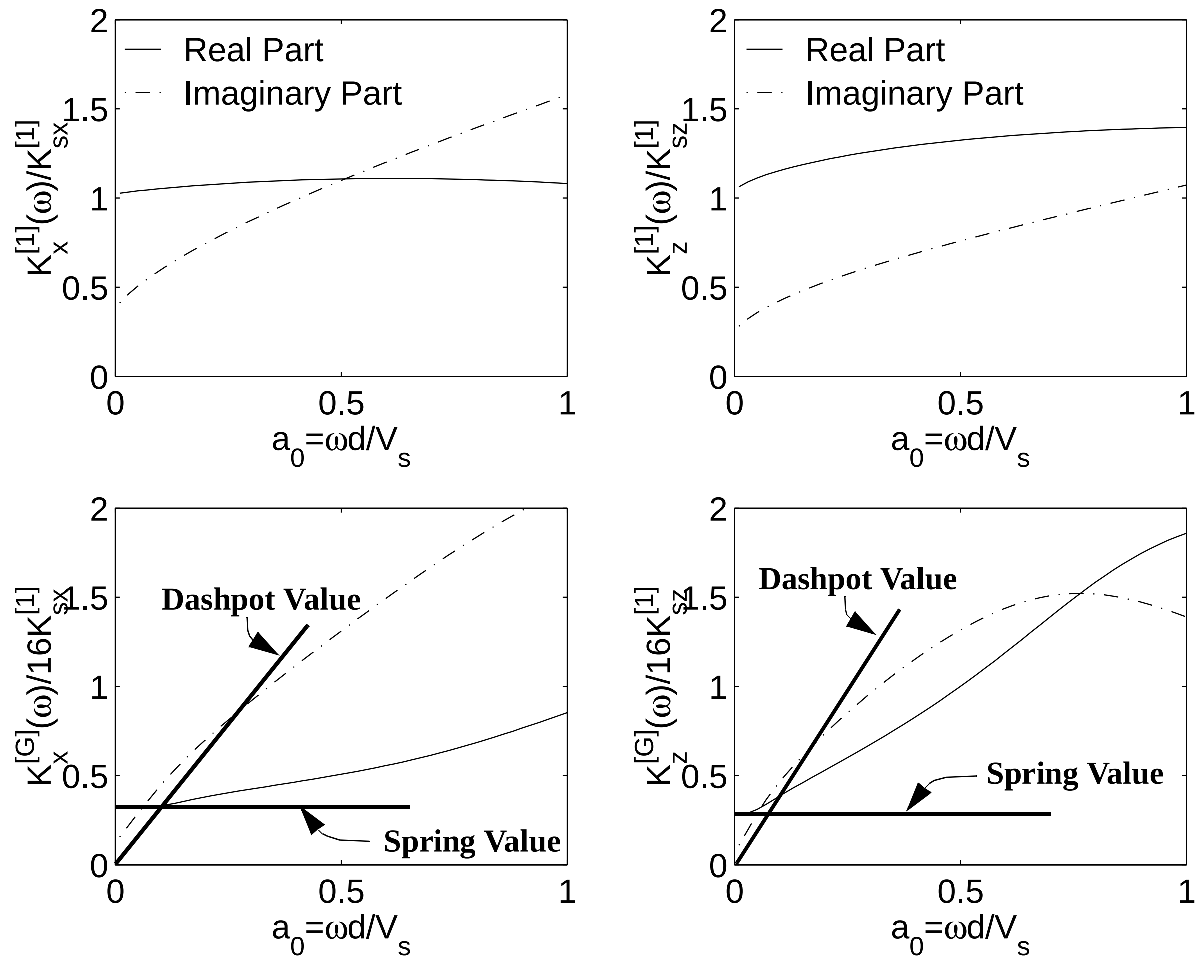

Figure 3.10. Dynamic stiffnesses of single pile and pile group at west abutment of Painter Street Overcrossing

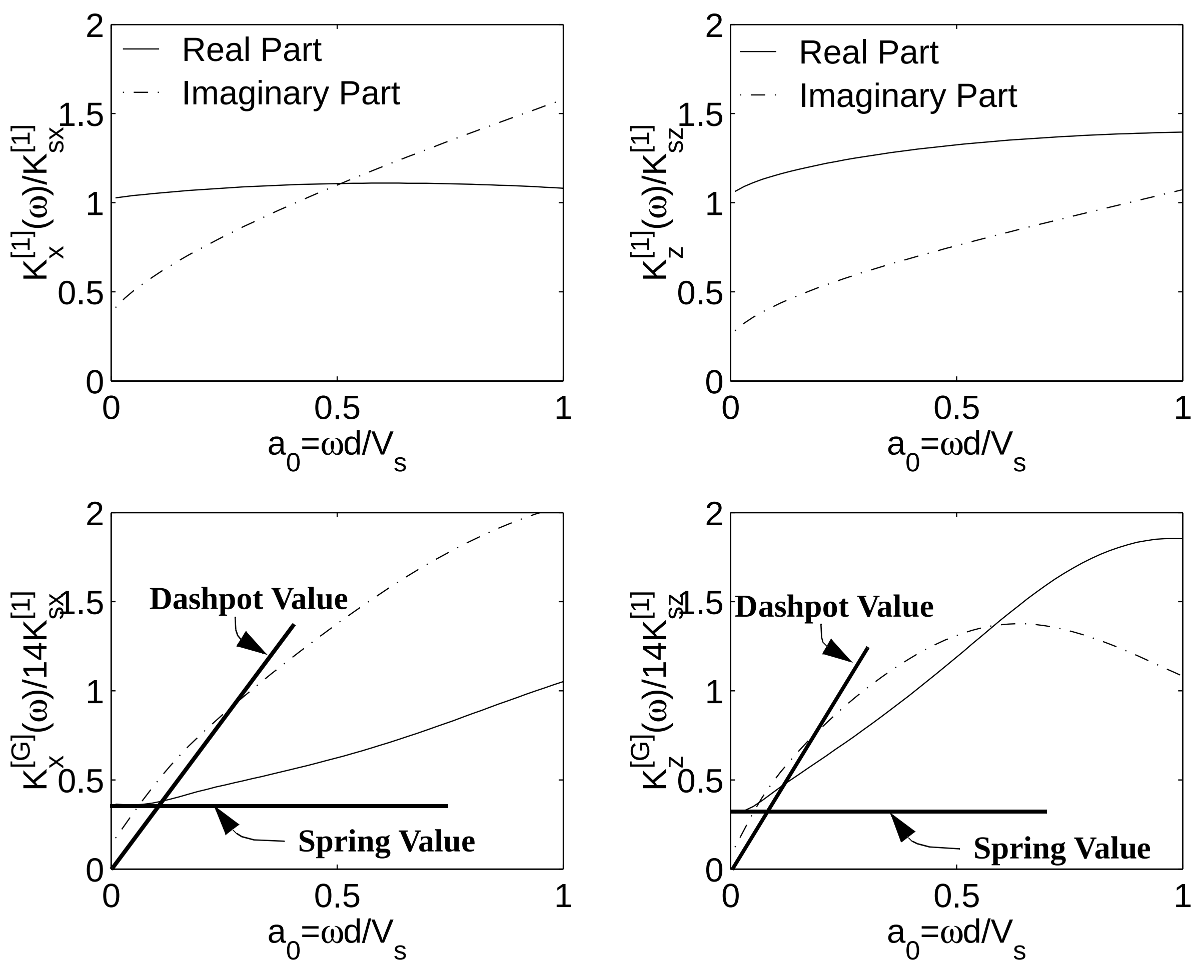

Figure 3.11. Dynamic stiffnesses of single pile and pile group at east abutment of Painter Street Overcrossing

TABLE 3. 1. The spring and dashpot values of the pile groups of interest

Parameters		Meloland Road Overcrossing	Painter Street Bridge
Pile Foundation at Abutments	$K_x, K_y\ (MN/m)$	56	180 (176)
	$K_z\ (MN/m)$	336	775 (762)
	$C_x, C_y\ (MN \cdot s/m)$	4.5	9.0 (8.6)
	$C_z\ (MN \cdot s/m)$	28.1	57.0 (54.5)
Pile Foundation at Center Bent	$K_x, K_y\ (MN/m)$	260	321
	$K_r\ (MN \cdot m/rad)$	7611	5254
	$K_{xr}, K_{yr}\ (MN/rad)$	-409	-354
	$K_z\ (MN/m)$	887	982
	$C_x, C_y\ (MN \cdot s/m)$	6.3	5.4
	$C_z\ (MN \cdot s/m)$	25.3	20.0
Note		Numbers in parentheses are for the east abutment of Painter Street Bridge	

3.4 EQUIVALENT FLEXURAL-SHEAR BEAM

In finite element analysis of the bridge system, the stiffnesses of the pile group should be included by an element whose stiffness matrix reads as

$$K^{[G]} = \begin{bmatrix} K_{1x}^{[G]} & K_{1xr}^{[G]} & 0 \\ K_{1xr}^{[G]} & K_{1r}^{[G]} & 0 \\ 0 & 0 & K_{1z}^{[G]} \end{bmatrix} \tag{3.40}$$

where $K_{1x}^{[G]}$, $K_{1z}^{[G]}$, $K_{1r}^{[G]}$, and $K_{1xr}^{[G]}$ are the real part of the static group stiffnesses obtained earlier. However, the cross-rocking term can not be modeled by adding a rotational spring or a displacement spring. To overcome this limitation a flexural-shear beam element is introduced. Its stiffness matrix takes the form (Ketter et al 1979):

$$K^b = \begin{bmatrix} k_{11} & k_{12} & 0 \\ k_{21} & k_{22} & 0 \\ 0 & 0 & k_{33} \end{bmatrix} \tag{3.41}$$

where

$$k_{11} = \frac{12GAEI}{L^3 GA + 12\lambda LEI} \tag{3.42}$$

$$k_{12} = \frac{-6GAEI}{L^2 GA + 12\lambda EI} = k_{21} \tag{3.43}$$

$$k_{22} = \frac{4(GAL^2 + 3\lambda EI)(EI)^2}{GAEIL^3 + 12\lambda L(EI)^2} \tag{3.44}$$

$$k_{33} = \frac{EA}{L} \tag{3.45}$$

and $\lambda = 1$ for a wide-flange cross section. By matching the stiffnesses of the equivalent beam element and those of the pile group, one can solve for beam length, L, cross-section area, A, moment of inertia, I, and shear modulus, G:

$$L = -2\frac{K_{1xr}^{[G]}}{K_{1x}^{[G]}} \tag{3.46}$$

$$A = -\frac{2}{E}\frac{K_{1z}^{[G]}K_{1xr}^{[G]}}{K_{1x}^{[G]}} \tag{3.47}$$

$$I = \frac{2}{E}K_{1xr}^{[G]}\left[\left(\frac{K_{1xr}^{[G]}}{K_{1x}^{[G]}}\right)^2 - \frac{K_{1r}^{[G]}}{K_{1x}^{[G]}}\right] \tag{3.48}$$

$$G = 3\lambda\frac{K_{1x}^{[G]}}{K_{1z}^{[G]}}\frac{(K_{1xr}^{[G]})^2 - K_{1r}^{[G]}K_{1x}^{[G]}}{4(K_{1xr}^{[G]})^2 - 3K_{1r}^{[G]}K_{1x}^{[G]}} \tag{3.49}$$

The expressions offered by (3.46) to (3.49) have been used in the finite element analysis presented in the next chapter.

3.5 SUMMARY OF PROCEDURE TO COMPUTE THE SPRING AND DASHPOT VALUES OF PILE FOUNDATIONS

1. Compute the transverse and vertical stiffnesses of single pile with equations (3.1), (3.18) and (3.21).
2. Compute the transverse, vertical, rocking and cross-rocking stiffnesses of pile groups with equations (3.33), (3.35), (3.36) and (3.38).
3. Select practical spring and dashpot values by passing a horizontal line through the graph of the real part and an inclined line through the graph of the imaginary part at locations that capture with satisfaction the low frequency behavior. In this study the spring value was selected equal to the static group stiffness.
4. When a stick model is used the pile foundation can be represented with a flexural-shear beam where its stiffness elements are given by equations (3.42) to (3.45).

4 Prediction of the Seismic Response of Highway Overcrossings

Once the kinematic response factors and dynamic stiffnesses of embankments and pile foundations have been established, the dynamic analysis of the bridge superstructure can be conducted with various models that offer different levels of sophistication. The most popular models are the reduced-order stick model and a detailed three-dimensional finite element model.

A comprehensive study that established the validity of the stick model was conducted by McCallen and Romstad (1994) who computed natural frequencies, mode shapes, and response time histories of the Painter Street Overcrossing using the two aforementioned numerical models. Both fixed and resilient foundation supports were considered and it was found that there is a one-to-one correspondence between the mode shapes predicted by the stick and the detailed finite element model. The McCallen and Romstad study indicated the substantial reduction in the transverse and longitudinal frequencies when realistic soil strains are considered; while in these two modes of vibration modal damping should be of the order of 20 to 30%. The levels of modal damping were concluded by McCallen and Romstad (1994) after a large number of trial and error iterations and comparisons of measured and computed responses at several bridge locations. The detailed finite element study by McCallen and Romstad (1994) that accounts for the resilience and dissipation at the center bent and end abutment involved the discretization of embankments and a large volume of the surrounding soil. Efforts to establish the validity of the stick model in estimating the seismic response of skew bridges have been also reported by Werner (1994).

4.1 RESPONSE OF THE MELOLAND ROAD OVERCROSSING

Figure 4.1 shows the stick model (top) and the three-dimensional finite element model (bottom) of the Meloland Road Overcrossing. The stick model is a collection of beam elements with cross-

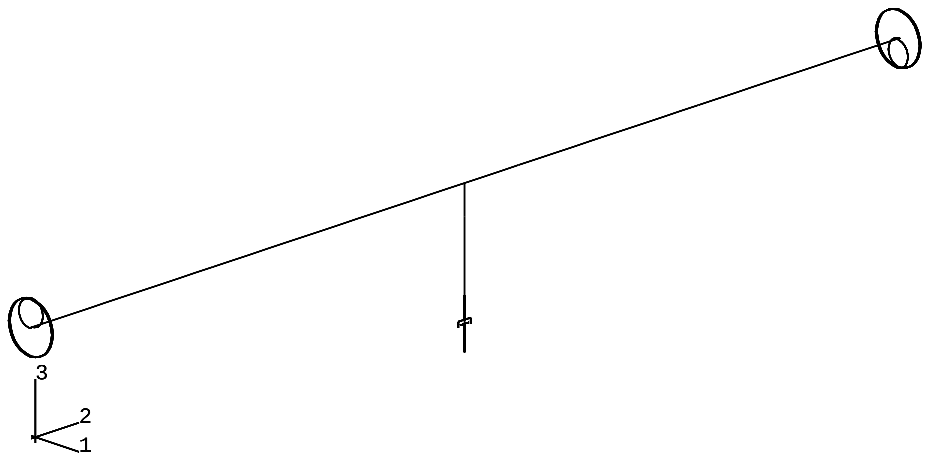

Stick Model

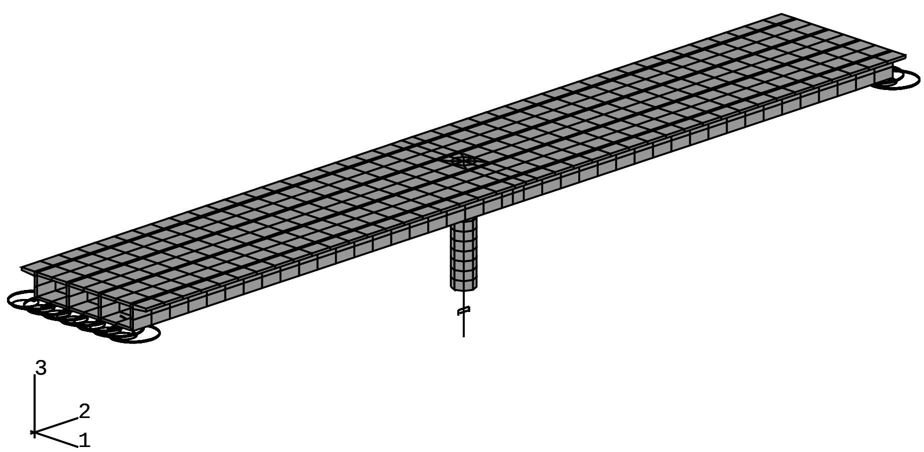

3D Finite Element Model

Figure 4.1 Numerical models of Meloland Road Overcrossing (Top: stick model; Bottom: 3-D finite element model) section properties adjusted from geometric data without considering any cracked section reduction. The three-dimensional finite element model uses eight-node solid elements for the bridge superstructure. The bridge superstructure is supported at its center bent and at each end by the springs and dashpots schematically shown in Figure 1.1, their values being estimated separately in Chapter 2 and 3 and summarized in Table 4.1.

TABLE 4.1. Spring and dashpot values that approximate the presence of the approach embankments and pile foundation of the Meloland Road Overcrossing. Values from this study are associated with the intensity of the 1979 Imperial Valley earthquake.

Parameters		1	2	3	4	5	6
Embankment + Pile Foundations	K_x (MN/m)	21+56	160*	91 (365)	107	/	607+49 (51+49)
	K_y (MN/m)	21+56	/	91 (365)	/	/	596+49
	K_z (MN/m)	78+356	418*	263 (1051)	/	/	/
	C_x $(MN \cdot s/m)$	1.5+4.5	/	/	/	/	/
	C_y $(MN \cdot s/m)$	1.5+4.5	/	/	/	/	/
	C_z $(MN \cdot s/m)$	3+28	/	/	/	/	/
Pile Foundation of Center Bent	K_x, K_y (MN/m)	260	/	254 (876)	/	1007	175
	K_r $(MN \cdot m/rad)$	7611	366	1888 (6509)	/	5696	/
	K_{xr}, K_{yr} (MN/rad)	-409	/	/	/	/	/
	K_z (MN/m)	887	/	550 (1898)	/	1460	/
	C_x, C_y $(MN \cdot s/m)$	6	/	/	/	/	/
	C_z $(MN \cdot s/m)$	25	/	/	/	/	/
Note	1. This study ($G = 2.0\ MPa$ and $\eta = 0.52$ for embankment soil) 2. Wilson and Tan 1990a (* embankment only, no piles and $G = 7.2\ MPa$ is used for embankment soil) 3. Douglas, Maragakis and Vrontinos 1991 (values in parenthesis are the optimal values identified from dynamic tests) 4. Werner 1994 (fixed boundary condition at the base of pier) 5. Maragakis, Douglas and Abdel-Ghaffar 1994 (values are from dynamic tests) 6. Caltrans: Method A (Method B)						

During the numerical simulation, the Young's modulus of the beam elements on top of the column was artificially increased by three orders of magnitude to form a rigid link in order to prevent excessive deflections at the connection point between pier and deck in the stick model, (McCallen and Romstad 1994). Vertical excitations are not considered. In both models, the damping of the bridge deck and center bent is approximated with the Rayleigh damping approximation, where the parameters α and β are computed by assuming a 5% modal damping ratio in the first and the second modes. The Young's modulus of the concrete is assumed to be $E_c = 22\ GPa$. This value is approximately 80% of the value obtained from empirical expressions to account for the cracking that occurred during the earthquake. Similar cracked values for the Young's modulus of concrete in seismic response analysis of bridges have been reported by Douglas and Reid (1982, $E_c = 20 \sim 25\ GPa$) and Dendrou et al. (1985, $E_c = 20\ GPa$). The density of concrete is assumed 2400 kg/m^3.

4.1.1 Eigenvalue Analysis

Eigensolutions were performed for the stick model and three-dimensional finite element model using the commercially available software ABAQUS. Figure 4.2 compares the first six modes and modal frequencies of the stick model and three-dimensional finite element model, and indicates a one-to-one correspondence between the two models. The natural frequencies of the stick model are also in good agreement with that of the three-dimensional finite element model.

While modal frequencies are directly estimated by solving the real eigenvalue problem of some structural idealization of the bridge-foundation system having mass matrix, $[M]$, and stiffness matrix, $[K]$, the estimation of the modal damping ratios appears to be a less straightforward procedure. The majority of modal damping ratios of bridges published in the literature have been back-figured by processing recorded data with system identification algorithms (Wilson 1986; Werner et al. 1987; Wilson and Tan 1990b; Werner 1994; and Goel 1997 among others). Although more recent multi-input-multi-output system identification algorithms appear to be more efficient than older single-input-single-output algorithms, the relevance of the reported values is strongly associated with the sophistication of the adopted structural model and the quality of the recorded data. In some occasions modal damping values appreciably larger than those identified were recommended (Werner 1994).

In an effort to calibrate finite element results, McCallen and Romstad (1994) initially assigned a uniform modal damping ratio, $\xi_j = 5\%$, to the first six modes of the Painter Street Overcrossing. Subsequently, after conducting a large number of trial and error iterations and comparisons of recorded and computed responses of the bridge, they reassigned much larger values of modal damping to selected modes in order to approximate satisfactorily the recorded responses.

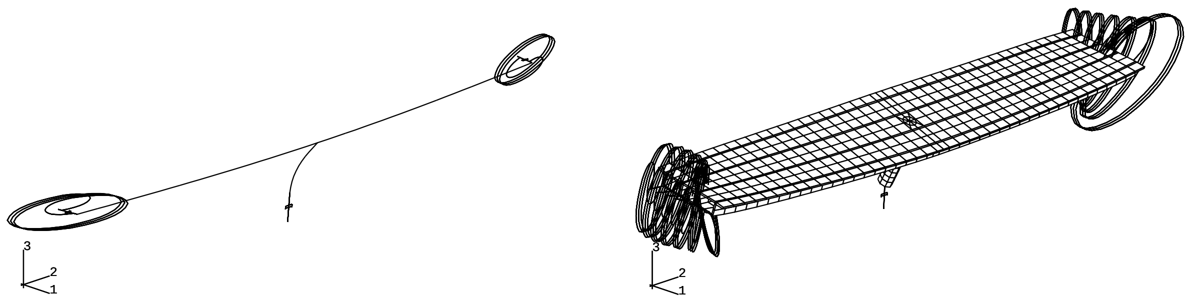

$f_1 = 2.01\ Hz$ $\xi_1 = 18.7\%$ $f_1 = 1.96\ Hz$

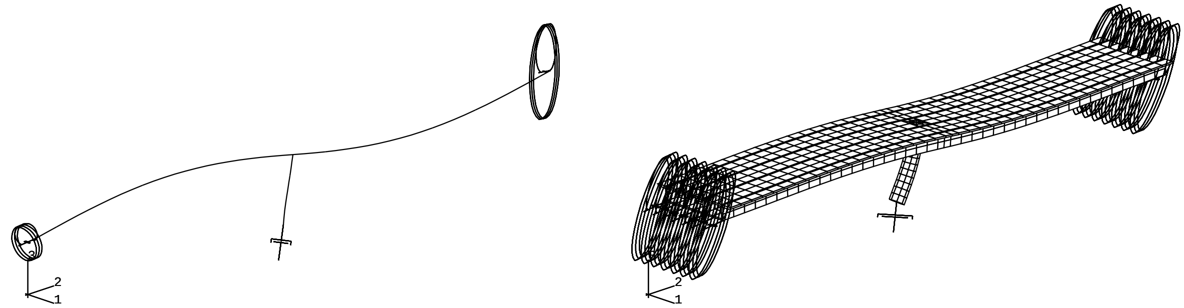

$f_2 = 2.85\ Hz$ $\xi_2 = 56.8\%$ $f_2 = 2.55\ Hz$

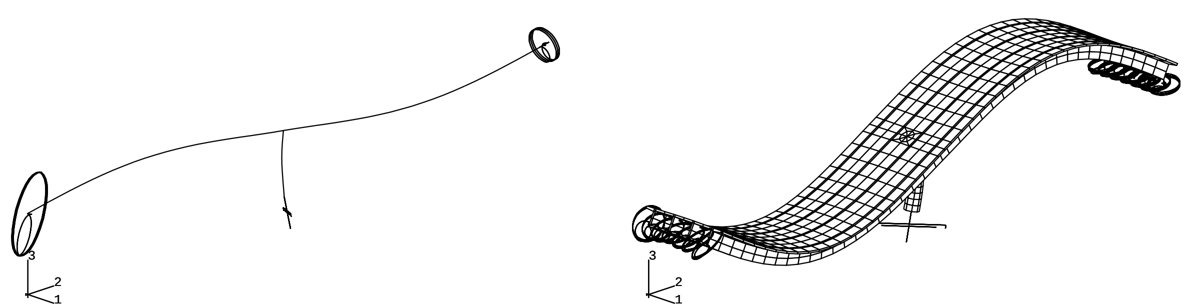

$f_3 = 3.58\ Hz$ $\xi_3 = 8.3\%$ $f_3 = 3.41\ Hz$

Figure 4.2. First six modal frequencies, damping ratios, and modes computed by stick model (left) and 3D FEM model (right) of Meloland Road Overcrossing (continued)

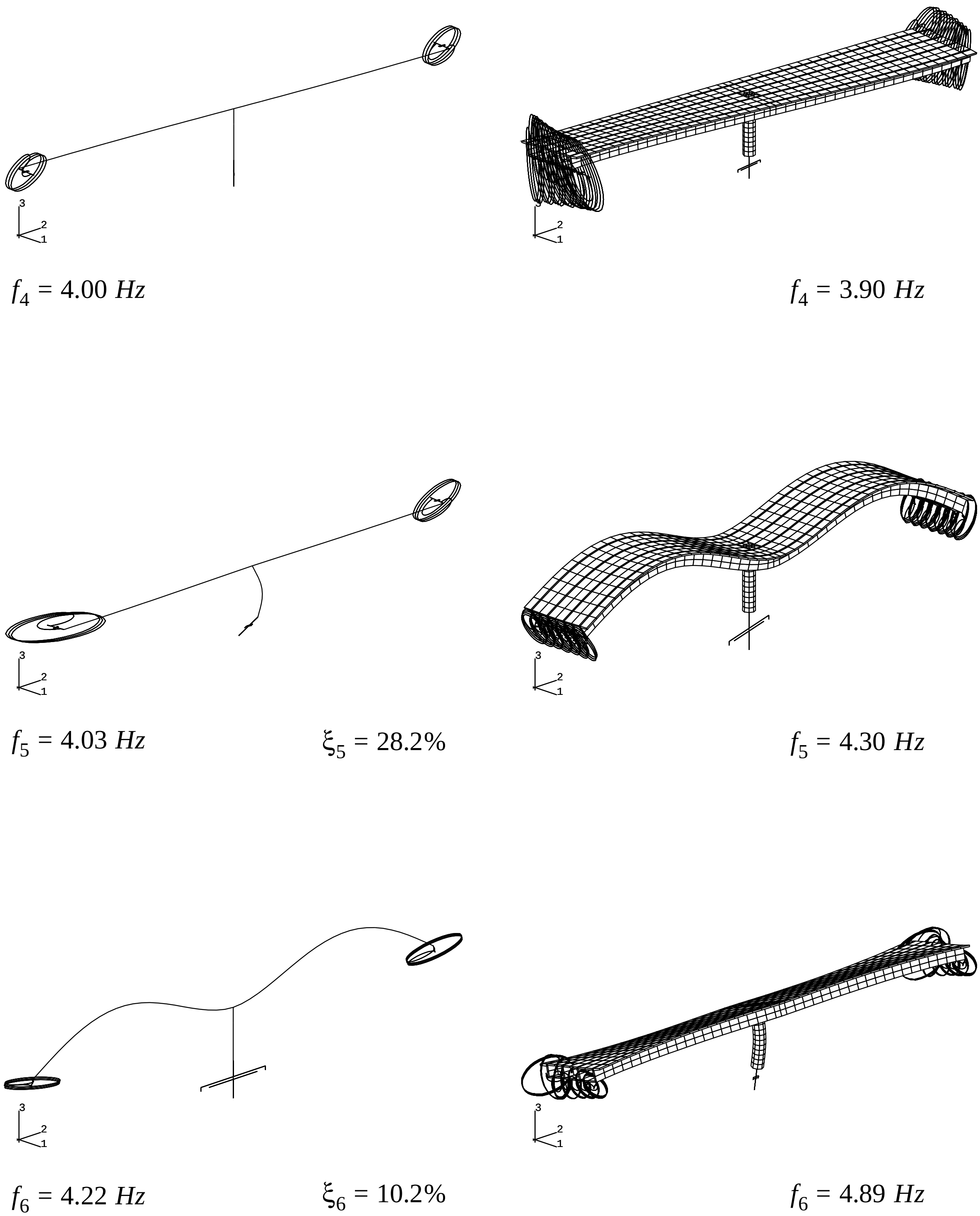

Figure 4.2. First six modal frequencies, damping ratios, and modes computed by stick model (left) and 3D FEM model (right) of Meloland Road Overcrossing

In this study the modal damping ratios of the bridge foundation system are computed by solving for the complex eigenvalues of the homogeneous equation

$$[M]\{\ddot{u}\} + [C]\{\dot{u}\} + [K]\{u\} = 0 \tag{4.1}$$

where $[M]$, $[C]$, and $[K]$ are the mass, damping, and stiffness matrices of the bridge-foundation idealization shown in Figure 1.1 and $\{u\}$ is the free vibration response vector

$$\{u\} = \{\phi\}e^{i\Omega t} \tag{4.2}$$

In equation (4.2), Ω is the complex characteristic value and $\{\phi\}$ is the associated characteristic vector. This complex eigenvalue approach is well known in the literature and was given a critical review by Veletsos and Ventura (1986). The damping matrix, $[C]$, is constructed by adopting the concept of Rayleigh damping for the bridge superstructure and appending the pre-identified lumped dashpots at the locations where the superstructure interacts with its foundation. Following this approach we assign a 5% modal damping ratio at the first and second modes of the undamped idealized model (bridge deck with springs) and add the damping constants, c_{ij}, identified in chapters 2 and 3 that represent the presence of the embankments and pile foundations. With this superposition the nonclassical damping matrix, $[C]$, of the bridge-foundation system assumes the form

$$[C] = \alpha[M] + \beta[K] + [c_{ij}] \tag{4.3}$$

The matrix $[c_{ij}]$ is assembled in the same way as the stiffness matrix $[K]$ of the undamped superstructure so that the lumped dashpots c_{ij} are assigned to the correct degrees of freedom. Substitution of (4.2) in (4.1) yields

$$(-\Omega^2[M] + i\Omega[C] + [K])\{\phi\} = 0 \tag{4.4}$$

which is a standard polynomial eigenvalue problem. The roots of this polynomial are the complex characteristic values Ω_j that were evaluated with MATLAB (1997). The relation between Ω_j with the modal frequencies, ω_j, and modal damping ratios, ξ_j ($j = 1, 2, ...\mathrm{N}$) is determined from the associated equation of a single-degree-of-freedom oscillator. Interpreting Ω_j as the frequency domain parameter one may determine

$$\Omega_j = \pm\sqrt{\omega_j^2 - \xi_j^2\omega_j^2} + i\xi_j\omega_j \tag{4.5}$$

After solving for ω_j and ξ_j,

$$\omega_j = \sqrt{\Omega_{jR}^2 + \Omega_{jI}^2} \tag{4.6}$$

$$\xi_j = \frac{\Omega_{jI}}{\omega_j} \tag{4.7}$$

in which Ω_{jR} and Ω_{jI} are the real and imaginary parts of the characteristic value Ω_j, respectively.

The stick model used in the real eigenvalue analysis consists of 354 degrees of freedom for Meloland Road Overcrossing. In order to bypass the problem of computing and interpreting the complex eigenvalues of such large matrices, a reduced-order stick model was developed with fewer degrees of freedom. Sensitivity studies indicated that the modal characteristics of the first ten modes are virtually insensitive to the exact number of elements of the reduced-order stick model. Two reduced-order stick models that consist of 228 and 300 degrees of freedom (d.o.f) respectively yield nearly identical results as indicated in Table 4.2.

Table 4.2 presents the first six real eigenvalues of the Meloland Road Overcrossing that have been computed with the 3D finite element model of the undamped bridge (column A), the original stick model of the undamped bridge (column B, d.o.f=354), the reduced-order stick model of the undamped bridge (column C, d.o.f=300 and 228 respectively), and the first six complex eigenvalues of the reduced-order stick model of the damped bridge (column D, d.o.f=300 and 228 respectively). The corresponding damping ratios computed with this study are shown in column 1, next to other values reported in the literature.

The values shown in Table 4.2 indicate that the reduced-order stick model in association with the complex eigenvalue analysis yield valuable information on the free vibration characteristics of the bridge.

- The computed modal damping ratios, ξ_j, are much larger than the 5% modal damping assumed by Caltrans.
- The computed first modal damping ratio, $\xi_1 = 18.7\%$, which in this case corresponds to the first transverse mode with the deck bending away from the undeformed configuration, is in agreement with the low end of damping values along the transverse mode that are reported by Werner (1994). The values of first modal damping reported by Werner (1994) are appreciably larger than the value by the same and other investigators during earlier studies on the same bridge (Werner et al. 1987).
- The computed second modal damping $\xi_2 = 56.8\%$ is unusually high. However, our confidence in this value originates from the straight configuration of the deck and its integral abutments which are mobilizing a large volume of soil with high damping. Indirect evidence that this high damping value might be realistic is provided by the inability of system identification studies to detect modal characteristics along the longitudinal mode of vibration.

TABLE 4.2. Modal frequencies, ω_j (rad/s), and damping ratios, ξ_j (%), of Meloland Road Overcrossing

Modes	Eigenvalues (rad/s)				1		2		3		4	5	
	Model A	Model B	Model C	Model D	ω_j	ξ_j	ω_j	ξ_j	ω_j	ξ_j	ω_j	ω_j	ξ_j
1st transverse	12.320	12.647	12.440 (12.441)	13.519 + 2.5771i (13.702 + 2.7333i)	13.8 (13.8)	18.7 (18.7)	15.5	7.2	14.3~15.7	6.6~12.7	15.6	16.3	19~26
longitudinal	16.044	17.913	17.882 (17.884)	16.001 + 11.047i (16.221 + 11.104i)	19.4 (19.4)	56.8 (56.8)					16.7		
1st vertical (antisymmetric)	21.405	22.460	21.911 (21.921)	21.073 + 1.746i (21.252 + 1.888i)	21.1 (21.2)	8.3 (8.3)					17.5		
torsion about vertical axis	24.521	25.105	23.823 (23.824)	0.0 + 17.942i (0.0 + 17.962i)	17.9 (18.0)	100 (100)	Critically Damped Mode						
2nd transverse/torsion about longitudinal axis	26.996	25.340	25.096 (25.087)	25.778 + 7.570i (26.830 + 8.010i)	26.9 (26.9)	28.2 (28.2)							
2nd vertical (symmetric)	30.724	26.515	26.496 (26.526)	28.153 + 2.895i (28.187 + 2.900i)	28.3 (28.3)	10.2 (10.2)	28.7	5.8	27.4~29.9	3.1~7.4	27.6		
Note	A: Undamped original 3D FEM model B: Undamped original stick model C: Undamped reduced stick model with 300 d.o.f and (228 d.o.f) respectively D: Damped reduced stick model with 300 d.o.f and (228 d.o.f) respectively 1: This study 2: Werner, Beck, and Levine 1987; 3: Wilson & Tan 1990b 4: Gates 1993 5: Werner 1994												

- The modal damping associated with the third mode (1st vertical, antisymmetric, $\xi_3 = 8.3\%$) is lower than the modal damping associated with the transverse and the longitudinal modes that involve more soil participation.
- The torsional mode about the vertical axis is critically damped. Since the modes are decoupled the modal damping of the torsional mode can be estimated by assuming that the deck is a single-degree-of-freedom structure with length, L, and linear mass density, m, that rotates about the center bent and its motion is resisted at the two ends by the transverse springs and dashpots of the embankments indicated in Table 4.1. With this idealization, the equation of motion for torsion about the vertical axis is

$$I_0\ddot{\theta} + \frac{1}{2}C_x L^2\dot{\theta} + \frac{1}{2}K_x L^2\theta = 0 \tag{4.8}$$

  where $I_0 = \frac{1}{12}mL^3$ is the moment of inertia of the deck about the vertical axis. Using the standard real valued procedure (Chopra 1995) or the complex formulation given by equations (4.6) and (4.7) one concludes that $\omega_5 = \sqrt{\frac{6K_x}{mL}} \approx 26.2\ rad/s$ and $\xi_5 = (3C_x)/(\sqrt{6K_x mL}) \approx 1.0$.
- The computed fifth modal damping $\xi_5 = 28.6\%$ also assumes a high value, probably due to the explanation offered above, since this mode involves the transverse motion of the deck as well as torsional motion of deck about the longitudinal axis.
- The good agreement between the values reported for the first and sixth natural frequencies of the MRO by various investigators is worth mentioning.

Figure 4.3 shows Fourier amplitude spectra of channels 7, 8, 9, and 13, which are located on the bridge deck and indicated in Figure 2.9. The solid lines indicate the first natural frequencies predicted by the stick model and 3D FEM model (1.96Hz~2.01Hz), while the dashed lines indicate the range of identified fundamental frequencies (2.28Hz~2.57Hz) that have been reported in literature (Werner et al. 1987; Wilson and Tan 1990b; Gates 1993; excitation: the1979 Imperial Valley earthquake). The spectrum shows an appreciable power concentration at a even lower frequency (0.5 Hz) which has not been identified from any studies. This might be related to a malfunction of the recording instruments (Werner et al. 1987). The data used in this study are reconstructed histories that have been provided by the California Division of Mines and Geologies.

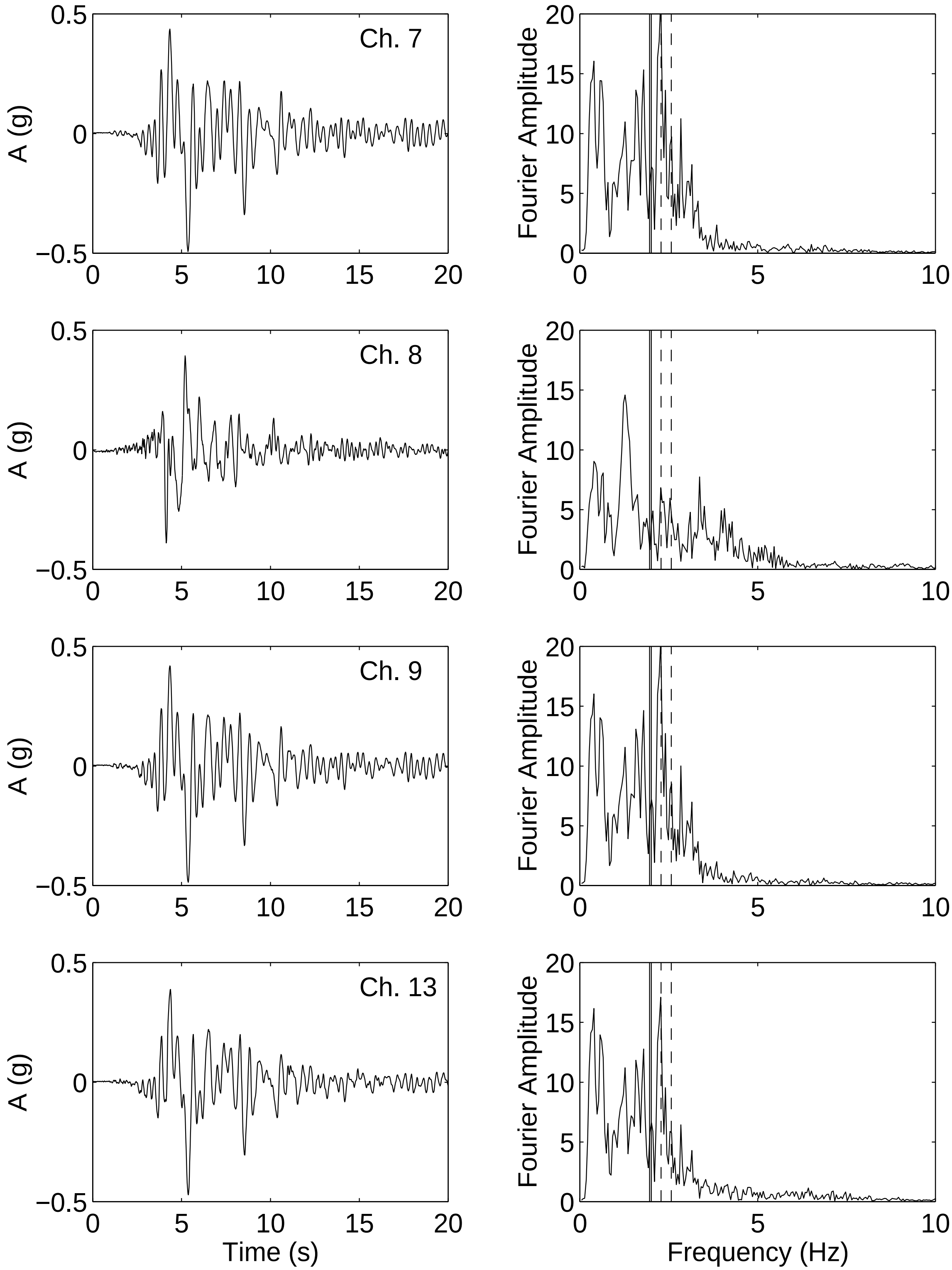

Figure 4.3. Fourier amplitude spectra of accelerations recorded at channels 7, 8, 9, and 13 of Meloland Road Overcrossing

4.1.2 Time History Analysis

Figures 4.4 to 4.7 plot total acceleration, relative velocity, and displacement time histories of the bridge response at selected locations. The analysis shown in these figures investigates the sensitivity of the bridge response to the support motion. The first column shows the recorded motions. The second column shows computed response quantities by using as a support motion at the end abutments the crest motions computed using Equation (2.14). The third column shows the computed response quantities by using as a support motion at the center bent and the end abutments the free-field motion. The last column shows computed response quantities by using as a support motion at the end abutments the recorded crest motions. All simulated responses are obtained by implementing the spring and dashpot values that have been evaluated with the approximate methods advanced in Chapters 2 and 3.

Figure 4.4 compares the computed response with the records of channel 7, which is located at mid-span of the bridge deck. The case where the recorded crest motions is used as support motions yields the best overall predictions. The acceleration and the deck drift are predicted with errors less than 8%, while the relative velocity is underestimated by 26%. When the computed crest motions are used as support motions, the peak acceleration is overestimated by 27% while the deck drift and the relative velocity is predicted with marginal discrepancies. Figure 4.5 compares the computed response with the records of channel 8. When the free-field motions are used as support motions the discrepancies between records and predictions are of the order of 70% or more for relative velocities and relative displacements. Similar trends can be observed in Figures 4.6 and 4.7, which compare the computed responses with the records of channels 9 and 13. The results shown in Figures 4.4 to 4.7 indicate the significance of considering the amplified support motions at the crest of the embankments.

Our parametric analysis proceeds by analyzing the bridge response when different support idealizations are considered. Figure 4.8 shows three idealizations of interest: (a) monolithic abutments and viscoelastic foundation at the center bent, (b) viscoelastic embankments and monolithic support at the center bent, and (c) viscoelastic embankments and elastic support at the center bent. The sensitivity of the bridge responses to the resilience and dissipation of the bridge supports is investigated in Figures 4.9 and 4.10, which compare the response quantities against the records of channels 7 and 9. The first column in Figures 4.9 and 4.10 shows the recorded motions. The second column shows computed response quantities by assuming monolithic abutments and

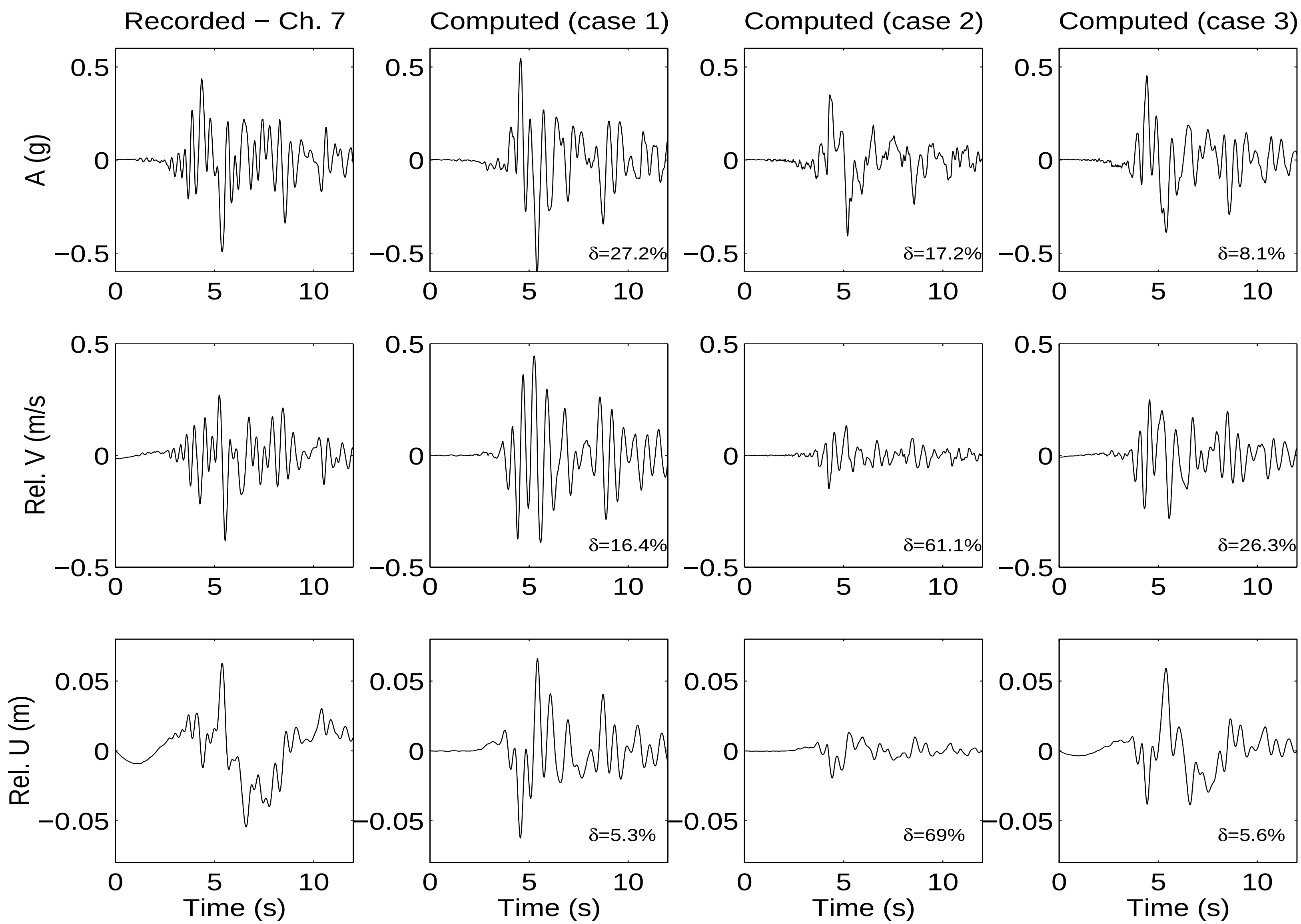

Figure 4.4. Records of channel 7 and predictions of Meloland Road Overcrossing response considering different support motions

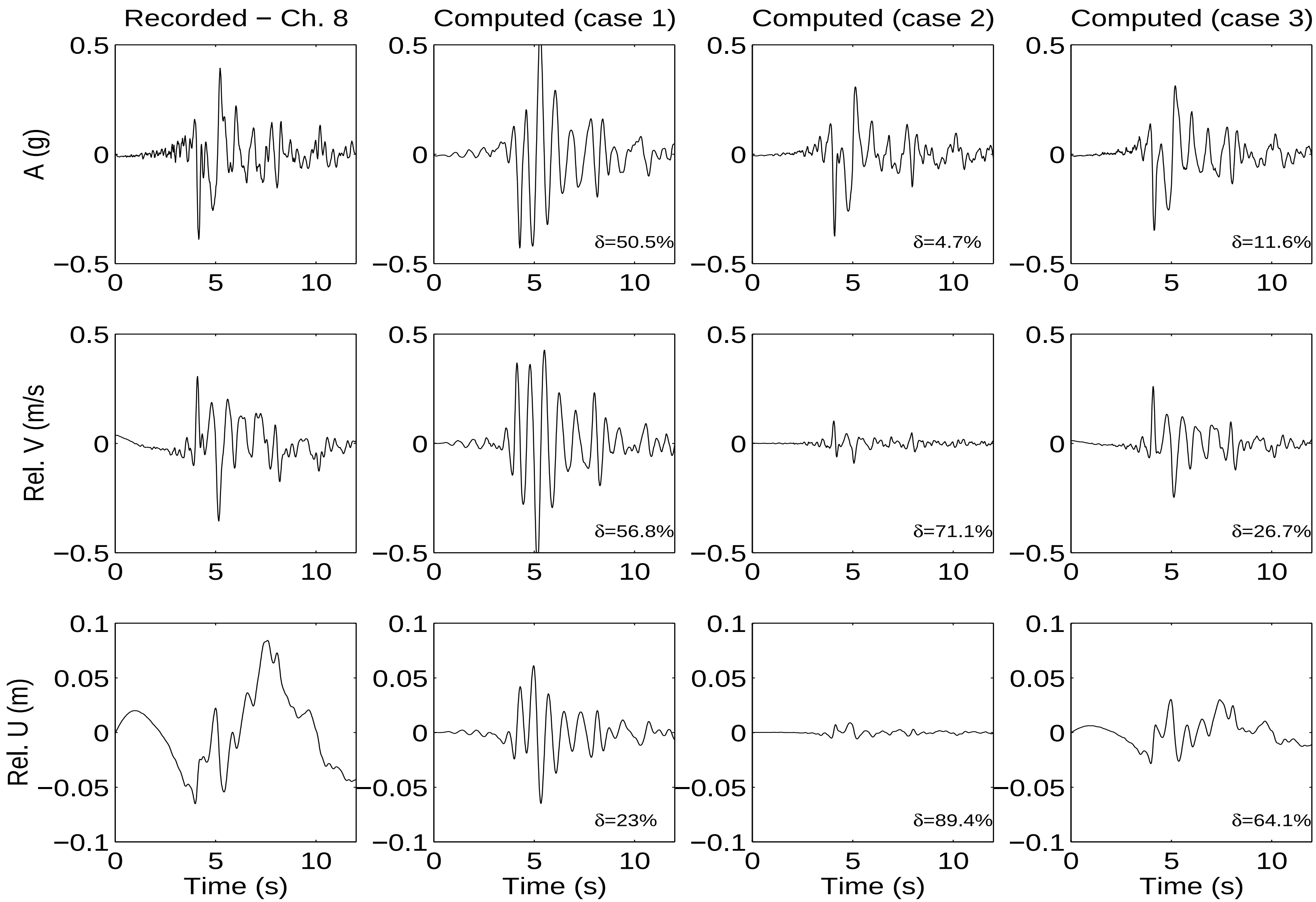

Figure 4.5. Records of channel 8 and predictions of Meloland Road Overcrossing response considering different support motions

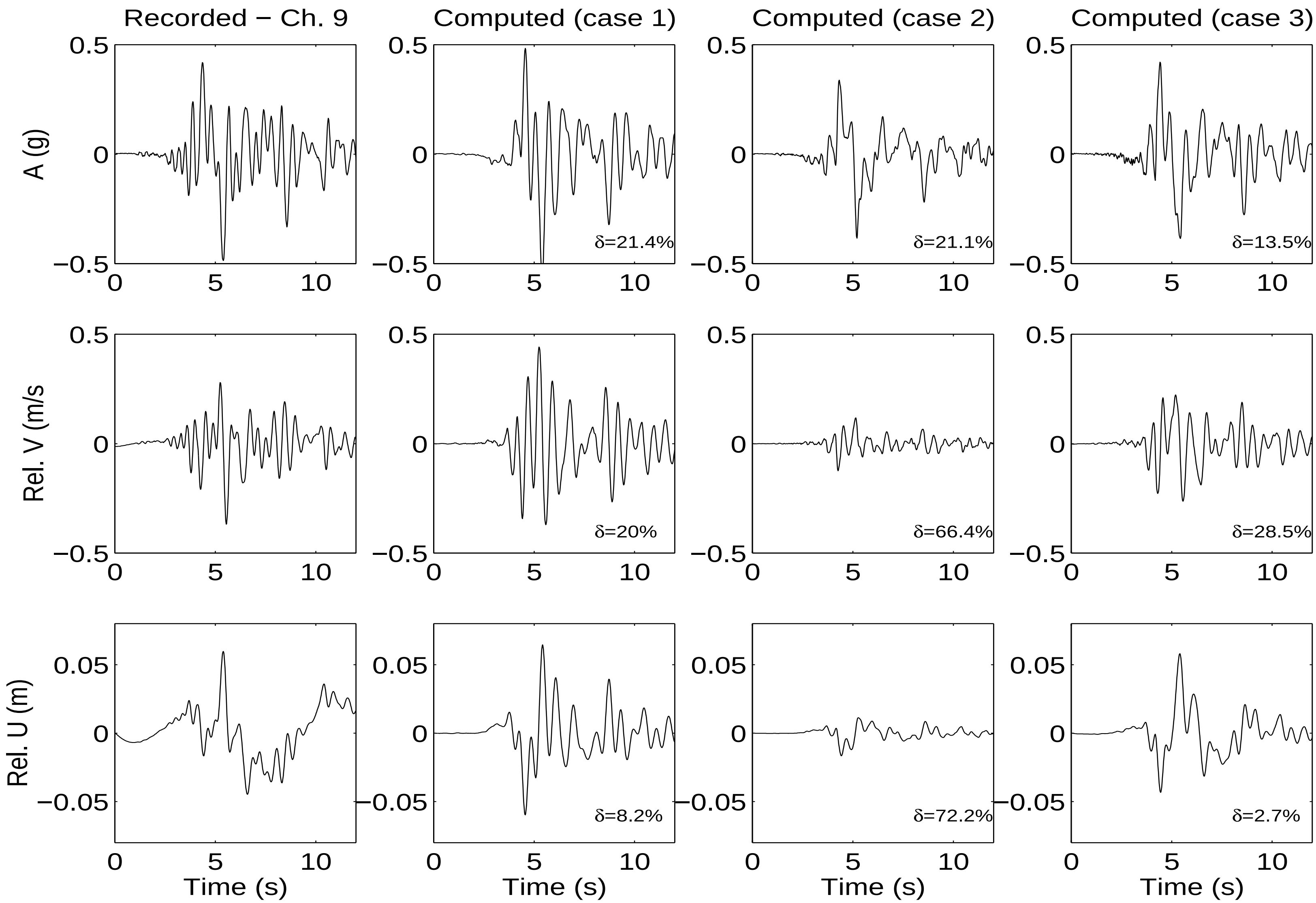

Figure 4.6. Records of channel 9 and predictions of Meloland Road Overcrossing response considering different support motions.

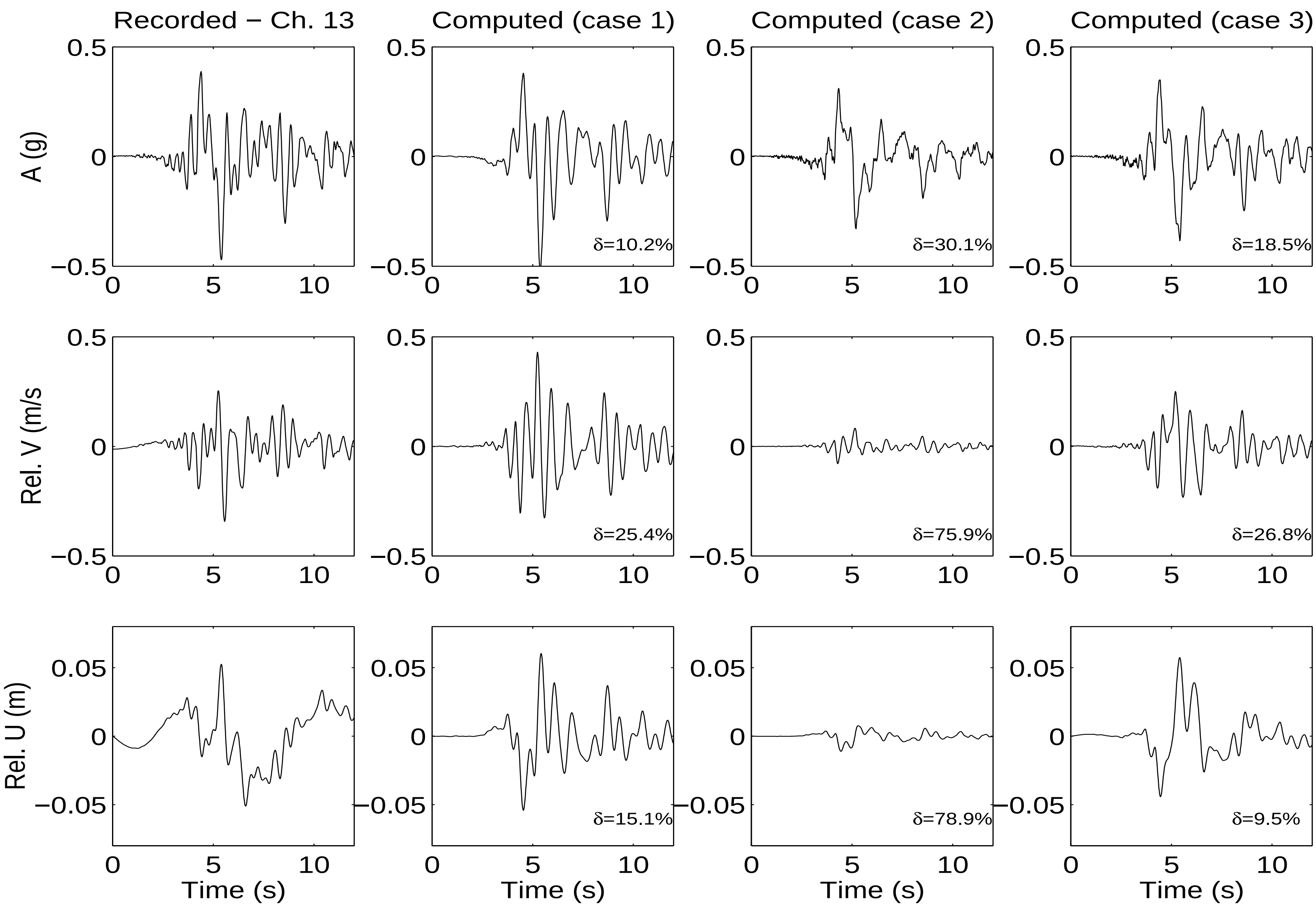

Figure 4.7. Records of channel 13 and predictions of Meloland Road Overcrossing response considering different support motions

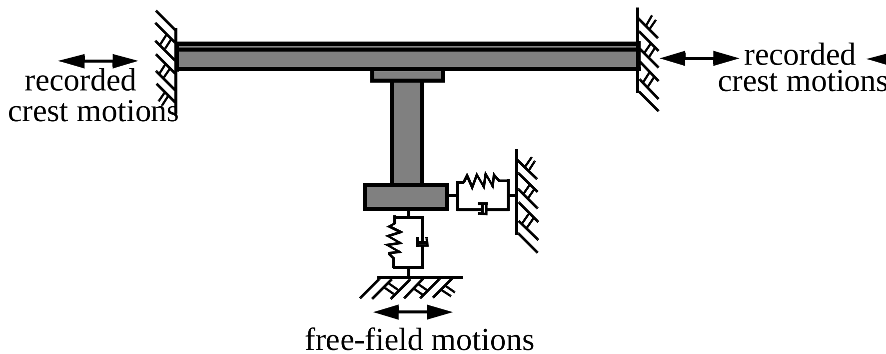

(a) Monolithic embankments and viscoelastic foundation at the center bent

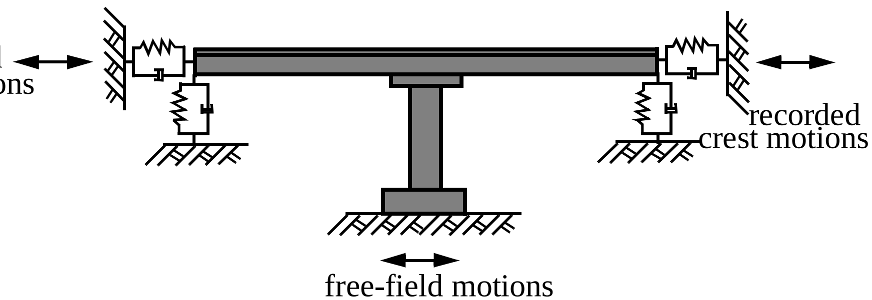

(b) Viscoelastic embankments and monolithic support at the center bent

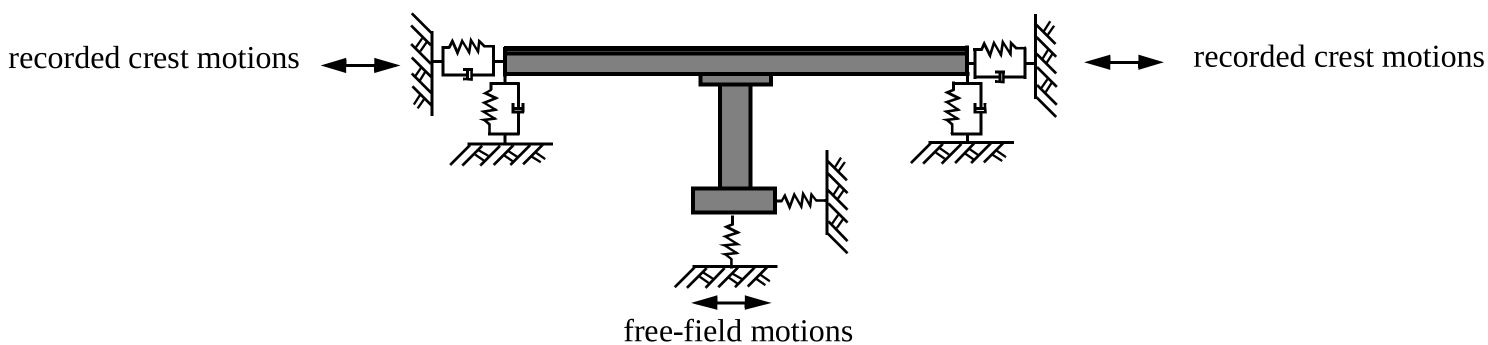

(c) Viscoelastic embankments and elastic support at the center bent

Figure 4.8 Bridge models with different support idealizations

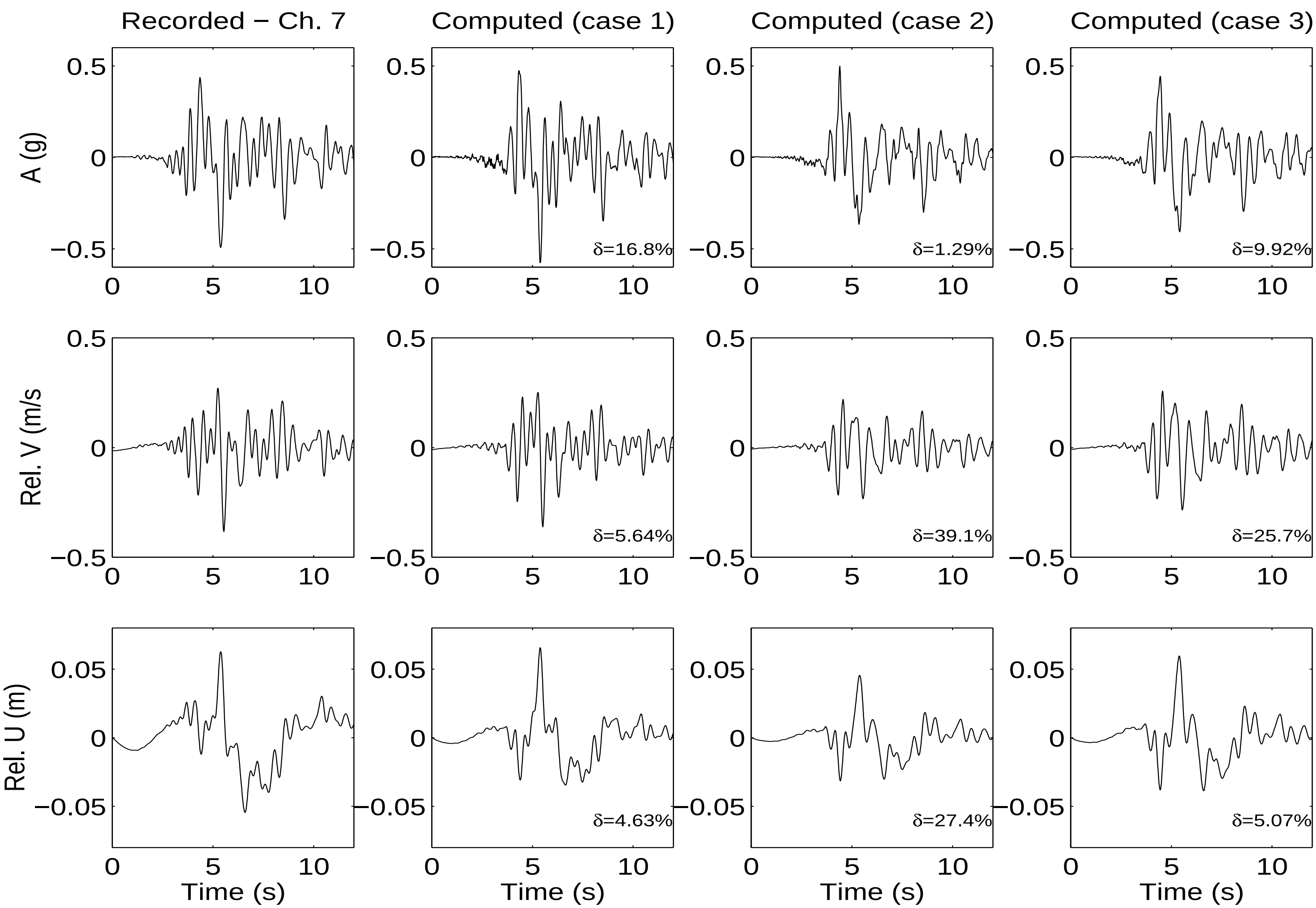

Figure 4.9. Records of channel 7 and predictions of Meloland Road Overcrossing response considering different support idealizations

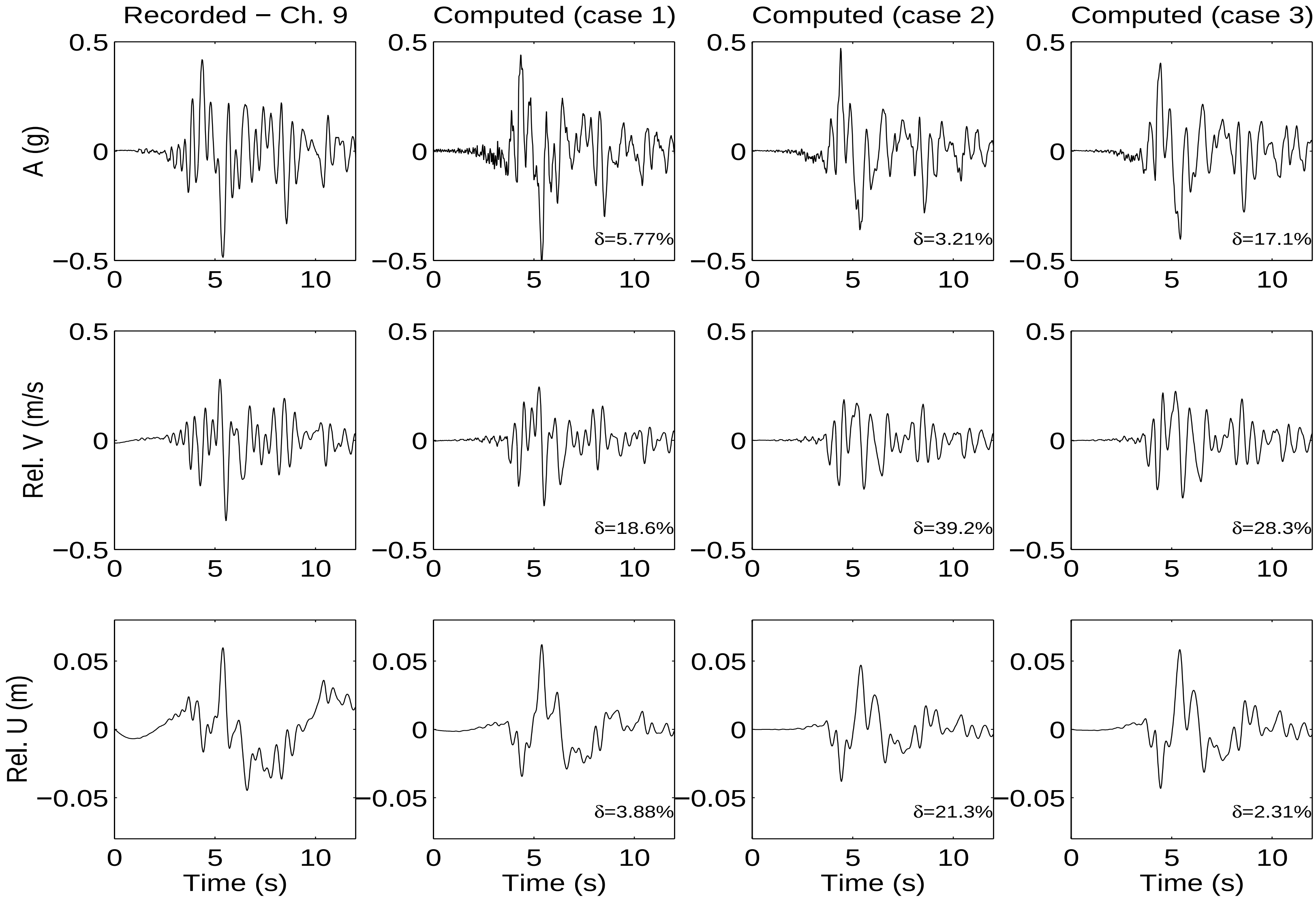

Figure 4.10. Records of channel 9 and predictions of Meloland Road Overcrossing response considering different support idealizations

viscoelastic foundation at the center bent. It examines the effect of neglecting the resilience and dissipation at the abutments. The third column examines the effect of neglecting the resilience and dissipation of the pile foundation at the center bent. The last column examines the effect of neglecting the dissipation of the pile foundation at the center bent. All simulated response are subjected to the recorded motions at the crest of the embenkment and the freefield and should be compared with the last column of Figures 4.4 and 4.6. The case of a rigid support at the center bent results in the smaller drifts, while the case of neglecting the dissipation of the pile foundations (Goel and Chopra 1997) yields comparable results when it is included.

4.2 RESPONSE OF THE PAINTER STREET OVERCROSSING

Figure 4.11 shows the stick model (top) and three-dimensional finite element model (bottom) of the Painter Street Overcrossing. Again, the stick model is a collection of beam elements with cross-section properties adjusted from geometric data without considering any cracked section reduction. While it is not shown in Figure 4.11 the beam elements are joined following the skew configuration of the bridge that results in coupling of the vibration modes. The three-dimensional finite element model uses eight-node solid elements for the bridge structure. The bridge superstructure is supported at its center bent and both ends by the springs and dashpots schematically shown in Figure 1.1 — their values being estimated separately in the chapters 2 and 3 and summarized in Table 4.3 (column 1), along with selected values reported in literature (columns 2 to 5).

Vertical excitations are not included during the analysis. In both models, the damping of the bridge superstructure is approximated with the Rayleigh damping approximation, where the parameters α and β are computed by assuming a 5% modal damping ratio in the first and the second modes. The Young's modulus of the concrete is assumed to be 22GPa. This value is approximately 80% of the value obtained from empirical expressions to account for the cracking that occurred during the earthquake. The density of concrete is $2400\ kg/m^3$.

4.2.1 Eigenvalue Analysis

Eigensolutions were performed for the stick model and three-dimensional finite element model using the commercially available software ABAQUS. Figure 4.12 compares the first six natural modes and frequencies of the stick model and the three-dimensional finite element model.

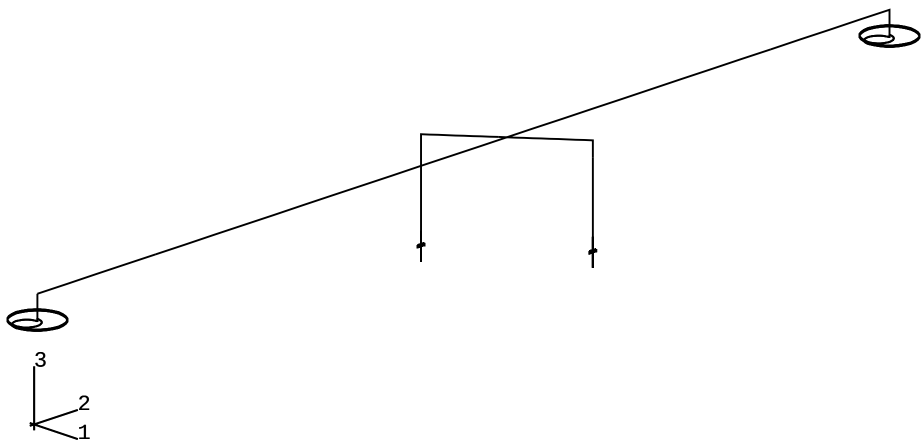

Stick Model

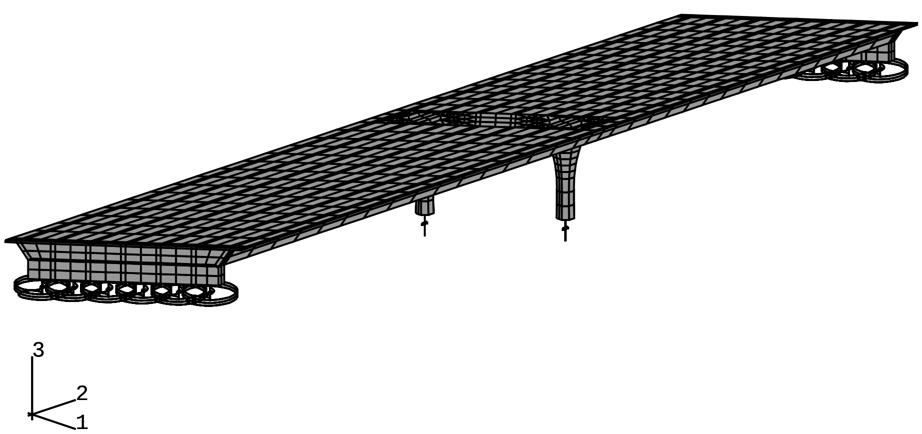

3D Finite Element Model

Figure 4.11. Numerical models of Painter Street Overcrossing (Top: stick model; Bottom: 3D finite element model)

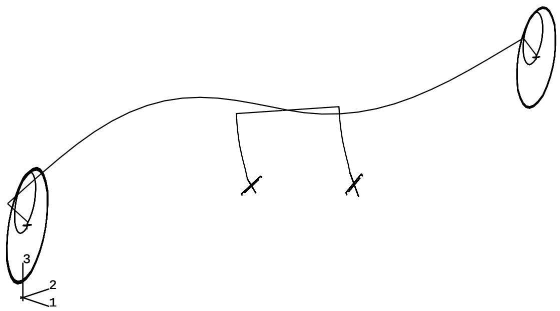

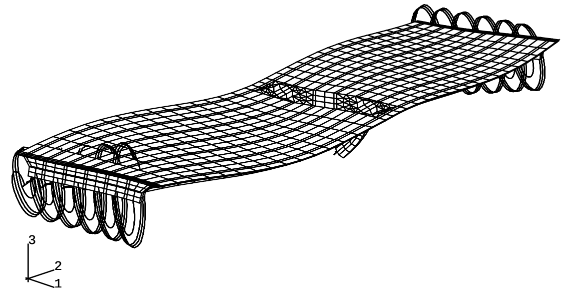

f_1 = 1.78 Hz (2.69 Hz) ξ_1 = 9.0% f_1 = 2.31 Hz (3.06 Hz)

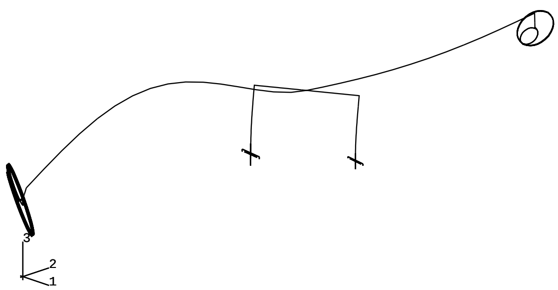

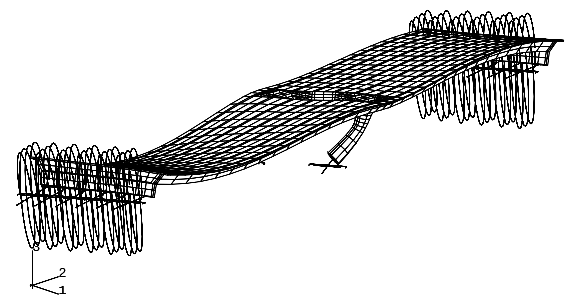

f_2 = 2.29 Hz (3.30 Hz) ξ_2 = 6.7% f_2 = 2.80 Hz (4.29 Hz)

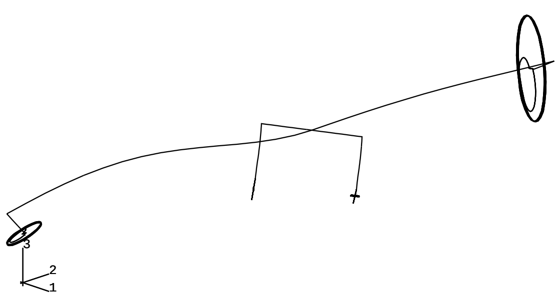

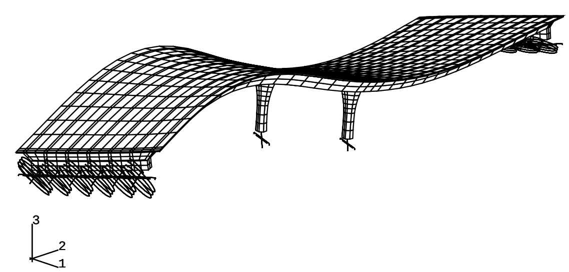

f_3 = 2.60 Hz (4.00 Hz) ξ_3 = 5.8% f_3 = 2.93 Hz (4.45 Hz)

Figure 4.12. First six modal frequencies, damping ratios, and modes computed by stick model (left) and 3D FEM model (right). Values in parentheses are those reported by McCallen and Romstad (1994) (continued).

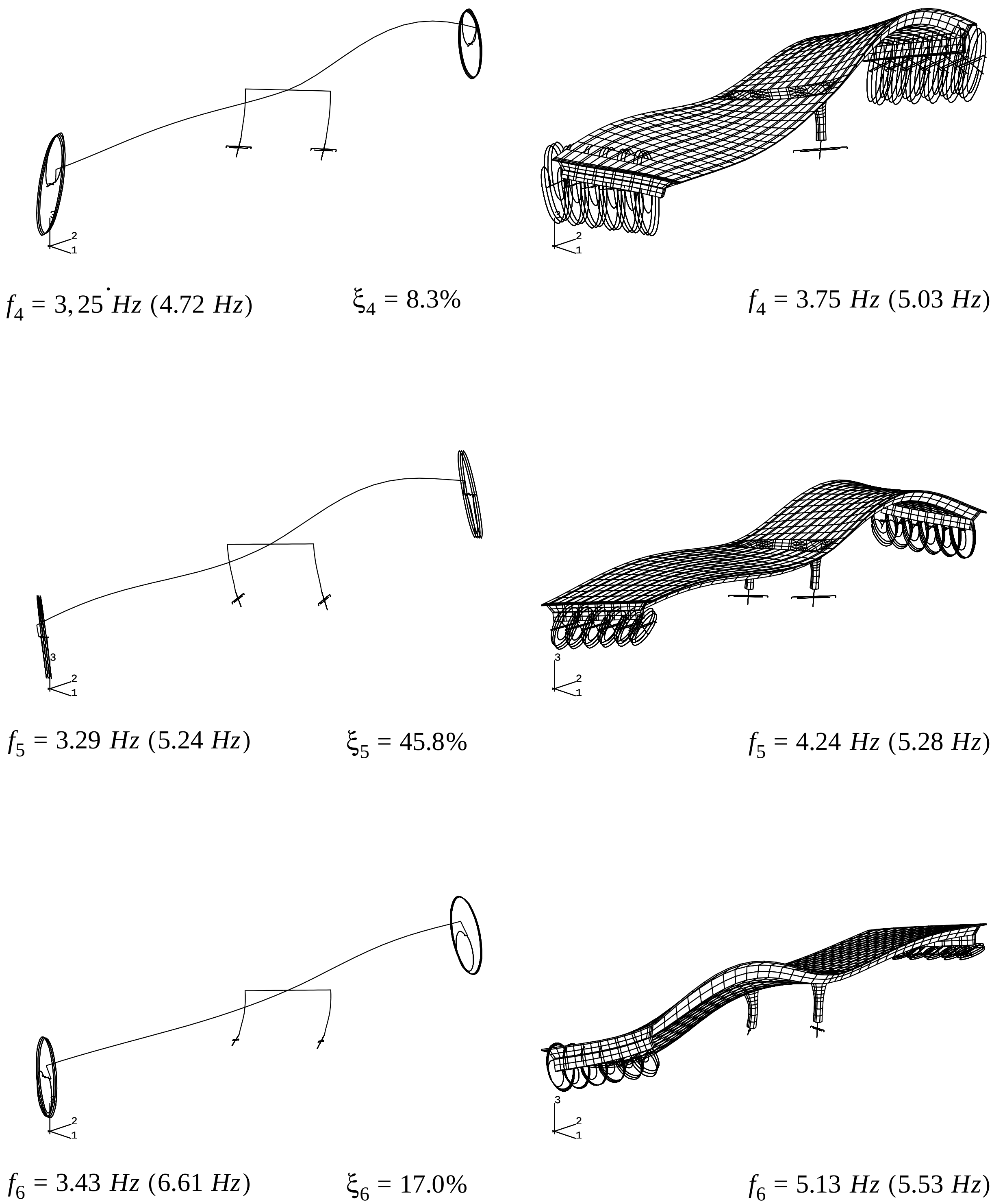

Figure 4.12. First six modal frequencies, damping ratios, and modes computed by stick model (left) and 3D FEM model (right). Values in parentheses are those reported by McCallen and Romstad (1994).

TABLE 4.3. Spring and dashpot values that approximate the presence of the embankments and pile foundations of the Painter Street Overcrossing. Values from this study are associated with the intensity of the 1992 Petrolia earthquake.

<table>
<tr><th colspan="2">Parameters</th><th>1</th><th>2</th><th>3</th><th>4</th><th>5</th></tr>
<tr><td rowspan="6">Embankment + Pile Foundations</td><td>$K_x\ (MN/m)$</td><td>137+180</td><td>201*</td><td>851+105</td><td>117~438+</td><td>810+105
(68+105)</td></tr>
<tr><td>$K_y\ (MN/m)$</td><td>137+180</td><td>/</td><td>815+105</td><td>146~1458+</td><td>876+105</td></tr>
<tr><td>$K_z\ (MN/m)$</td><td>582+773</td><td>564*</td><td>∞</td><td>/</td><td>/</td></tr>
<tr><td>$C_x\ (MN \cdot s/m)$</td><td>9+9</td><td>/</td><td>/</td><td>/</td><td>/</td></tr>
<tr><td>$C_y\ (MN \cdot s/m)$</td><td>9+9</td><td>/</td><td>/</td><td>/</td><td>/</td></tr>
<tr><td>$C_z\ (MN \cdot s/m)$</td><td>17+56</td><td>/</td><td>/</td><td>/</td><td>/</td></tr>
<tr><td rowspan="6">Pile Foundation of Center Bent</td><td>$K_x, K_y\ (MN/m)$</td><td>321</td><td>/</td><td>140</td><td>/</td><td>140</td></tr>
<tr><td>$K_r\ (MN \cdot m/rad)$</td><td>5254</td><td>/</td><td>/</td><td>/</td><td>/</td></tr>
<tr><td>$K_{xr}, K_{yr}\ (MN/rad)$</td><td>354</td><td>/</td><td>/</td><td>/</td><td>/</td></tr>
<tr><td>$K_z\ (MN/m)$</td><td>982</td><td>/</td><td>∞</td><td>/</td><td>/</td></tr>
<tr><td>$C_x, C_y\ (MN \cdot s/m)$</td><td>5</td><td>/</td><td>/</td><td>/</td><td>/</td></tr>
<tr><td>$C_z\ (MN \cdot s/m)$</td><td>20</td><td>/</td><td>/</td><td>/</td><td>/</td></tr>
<tr><td>Note</td><td colspan="6">1. This study ($G = 8.0\ MPa$ and $\eta = 0.50$ for embankment soil)
2. Wilson and Tan 1990a (* embankment only, no piles)
3. McCallen and Romstad 1994
4. Goel and Chopra 1997(+ embankment and piles)
5. Caltrans 1989 Method A (Method B)</td></tr>
</table>

There is a one-to-one correspondence between the mode shapes predicted by the stick model and three-dimensional finite element model. The natural frequencies of the stick model are also in good agreement with that of the three-dimensional finite element model. The first values shown are those computed by adopting the converged soil properties during the strong 1992 Petrolia earthquake. The values shown in the parenthesis are those reported by McCallen and Romstad (1994). They are 50% higher than the values computed in this study. Part of the reason for these discrepancies is the six times larger embankment stiffnesses they used in their study.

Modal damping ratios are estimated with the complex eigenvalue procedure presented in the equivalent section associated with the analysis of the Meloland Road Overcrossing. Similarly, a reduced-order stick model was developed with fewer degrees of freedom in order to bypass the problem of computing and interpreting the large number of complex eigenvalues resulting from the original stick model which consists of 618 degrees of freedom. Table 4.4 presents the first six eigenvalues of the Painter Street Overcrossing that have been computed with the three-dimensional (3-D) finite element model of the undamped bridge (column A), the original stick model of the undamped bridge (column B), the reduced-order stick model of the undamped bridge (column C), and the first six complex eigenvalues of the reduced-order stick model of the damped bridge. Damping ratios computed with this study are shown in column 1 next to other values reported in the literature. Selected observations from the modal values indicated in Table 4.4 are

- Due to the skew configuration, there is strong coupling of modes involved in the eigenvalue analysis.
- The computed modal damping ratio, ξ_j, are larger than the 5% modal damping assumed by Caltrans, however, the first three modal damping ratios are not as high as the modal damping ratios computed for the unskewed Meloland Road Overcrossing. This might be partly due to the strong participation of the vertical mode in the Painter Street Bridge that is associated with less damping.
- The computed first modal damping, $\xi_1 = 9\%$ is approximately half the value that McCallen and Romstad (1994) needed to match the recorded data. However, it is in agreement with the high-end of the modal damping range identified by Goel (1997).
- The longitudinal mode (that was the second mode for the Meloland Road Overcrossing) has been pushed down to the fifth mode. Interestingly, the complex eigenvalue analysis advanced in this study is able to capture the outstandingly high damping, $\xi_5 = 46\%$, associated with this mode. As was indicated during the analysis of the modal properties of the Meloland Road Overcrossing, in which $\xi_2 = 56.5\% \text{ (longitudinal mode)}$, the longitudinal mode mobilize a large volume of soil with high damping.
- The procedure advanced in this study, where the appropriate values of G and η of the soil embankments are established with the kinematic response analysis, yields a first natural frequency that is in very good agreement with the values reported by Goel (1997) and Price and Eberhard (1998).

Figure 4.13 shows Fourier amplitude spectra of channels 4, 7, 9, and 11 of the Painter Street Overcrossing, where the frequency around 2Hz can be identified. The solid lines are the fundamental frequencies computed by the stick model and 3D FEM model in this study while the dashed lines are the values reported by McCallen and Romstad (1994). It can be seen that our prediction is closer to the main amplification of the spectrum.

TABLE 4.4. Modal frequencies, ω_j (rad/s), and damping ratios, ξ_j (%), of Painter Street Overcrossing

Modes	Eigenvalues (rad/s)				1		2		3		4	
	Model A	Model B	Model C	Model D	ω_j	ξ_j	ω_j	ξ_j	ω_j	ξ_j	ω_j	ξ_j
1st transverse/antisymmetric vertical	14.514	11.162	11.364 (11.587)	$11.490 + 1.040i$ $(11.730 + 1.116i)$	11.5 (11.8)	9.0 (9.5)	20.7	20	11.0~17.9	5.6~8.5	10.3	16.6
antisymmetric vertical/torsion about vertical axis	17.593	14.409	14.578 (14.751)	$14.683 + 0.984i$ $(14.863 + 1.006i)$	14.7 (14.9)	6.7 (6.8)	16.9	3				
torsion about vertical axis/ symmetric vertical	18.410	16.366	16.365 (16.366)	$16.527 + 0.962i$ $(16.524 + 0.972i)$	16.6 (16.6)	5.8 (5.9)	25.1	3				
symmetric vertical/longitudinal	23.562	20.691	20.808 (20.994)	$21.075 + 1.761i$ $(21.370 + 1.809i)$	21.1 (21.4)	8.3 (8.4)	32.9	5				
longitudinal	26.641	21.545	20.938 (21.265)	$20.176 + 10.383i$ $(20.394 + 10.395i)$	22.7 (22.9)	45.8 (45.4)	29.6	30				
2nd transverse/torsion about longitudinal axis	32.233	31.156	22.052 (22.532)	$23.754 + 4.096i$ $(24.236 + 4.302i)$	24.1 (24.6)	17.0 (17.5)	41.5	5				
Note	A: Undamped original 3D FEM model B: Undamped original stick model C: Undamped reduced stick model with 174 d.o.f and (138 d.o.f) respectively D: Damped reduced stick model with 174 d.o.f and (138 d.o.f) respectively 1: This study 2: McCallen and Romstad 1994 3: Goel 1997 4. Price and Eberhard 1998											

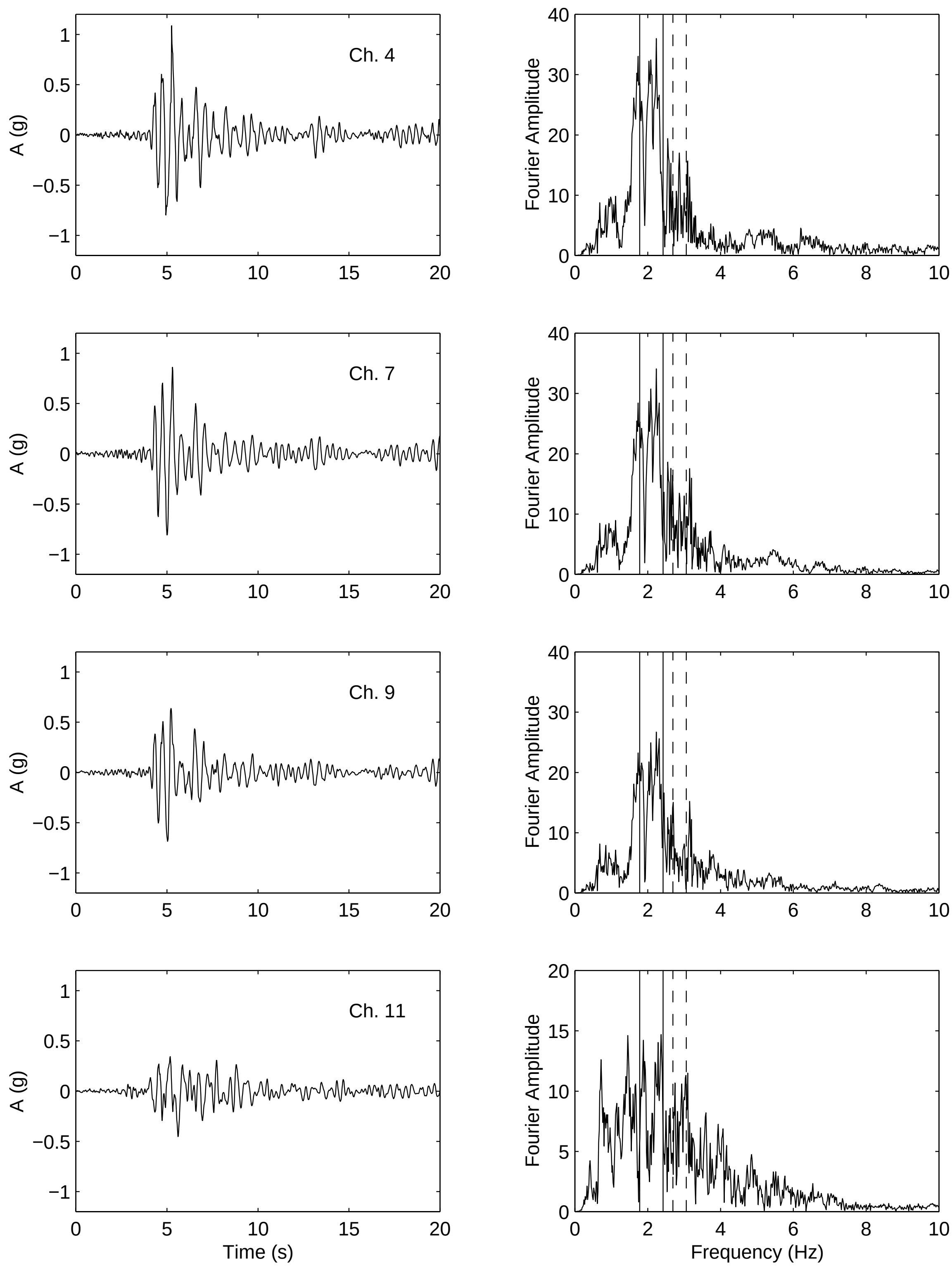

Figure 4.13. Fourier amplitude spectra of accelerations recorded at channels 4, 7, 9, and 11 of Painter Street Overcrossing

4.2.2 Time History Analysis

Figures 4.14 to 4.17 plot total acceleration, relative velocity, and displacement time histories of the bridge response at selected locations. The analysis shown in these figures investigates the sensitivity of the bridge response to the foundation input motion. The first column shows the recorded motions. The second column shows computed response quantities by using as a support motion at the end abutments the crest motions computed using Eq. (2-14). The third column shows the computed response quantities by using as a support motion at the center bent and end abutments the free-field motion. The last column shows computed response quantities by using as a support motion at the end abutments the recorded crest motions.

Figure 4.14 compares the computed responses with the records of channel 4. The case where the recorded crest motions are used as support motions yields invariably the most favorable prediction. When the free-field motions are used as support motions, the bridge response shown along the third column is substantially underestimated, since it has not experienced the amplification that the embankments induce at the two ends. When the computed crest motions are used as support motions the peak accelerations are predicted with marginal discrepancies; however, deck drifts are underestimated by 22%. Figure 4.15 which compares the computed response with the records of channel 7, indicates similar trends. When the free-field motions are used as support motions the discrepancies between records and predictions are of the order of 40% or more, for relative velocities and relative displacements. Similar trends are observed in Figures 4.16 and 4.17, which compare the computed responses with the records of channels 9 and 11.

The sensitivity of the bridge response to the resilience and dissipation of the bridge supports is investigated in Figures 4.18 to 4.21, which plot total acceleration, relative velocity, and displacement time histories. Again the first column shows the recorded motion for convenience. The second column plots the computed response quantities by assuming that the abutments are monolithic supports and soil-structure-interaction happens only at the foundation of the center bent (case (a) of Figure 4.8). The third column plots the computed response quantities by considering soil-structure-interaction at the end abutments and by assuming a monolithic support at the center bent (case (b) of Figure 4.8). The forth column plots the computed response quantities by accounting for soil-structure interaction at the end abutments and at the center bent; the flexibility is included whereas the dissipation of the pile foundation at the center bent is eliminated. In all

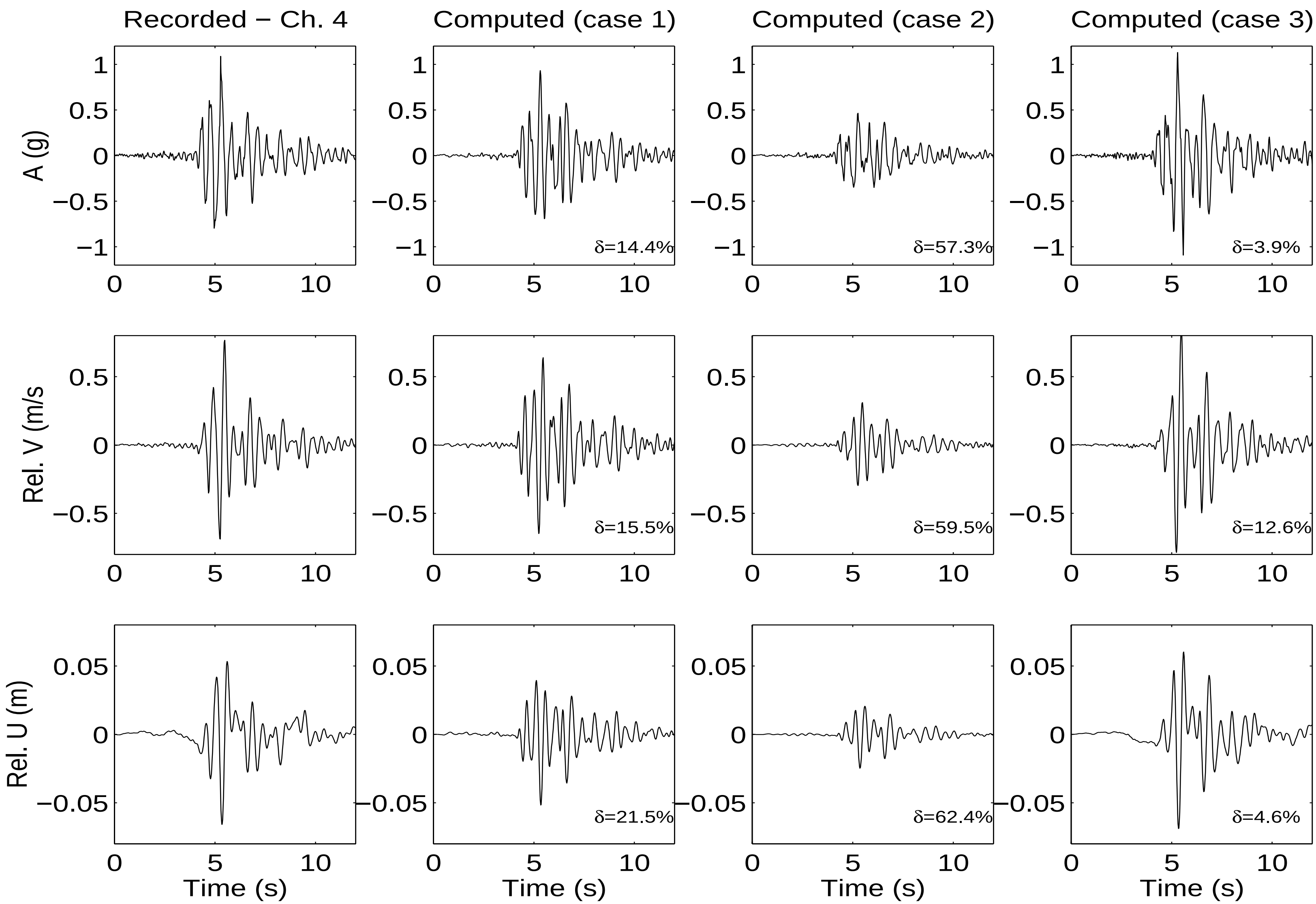

Figure 4.14. Records of channel 4 and predictions of Painter Street Overcrossing response considering different support motions

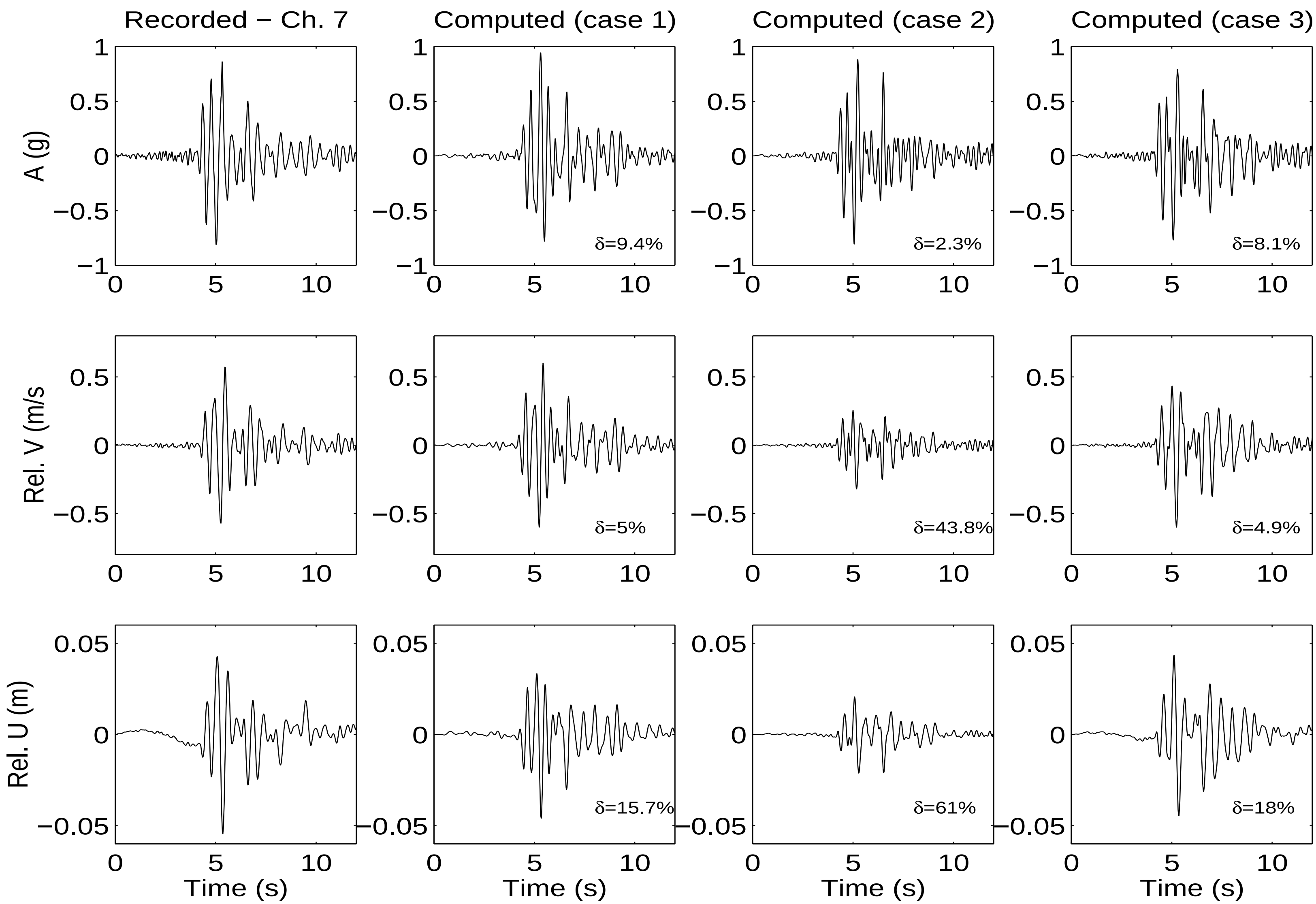

Figure 4.15. Records of channel 7 and predictions of Painter Street Overcrossing response considering different support motions

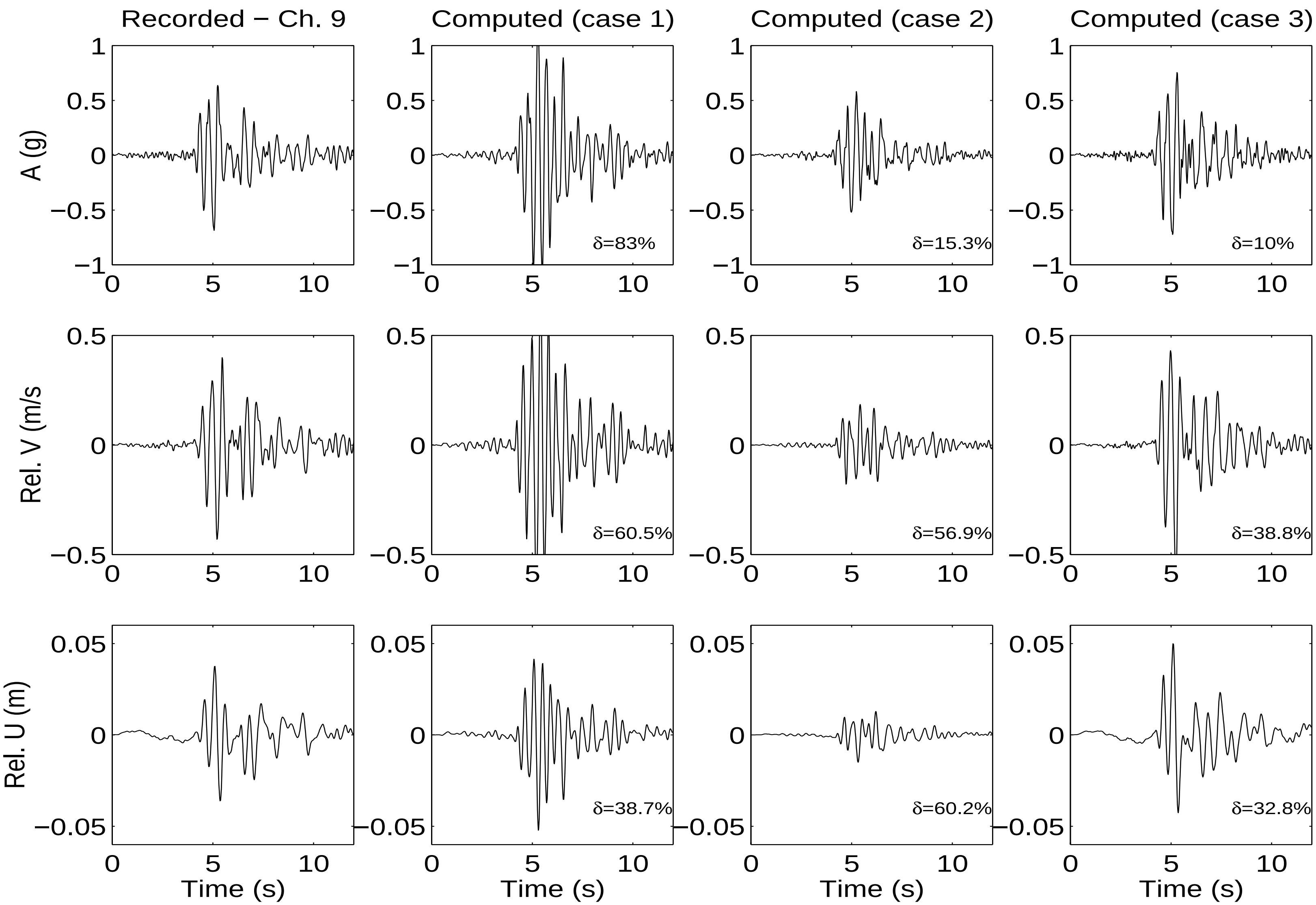

Figure 4.16. Records of channel 9 and predictions of Painter Street Overcrossing response considering different support motions

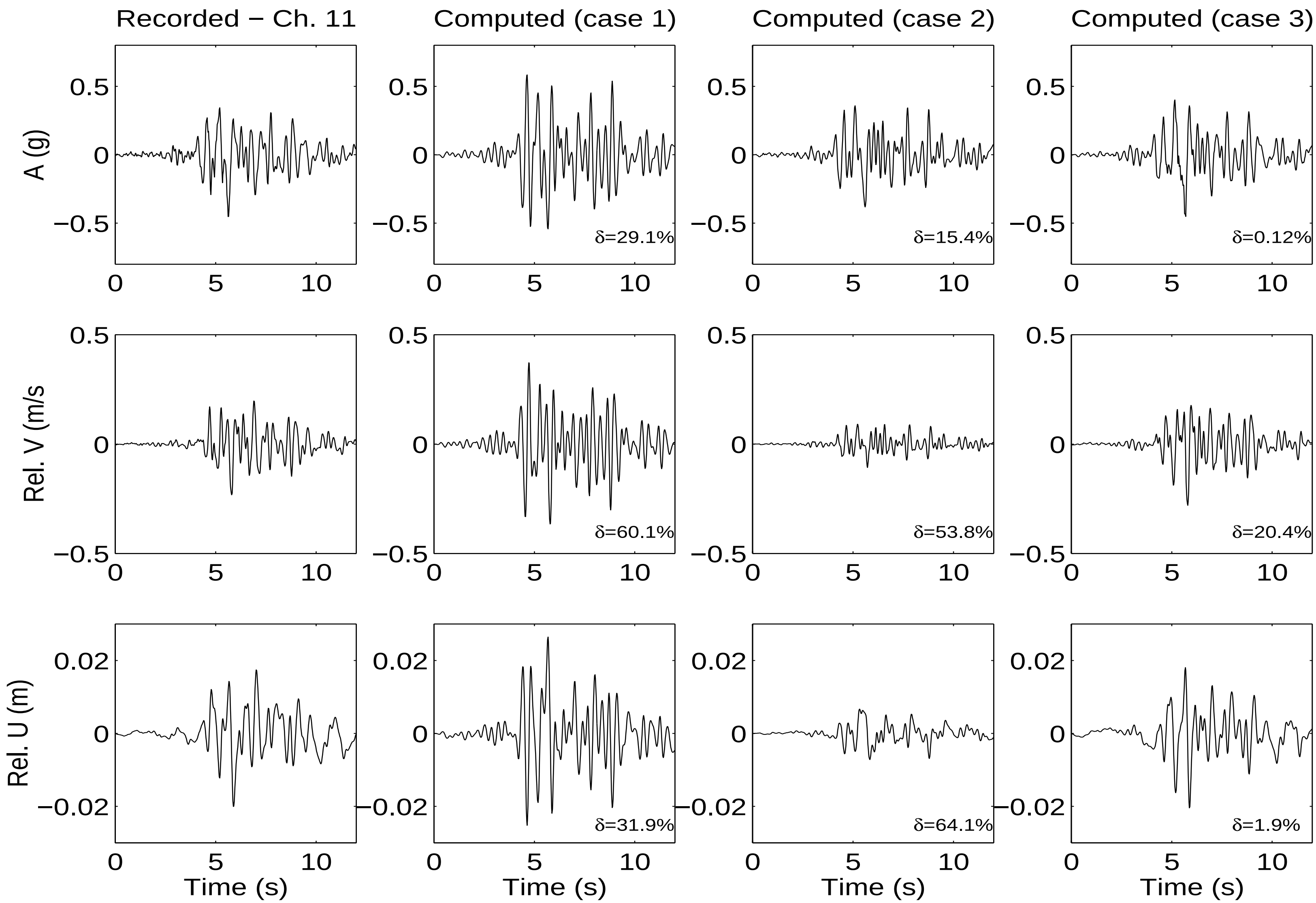

Figure 4.17. Records of channel 11 and predictions of Painter Street Overcrossing response considering different support motions

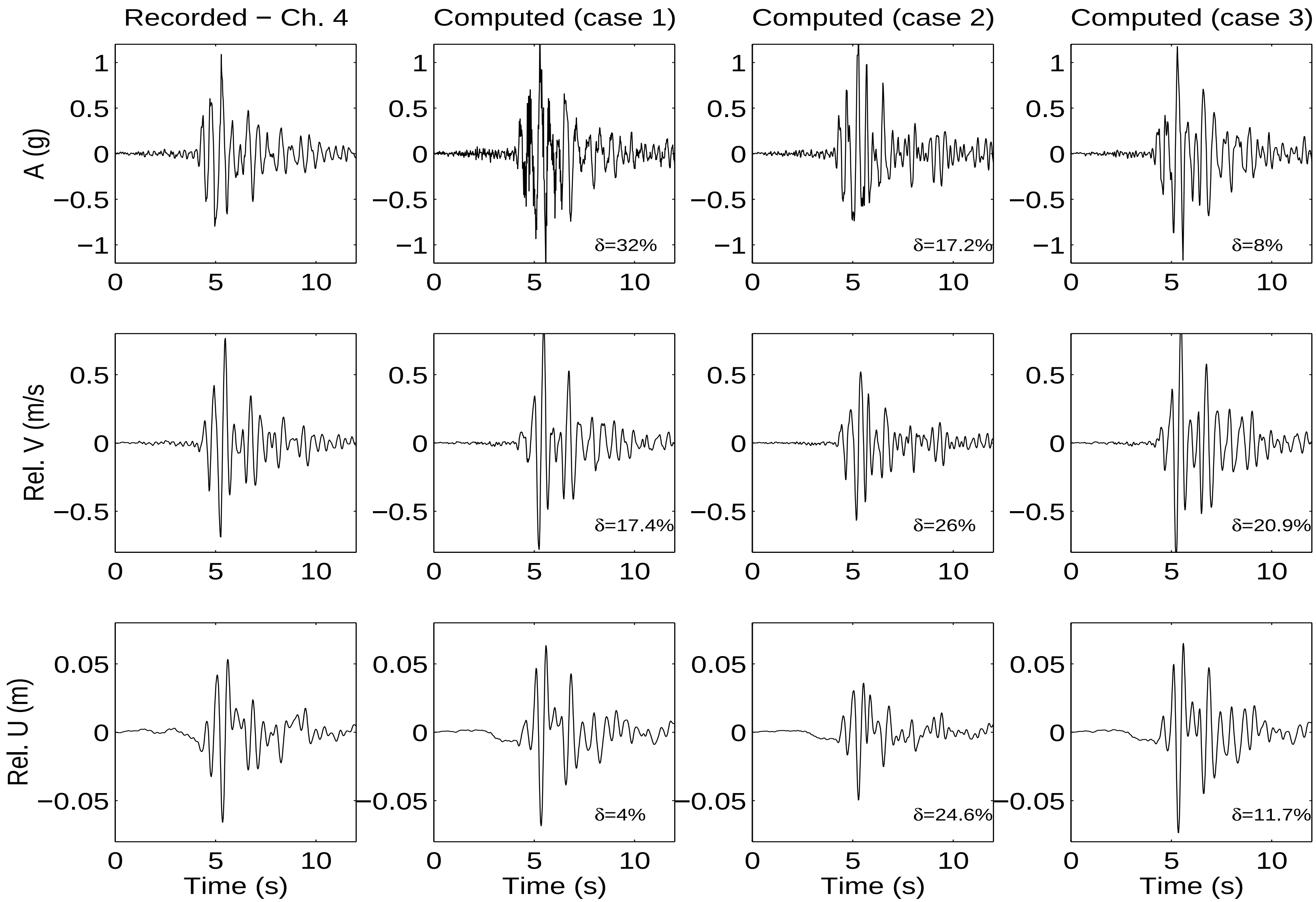

Figure 4.18. Records of channel 4 and predictions of Painter Street Overcrossing response considering different support idealizations

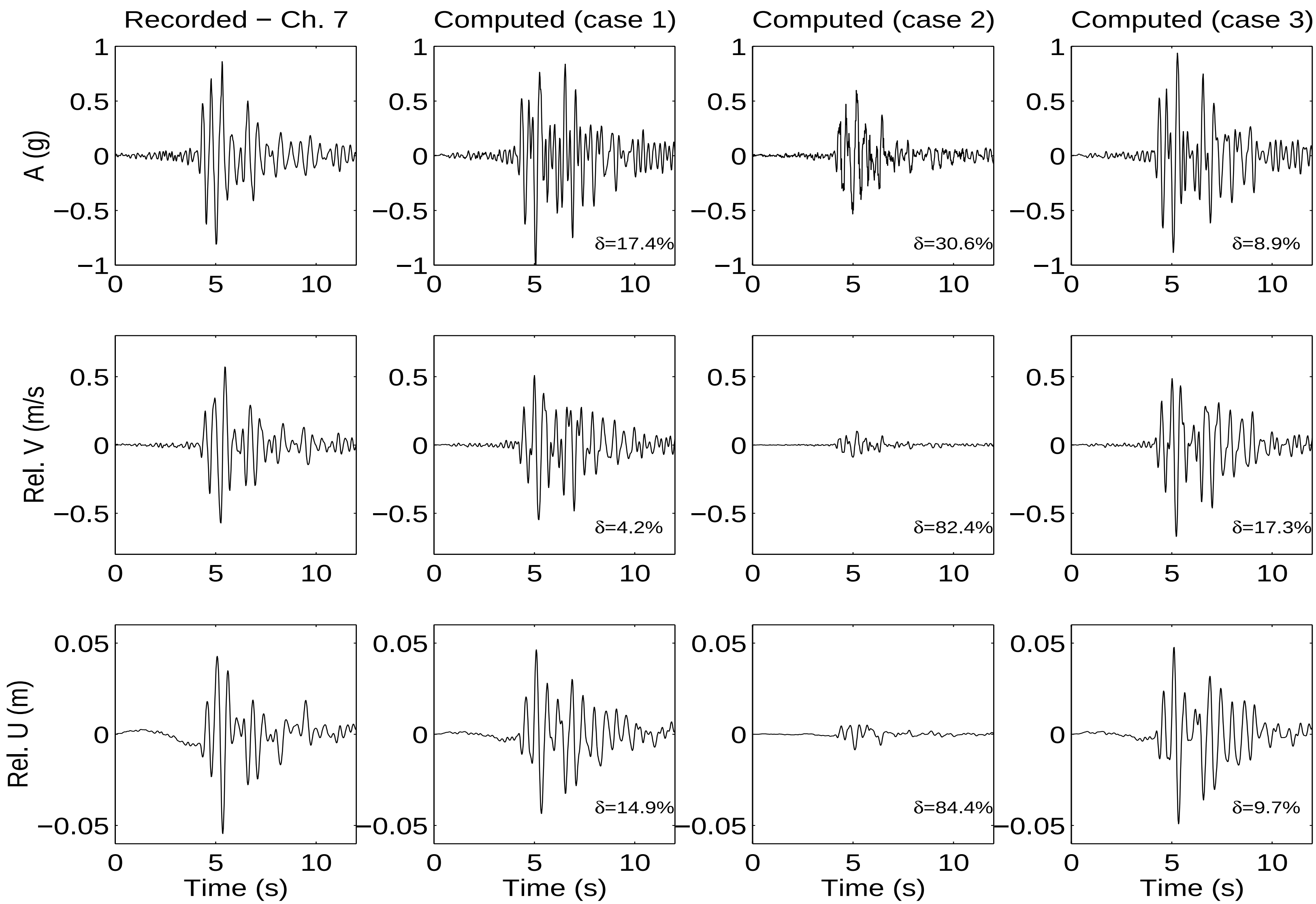

Figure 4.19. Records of channel 7 and predictions of Painter Street Overcrossing response considering different support idealizations

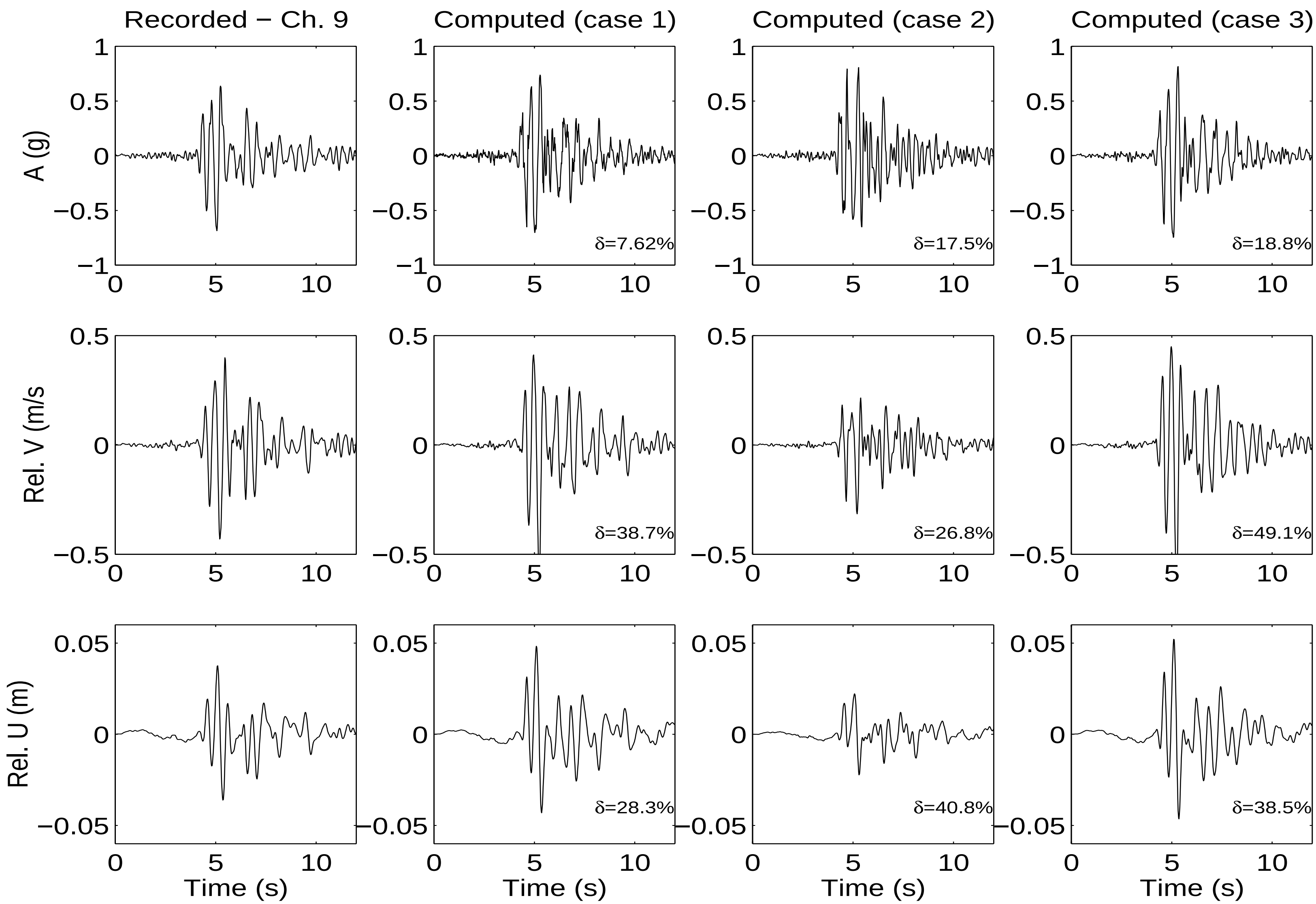

Figure 4.20. Records of channel 9 and predictions of Painter Street Overcrossing response considering different support idealizations

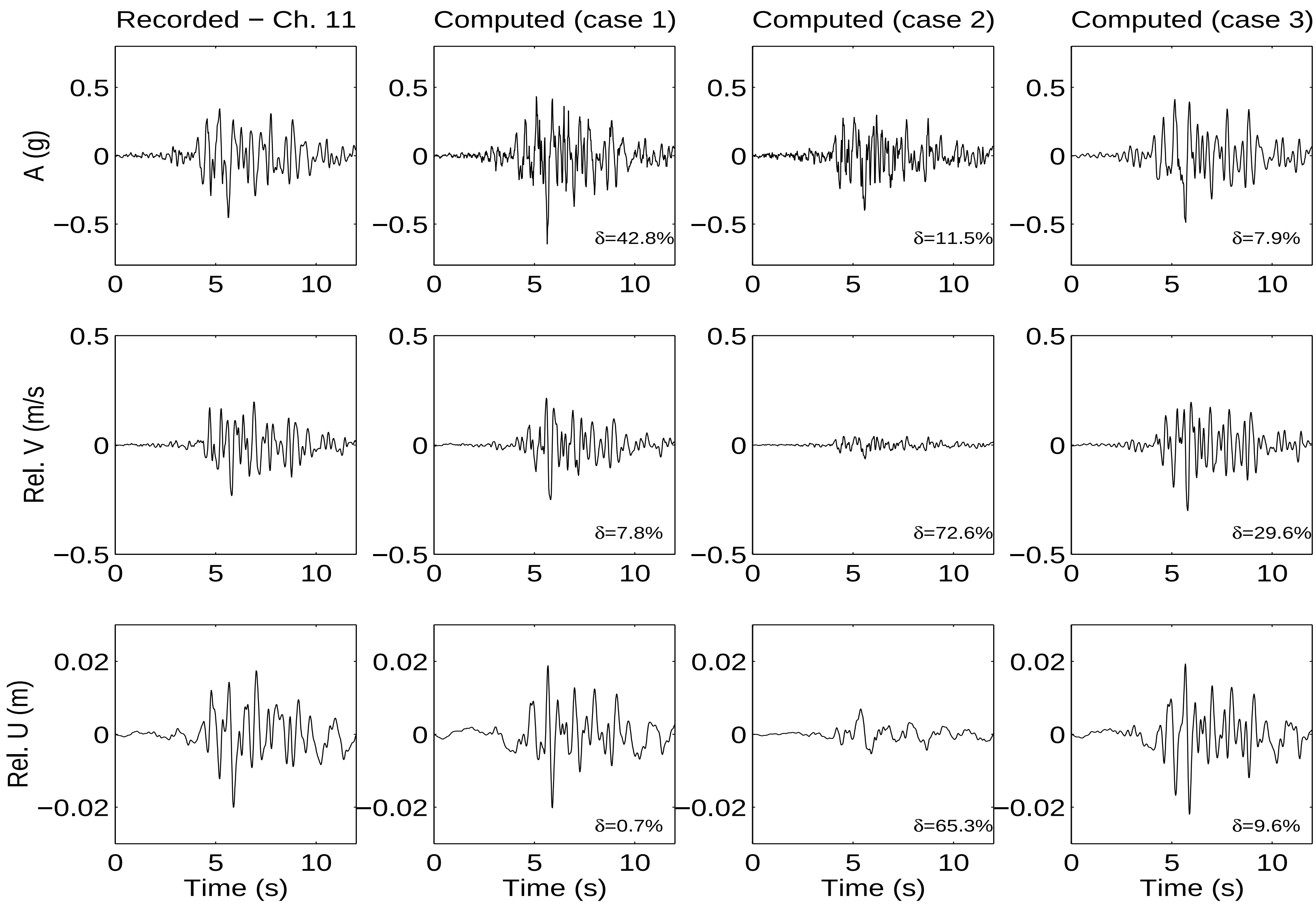

Figure 4.21. Records of channel 11 and predictions of Painter Street Overcrossing response considering different support idealizations

cases the free-field motions were induced at the foundation of the center bent and the recorded crest motions were induced at the end abutments.

Figure 4.18 compares the computed responses with the records of channel 4. It indicates that the resilience of the pile foundation of the center bent is appreciably affecting the response, whereas the associated damping has less important effects. Figure 4.19, which shows computed responses at the mid-span, indicates the similar trends. More specifically, the results obtained by neglecting the damping of the pile foundation at the center bent are comparable to the results obtained when damping is included, a result that confirms the validity of the assumption adopted by Goel and Chopra (1997). Similar trends, observed in Figures 4.20 and 4.21, suggest that in this case the damping of the pile foundation at the center bent has marginal effects; whereas the flexibility of the pile foundations has an appreciable effect and has to be included.

4.3 OUTLINE OF PROPOSED PROCEDURE

The two case studies presented in this report confirmed the validity of a step-by-step procedure to estimate the seismic response of freeway overcrossings. The study shows that the stick model used by Caltrans when enhanced with realistic springs and dashpots at its supports can yield dependable estimates of the seismic response of freeway overcrossings.

Step 1. Compute the kinematic response function of the approach embankments as outlined in section 2.2.5, after establishing the converged values of the equivalent linear soil parameters, G and η.

Step 2. Compute the embankment crest response by amplifying the free-field motion with the kinematic response functions obtained in step 1.

Step 3. Compute the frequency-independent spring and dashpot values of the approach embankment as outlined in section 2.3.5.

Step 4. Compute the frequency-independent spring and dashpot values of the pile groups at the abutments and the center bent as outlined in section 3.5.

Step 5. Construct a stick model of the bridge enhanced with the transverse and longitudinal spring and dashpot values computed in steps 3 and 4.

Step 6. Compute the two-dimensional dynamic response of the model constructed in step 5 (see Figure 1.2) subjected to the free-field motions at the center bent and the crest motions at the abutment ends computed in step 2.

5 Conclusions

The seismic response of highway overcrossings was investigated in this report within the context of equivalent linear analysis. The goal of this study was to identify and characterize the effects of various structural components of the bridge-foundation system and to develop a simple yet dependable method to estimate the earthquake response of short bridges.

Recognizing that soil-structure interaction affects appreciably the earthquake response of highway overcrossings, the kinematic response functions and dynamic stiffnesses of approach embankments were revisited in Chapter 2 and it was concluded that

- During strong shaking soil strains in the embankment can be as large as $\gamma \approx 5 \times 10^{-3}$ or even larger, resulting in equivalent linear shear modulus, $G \approx G_{max}/10$, and damping coefficient, $\eta \approx 0.5$.
- Typical approach embankments even when strained at the above-indicated levels tend to amplify substantially the free-field motions (two to three times).
- The dynamic stiffnesses of embankments, although in theory are frequency dependent, can be approximated in practice with frequency-independent springs and dashpots.
- The unit-width shear-wedge model can be extended to a two-dimensional model that yields dependable estimates of the transverse static stiffness of approach embankments when loaded at one end. The formulation reveals a sound closed-form expression for the critical length, L_c, that is the ratio of the transverse static stiffness of an approach embankment to the transverse static stiffness of a unit-width wedge.
- The simple expression for the critical length, $L_c \approx 0.7\sqrt{SB_cH}$ allows for a realistic estimation of the dynamic stiffness of the approach embankment from the dynamic stiffness of a unit-width shear-wedge.

Chapter 3 summarizes current state-of-art procedures to compute the dynamic stiffnesses of piles and pile groups. They were implemented to compute the dynamic stiffnesses of the pile groups at the end abutments and the center bents of the two instrumented bridges studied in this report — the Meloland Road Overcrossing and the Painter Street Overcrossing. The study indicates that the dynamic stiffnesses of pile groups, although in theory are frequency dependent, can be approximated in practice with frequency-independent springs and dashpots.

The free-vibration and earthquake responses of the two aforementioned bridges of interest were examined in Chapter 4 with a reduced-order stick model and a more detailed three-dimensional finite element model. Either model in this study was enhanced with the springs and dashpots established in chapters 2 and 3 to account for the presence of the approach embankments and pile foundations. Our analysis revealed distinguishable trends that lead to the following conclusions:

- The reduced-order stick model yields comparable modal parameters and seismic response characteristics to the more detailed three-dimensional finite element model. It is capable to capture the dynamic characteristics of a skewed overcrossing that exhibits strong coupling of its vibration modes.
- The modal damping ratios, ξ_j, of either the straight Meloland Road Overcrossing and the skewed Painter Street Overcrossing are much larger than the 5% modal damping ratios assumed by Caltrans.
- The first mode of the straight Meloland Road Overcrossing is the transverse mode; whereas, for the skewed Painter Street Overcrossing, it is the coupled transverse/first antisymmetric vertical mode.
- The first modal damping ratio of the Meloland Road Overcrossing is of the order of 20%; whereas, for the Painter Street Overcrossing, it is of the order of 10%. The smaller amount of the first modal damping in the skewed Painter Street Overcrossing is because the transverse mode is coupled with the first antisymmetric vertical mode that is lightly damped.
- The longitudinal mode emerges as the second mode for the straight Meloland Road Overcrossing; whereas, in the skewed Painter Street Overcrossing, it is pushed down to the fifth place. In both cases the modal damping ratio along the longitudinal direction is of the order of 50%.
- Vertical vibration modes exhibit smaller damping ratios (8% to 10%).
- The torsional mode of the straight and symmetric overcrossings is highly damped. For the particular case of the Meloland Road Overcrossing, the torsional mode (4th mode) was critically damped, $\xi_4 \approx 100\%$. In contrast, in the case of the skewed Painter Street Overcrossing the tor-

sional mode is coupled with the symmetric vertical mode and the modal damping was as low as $\xi_3 \approx 6\%$.

- Time history analysis shows that the amplified crest motions of the approach embankments have an appreciable effect on the bridge response and should not be neglected.
- Parametric studies that examine the effect of different support idealizations indicate that neglecting the resilience of the foundation of the center bent yields unrealistic small drifts, while neglecting the dissipation of the foundation of the center bent has a marginal effect.

In summary, in view of the strong effect of soil-structure interaction, it is concluded that the earthquake response of highway overcrossings can be realistically computed with the stick model used by Caltrans provided that (a) it is enhanced with the springs and dashpots established in chapters 2 and 3 and (b) it is subjected at its end abutments to the amplified crest motions calculated in Chapter 2.

References

AASHTO-83. 1988. *Guide specifications for seismic design of highway bridges.* Washington, D. C.: American Association of State Highway and Transportation Officials.

ABAQUS. 1997. Hibbitt, Karlsson & Sorensen, Inc.

Abramowitz, M. and I. A. Stegun. 1970. *Handbook of mathematical functions with formulas, graphs, and mathematical tables*. New York: Dover Publications, Inc.

Badoni, D., and N. Makris. 1997. *Analysis of the nonlinear response of structures supported on pile foundations.* Report No. UCB/EERC-97/07. Berkeley, Calif.: University of California.

Blaney, G. W., E. Kausel, and J. M Roesset. 1976. Dynamic stiffness of piles, in *Proceedings of the 2nd International Conference on Numerical Methods in Geomechanics,* Vol. 2, pp. 1001–12. Blacksburg, Va.: Virginia Polytechnical Institute and State University.

Caltrans. 1989. *Bridge design aids 14-1*. Sacramento, Calif.: California Department of Transportation.

Caughey, T. K. 1962. Vibrations of dynamic systems with linear hysteretic damping (linear theory). In *Proc. 4th U. S. Natl. Congr. Appl. Mech.,* pp. 87–97. New York: ASME.

Chopra, A. K. 1967. Earthquake response of earth dams. *J. of Soil Mechanics and Foundation Division* 93: SM2. ASCE.

Chopra, A. K. 1995. *Dynamics of structures: theory and applications to earthquake engineering.* Englewood Cliffs, N.J.: Prentice Hall.

Crandall, S. H. 1963. Dynamic response of systems with structural damping. In *Air, space and instruments,* S. Lees ed., pp. 183–93. New York: McGraw Hill.

Crandall, S. H. 1970. The role of damping in vibration theory. *J. of Sound and Vibration* 11(1): 3–18.

Crouse, C. B., B. Hushmand, and G. R. Martin. 1987. Dynamic soil-structure interaction of single-span bridge. In *Earthquake Engineering and Soil Dynamics,* Vol. 15, pp. 711–29.

Crouse, C. B. and T. Price. 1993. Dynamic soil-foundation interaction at the Meloland Road Overcrossing. *Structural Engineering in Natural Hazards Mitigation: Proceedings of Papers Presented at the Structures Congress '93*, Vol. 1, pp. 355–60. New York: ASCE.

Dakoulas, P., and G. Gazetas. 1985. A class of inhomogeneous shear models for seismic response of dams and embankments. *Soil Dynamics and Earthquake Engineering* 4(4): 166–82.

Dakoulas, P., and G. Gazetas. 1986. Seismic shear strains and seismic coefficients in dams and embankments. *Soil Dynamics and Earthquake Engineering* 5(2): 75–83.

Delis, E. A., R. B. Malla, M. Madani, and K. J. Thompson. 1996. Energy dissipation devices in bridges using hydraulic dampers. In *Proc. Structures Congress XIV,* Vol. 2, pp. 1188–96. Chicago: ASCE.

Dendrou, B., S. D. Werner, and T. Toridis. 1985. Three-dimensional response of a concrete bridge system to traveling seismic waves. *Computers & Structures* 20: 593–603.

Dobry, R. and G. Gazetas. 1988. Simple method for dynamic stiffness and damping of floating pile groups. *Geotechnique* 38: 557–74.

Douglas, B. M. and W. H. Reid. 1982. Dynamic tests and system identification of bridges. *J. of the Structural Division* 108(ST10): 2295–2312. ASCE.

Douglas, B. M., E. Maragakis, and S. Vrontinos. 1991. Parameter identification studies of the Meloland Road Overcrossing. In *Proc. Pacific Conference on Earthquake Engineering*, Vol. 1, pp. 105–16. [Wellington], New Zealand: New Zealand National Society for Earthquake Engineering.

Fan, K., G. Gazetas, A. Kaynia, E. Kausel, S. Ahmad. 1991. Kinematic seismic response of single piles and pile groups. *J. of Geotechnical Engineering* 117(12): 1860–79.

Federal Highway Administration. 1995. *Seismic retrofitting manual for highway bridges.* Publication No. FHWA-RD-94-052. Springfield, Va.: Office of Research and Development, Federal Highway Administration.

Flugge, W. 1975. *Viscoelasticity.* New York: Springer.

Gates, J. H. 1993. Dynamic field response studies and earthquake instrumentation of the Meloland Road Overcrossing. *Structural Engineering in Natural Hazards Mitigation: Proc. of Papers Presented at the Structures Congress '93*, Vol.1, pp. 343–48. New York: ASCE.

Gazetas, G. 1984. Seismic response of endbearing piles. *Soil Dynamics and Earthquake Engineering* 3(2): 82–93.

Gazetas, G. 1987. Seismic response of earth dams: some recent developments. *Soil Dynamics and Earthquake Engineering* 6(1): 2–47.

Gazetas, G., and R. Dobry. 1984a. Horizontal response of piles in layered soils. *J. of Geotechnical Engineering* 110: 20–40. ASCE.

Gazetas, G., and R. Dobry. 1984b. Single radiation damping model for piles and footings. *J. of Engineering Mechanics*. 110:937–56.

Gazetas, G., K. Fan, A. Kaynia, E. Kausel. 1991. Dynamic interaction factors for floating pile groups. *J. of Geotechnical Engineering* 117(10): 1531–48.

Goel, R. K. 1997. Earthquake behavior of bridges with integral abutments. In *Proc. of the National Seismic Conference on Bridges and Highways: Progress in Research and Practice*, pp. 149–59. Sacramento, Calif.

Goel, R. K., and A. K. Chopra. 1997. Evaluation of bridge abutment capacity and stiffness during earthquakes. *Earthquake Spectra*. 13(1): 1–23.

Hardin, B. O. 1965. The nature of damping in sand. *J. of Soil Mechanics & Foundation Engineering* 91:63–97. New York.

Heuze, F. E., and R. P. Swift. 1991. *Seismic refraction studies at the Painter Street Bridge site, Rio Dell, California.* Report UCRL-ID-108595. Oak Ridge, Tenn.: Lawrence Livermore National Laboratory.

Idriss, I. M., H. B. Seed, N. Serff. 1974. Seismic response by variable damping finite elements. *J. of Geotechnical Engineering* 100(GT1): 1–13.

Inaudi, J. A., and J. M. Kelly. 1995. Linear hysteretic damping model and the Hilbert transform. *J. of Engineering Mechanics* 121(5): 626–32. ASCE.

Iwasaki, T., F. Tatsuoka, and Y. Takagi. 1978. Shear moduli of sands under cyclic torsional shear loading. *Soils and Foundations* 18(1): 39–56.

Kaynia, A. M., and E. Kausel. 1982. *Dynamic stiffness and seismic response of sleeved piles.* Report No. R80-12. Cambridge, Mass.: Massachusetts Institute of Technology.

Kaynia, A. M., and M. Novak 1992. Response of pile foundations to Rayleigh waves and to obliquely incident body waves. *Earthquake Engineering and Structural Dynamics* 21(4): 115–32.

Ketter et al. 1979. *Structural analysis and design.* New York: McGraw-Hill.

Makris, N. 1994. Soil-pile interaction during the passage of Rayleigh waves: an analytical solution. *Earthquake Engineering and Structural Dynamics* 23: 153–67.

Makris, N., and D. Badoni. 1995. Seismic response of pile-groups during the passage of oblique-shear and Rayleigh waves. *Earthquake Engineering and Structural Dynamics* 24: 517–32.

Makris, N., and G. Gazetas. 1992. Dynamic pile-soil-pile interaction Part II: Lateral and seismic response. *Earthquake Engineering and Structural Dynamics* 21(2): 145–62.

Makris, N., and G. Gazetas. 1993. Displacement phase differences in a harmonically oscillating pile. *Geotechnique* 43(1): 135–50.

Makris, N., D. Badoni, E. Delis, and G. Gazetas. 1994. Prediction of observed bridge response with soil-pile-structure interaction. *J. of Structural Engineering* 120(10): 2992–3011.

Makris, N. 1997. Causal hysteretic element. *J. of Engineering Mechanics* 123(11): 1209–214. ASCE.

Makris, N., and J. Zhang. 2000. Time-domain viscoelastic analysis of earth structures. E*arthquake Engineering and Structural Dynamics* 29: 745–68.

Mamoon, S. M., and P. K. Banerjee. 1990. Response of piles and pile groups to travelling SH-waves. *Earthquake Engineering and Structural Dynamics* 19: 579–610.

Maragakis, E. A. 1985. A *model for the rigid body motion of skew bridges.* Report No. EERL 85-02. Pasadena, Calif.: California Institute of Technology.

Maragakis, E. A., and P. C. Jennings. 1987. Analytical models for the rigid body motions of skew bridges. *Earthquake Engineering and Structural Dynamics* 15(8): 923–44.

Maragakis, E., B., M. Douglas, and S. M. Abdel-Ghaffar. 1994. An equivalent linear finite element approach for the estimation of pile foundation stiffnesses. *Earthquake Engineering & Structural Dynamics* 23(10): 1115–24.

Maroney, B., K. Romstad, and M. Chajes. 1990. Interpretation of Rio Del freeway response during six recorded earthquake events. In *Proc. 4th U.S. National Conference on Earthquake Engineering*, Vol. 1, pp. 1007–16.

Maroney, B. A., K. M. Romstad, and B. Kutter. 1993. Experimental testing of laterally loaded large scale bridge abutments. *Structural Engineering in Natural Hazards Mitigation: Proceedings of Papers Presented at the Structures Congress '93*, Vol. 2, pp. 1065–70. New York: ASCE.

MATLAB. 1997. Natick, Mass.: Mathworks Inc.

McCallen, D. B., and K. M. Romstad. 1994. Analysis of a skewed short-span, box-girder overpass. *Earthquake Spectra* 10(4): 729–55.

Mononobe, H. A. 1936. Seismic stability of the earth dam. In *Proc. 2nd Congress on Large Dams*, IV. Washington D.C.

Novak, M. 1991. Piles under dynamic loads: state of the art. In *2nd Int. Conf. Recent Adv. Geotech Earthq. Engrg. Soil Dynamics*, Vol III, pp. 250–73. St. Louis, Mo.

Novak, M., Nogami, T., and F. Aboul-Ella. 1978. Dynamic soil reaction for plane strain case. *J. of Engineering Mechanics Division* 104: 1465–88. ASCE.

Poulos, H. G. 1968. Analysis of the settlement of pile groups. *Geotechnique* 18(4): 449–71.

Price, T. E., and M. O. Eberhard. 1998. Efficient procedure for modeling the transverse seismic response of bridge embankments. In *Proc., Sixth U.S. National Conference on Earthquake Engineering*. Oakland, Calif.: Earthquake Engineering Research Institute.

Priestley, M. J. N., F. Seible, and G. M. Calvi. 1996. *Seismic design and retrofit of bridges.* New York: John Wiley.

Randolph, M. F. 1977. *A theoretical study of the performance of piles.* Ph.D. thesis. Cambridge, England: Cambridge University.

Roesset, J. M. 1984. Dynamic stiffness of pile groups. In *Pile Foundations.* New York: ASCE.

Roesset, J. M., and D. Angelides. 1980. Dynamic stiffness of piles. In *Numerical methods in offshore piling*, pp. 75–82. London: Institution of Civil Engineers.

Romstad, K. M., B. Kutter, B. Maroney, E. Vanderbilt, M. Griggs, Y. H. Chai. 1995. *Experimental measurements of bridge abutment behavior.* Report No. UCD-STR-95-1. Davis, Calif.: University of California.

Sanchez-Salinero, I. 1983. *Dynamic stiffness of pile groups: approximate solutions*. Geotech. Engrg. Report No. GR83-5. Austin, Texas: University of Texas.

Seed, H. B., and I. M. Idriss. 1969. Influence of soil conditions on ground motions during earthquakes. *J. of Soil Mechanics and Foundations* 95(V SM1): 99–137. ASCE.

Seed, H. B., and I. M. Idriss. 1970. *Soil moduli and damping factors for dynamic response analysis.* Report No. EERC 70-10. Berkeley, Calif.: University of California.

Siddharthan, R., M. El-Gamal, E. A. Maragakis. 1993. Investigation of performance of bridge abutments in seismic regions. *J. of Structural Engineering* 120(4): 1327–46. ASCE.

Siddharthan, R., M. El-Gamal, and E. A. Maragakis. 1997. Stiffnesses of abutments on spread footings with cohesionless backfill. *Canadian Geotechnical J.* 34(5): 686–97.

Skinner, R. I., W. H. Robinson, and G. H. McVerry. 1993. *An introduction to seismic isolation*. Chichester, U.K. and New York: John Wiley & Sons.

Sweet, J. 1993. *A technique for nonlinear soil-structure interaction.* Rep. CAI093-100, Sacramento, California.

Tajimi, H. 1977. Seismic effects on piles, state-of-the-art report No.2. In *Int. Conf. Soil Mech. Found. Engrg., Proc. Specialty Session 10,* pp. 15–27.

Tatsuoka, F., T. Iwasaki, Y. Takagi, 1978. Hysteretic damping of sands and cyclic loading and its relation to shear modulus. *Soils and Foundations* 18(2): 25–40.

Tseng, W.-S., and J. Penzien. 2000. Soil-foundation-structure interaction. In *Bridge Engineering Handbook,* chapter 42, eds. W.-F. Chen, and L. Duan. Boca Raton, Fla.: CRC Press.

Veletsos, A. S., and C. E. Ventura. 1986. Modal analysis of non-classically damped linear systems. *Earthquake Engineering and Structural Dynamics* 14: 217–43.

Veletsos, A. S., and V. Verbic. 1974. Basic response functions for elastic foundations. *J. of Engineering Mechanics* 100(EM2): 189–202. ASCE.

Vucetic, M., and R. Dobry. 1991. Effect of soil plasticity on cyclic response. *J. of Geotechnical Engineering* 117(1): 89–107. ASCE.

Werner, S. D., J. L. Beck, and M. B. Levine. 1987. Seismic response evaluation of Meloland road overpass using 1979 Imperial valley earthquake records. *Earthquake Engineering and Soil Dynamics* 15: 249–74.

Werner, S. D. 1994. Study of Caltrans' seismic evaluation procedure for short bridges. In *Proc. 3rd Annual Seismic Research Workshop*. Sacramento, Calif.: California Department of Transportation.

Wilson, J. C. 1986. System identification of the seismic response of a highway bridge. In *Proc., 8th European Conference on Earthquake Engineering,* Vol. 3, pp. 17–24.

Wilson, J. C. 1988. Stiffness of non-skew monolithic bridge abutments for seismic analysis. *Earthquake Engineering & Structural Dynamics* 16(6): 867–83.

Wilson, J. C., and B. S. Tan. 1990a. Bridge abutments: formulation of simple model for earthquake response analysis. *J. of Engineering Mechanics* 116(8): 1828–37.

Wilson, J. C., and B. S. Tan. 1990b. Bridge abutments: accessing their influence on earthquake response of Meloland Road Overpass. *J. of Engineering Mechanics* 116(8): 1838–56.

Wolf, J. P. 1994. *Foundation vibration analysis using simple physical models.* Inglewood Cliffs, N.J.: Prentice-Hall.

PEER REPORTS

PEER reports are available from the National Information Service for Earthquake Engineering (NISEE). To order PEER reports, please contact the Pacific Earthquake Engineering Research Center, 1301 South 46th Street, Richmond, California 94804-4698. Tel.: (510) 231-9468; Fax: (510) 231-9461.

PEER 2001/03 *A Modal Pushover Analysis Procedure to Estimate Seismic Demands for Buildings: Theory and Preliminary Evaluation.* Anil K. Chopra and Rakesh K. Goel. January 2001. $15.00

PEER 2001/02 *Seismic Response Analysis of Highway Overcrossings Including Soil-Structure Interaction.* Jian Zhang and Nicos Makris. March 2001. $20.00

PEER 2001/01 *Experimental Study of Large Seismic Steel Beam-to-Column Connections.* Egor P. Popov and Shakhzod M. Takhirov. November 2000. $15.00

PEER 2000/09 *Structural Engineering Reconnaissance of the August 17, 1999, Kocaeli (Izmit), Turkey, Earthquake.* Halil Sezen, Kenneth J. Elwood, Andrew S. Whittaker, Khalid Mosalam, John J. Wallace, and John F. Stanton. December 2000. $20.00

PEER 2000/07 *Cover-Plate and Flange-Plate Reinforced Steel Moment-Resisting Connections.* Taejin Kim, Andrew S. Whittaker, Amir S. Gilani, Vitelmo V. Bertero, and Shakhzod M. Takhirov. September 2000. $33.00

PEER 2000/06 *Seismic Evaluation and Analysis of 230-kV Disconnect Switches.* Amir S. J. Gilani, Andrew S. Whittaker, Gregory L. Fenves, Chun-Hao Chen, Henry Ho, and Eric Fujisaki. July 2000. $26.00

PEER 2000/05 *Performance-Based Evaluation of Exterior Reinforced Concrete Building Joints for Seismic Excitation.* Chandra Clyde, Chris P. Pantelides, and Lawrence D. Reaveley. July 2000. $15.00

PEER 2000/04 *An Evaluation of Seismic Energy Demand: An Attenuation Approach.* Chung-Che Chou and Chia-Ming Uang. July 1999. $20.00

PEER 2000/03 *Framing Earthquake Retrofitting Decisions: The Case of Hillside Homes in Los Angeles.* Detlof von Winterfeldt, Nels Roselund, and Alicia Kitsuse. March 2000. $13.00

PEER 2000/01 *Further Studies on Seismic Interaction in Interconnected Electrical Substation Equipment.* Armen Der Kiureghian, Kee-Jeung Hong, and Jerome L. Sackman. November 1999. $20.00

PEER 1999/14 *Seismic Evaluation and Retrofit of 230-kV Porcelain Transformer Bushings*. Amir S. Gilani, Andrew S. Whittaker, Gregory L. Fenves, and Eric Fujisaki. December 1999. $26.00

PEER 1999/12 *Rehabilitation of Nonductile RC Frame Building Using Encasement Plates and Energy-Dissipating Devices.* Mehrdad Sasani, Vitelmo V. Bertero, James C. Anderson. December 1999. $26.00

PEER 1999/11 *Performance Evaluation Database for Concrete Bridge Components and Systems under Simulated Seismic Loads.* Yael D. Hose and Frieder Seible. November 1999. $20.00

PEER 1999/10 *U.S.-Japan Workshop on Performance-Based Earthquake Engineering Methodology for Reinforced Concrete Building Structures.* December 1999. $33.00

PEER 1999/09 *Performance Improvement of Long Period Building Structures Subjected to Severe Pulse-Type Ground Motions*. James C. Anderson, Vitelmo V. Bertero, and Raul Bertero. October 1999. $26.00

PEER 1999/08 *Envelopes for Seismic Response Vectors.* Charles Menun and Armen Der Kiureghian. July 1999. $26.00

PEER 1999/07 *Documentation of Strengths and Weaknesses of Current Computer Analysis Methods for Seismic Performance of Reinforced Concrete Members.* William F. Cofer. November 1999. $15.00

PEER 1999/06 *Rocking Response and Overturning of Anchored Equipment under Seismic Excitations.* Nicos Makris and Jian Zhang. November 1999. $15.00

PEER 1999/05 *Seismic Evaluation of 550 kV Porcelain Transformer Bushings.* Amir S. Gilani, Andrew S. Whittaker, Gregory L. Fenves, and Eric Fujisaki. October 1999. $15.00

PEER 1999/04 *Adoption and Enforcement of Earthquake Risk-Reduction Measures.* Peter J. May, Raymond J. Burby, T. Jens Feeley, and Robert Wood. $15.00

PEER 1999/03 *Task 3 Characterization of Site Response General Site Categories*. Adrian Rodriguez-Marek, Jonathan D. Bray, and Norman Abrahamson. February 1999. $20.00

PEER 1999/02 *Capacity-Demand-Diagram Methods for Estimating Seismic Deformation of Inelastic Structures: SDF Systems*. Anil K. Chopra and Rakesh Goel. April 1999. $15.00

PEER 1999/01 *Interaction in Interconnected Electrical Substation Equipment Subjected to Earthquake Ground Motions.* Armen Der Kiureghian, Jerome L. Sackman, and Kee-Jeung Hong. February 1999. $20.00

PEER 1998/08 *Behavior and Failure Analysis of a Multiple-Frame Highway Bridge in the 1994 Northridge Earthquake.* Gregory L. Fenves and Michael Ellery. December 1998. $20.00

PEER 1998/07 *Empirical Evaluation of Inertial Soil-Structure Interaction Effects.* Jonathan P. Stewart, Raymond B. Seed, and Gregory L. Fenves. November 1998. $26.00

PEER 1998/06 *Effect of Damping Mechanisms on the Response of Seismic Isolated Structures.* Nicos Makris and Shih-Po Chang. November 1998. $15.00

PEER 1998/05 *Rocking Response and Overturning of Equipment under Horizontal Pulse-Type Motions.* Nicos Makris and Yiannis Roussos. October 1998. $15.00

PEER 1998/04 *Pacific Earthquake Engineering Research Invitational Workshop Proceedings, May 14–15, 1998: Defining the Links between Planning, Policy Analysis, Economics and Earthquake Engineering.* Mary Comerio and Peter Gordon. September 1998. $15.00

PEER 1998/03 *Repair/Upgrade Procedures for Welded Beam to Column Connections.* James C. Anderson and Xiaojing Duan. May 1998. $33.00

PEER 1998/02 *Seismic Evaluation of 196 kV Porcelain Transformer Bushings.* Amir S. Gilani, Juan W. Chavez, Gregory L. Fenves, and Andrew S. Whittaker. May 1998. $20.00

PEER 1998/01 *Seismic Performance of Well-Confined Concrete Bridge Columns.* Dawn E. Lehman and Jack P. Moehle. December 2000. $33.00